Wavelength dependent demagnetization dynamics in Co$_2$MnGa Heusler-alloy

Dissertation
zur Erlangung des akademischen Grades
(Dr. rer. nat.)
in der Wissenschaftsdisziplin
Methoden und Instrumentierung der Forschung mit Synchronrotstrahlung

eingereicht an der
Mathematisch-Naturwissenschaftlichen Fakultät
der Universität Potsdam

von
Dipl.-Phys. Sergej Solopow

Betreuer:
Herr. Prof. Dr. Alexander Föhlisch
Herr. Prof. Dr. Oliver Rader
Herr. Dr. Torsten Kachel

Gurachter:
Herr. Prof. Dr. Alexander Föhlisch
Herr. Prof. Dr. Wolfgang Kuch
Herr. Prof. Dr. Peter Oppeneer

Golm, 19.02.2019

Zusammenfassung

In dieser Arbeit haben wir ultraschnelle Entmagnetisierung an einer Heusler-Legierung mit der chemischen Formel Co_2MnGa untersucht. Es handelt sich um ein Halbmetall mit einer $L2_1$ Kristallstruktur, das sich in einer ferromagnetischen Phase befindet. Die Besonderheit dieses Materials besteht im Aufbau einer Bandstruktur. Diese bildet Zustandsdichten, in der die Majoritätselektronen eine metallische Bänderbildung aufweisen und die Minoritätselektronen eine Bandlücke in der Nähe des Fermi-Niveaus aufweisen, das dem Aufbau eines Halbleiters entspricht.

Mit Hilfe der Pump-Probe-Experimente haben wir zeitaufgelöste Messungen durchgeführt. Für das Pumpen wurden ultrakurze Laserpulse mit einer Pulsdauer von 100 fs benutzt. Wir haben dabei zwei verschiedene Wellenlängen mit 400 nm und 1240 nm benutzt, um den Effekt der Primäranregung und der Bandlücke in den Minoritätszuständen zu untersuchen. Dabei wurde zum ersten Mal OPA (Optical Parametrical Amplifier) für die Erzeugung der langwelligen Pulse an der FEMTOSPEX-Beamline getestet und erfolgreich bei den Experimenten verwendet. Wir haben Wellenlängen bedingte Unterschiede in der Entmagnetisierungszeit gemessen. Mit der Erhöhung der Photonenenergie ist der Prozess der Entmagnetisierung deutlich schneller als bei einer niedrigeren Photonenenergie. Wir verknüpften diese Ergebnisse mit der Existenz der Energielücke für Minoritätselektronen. Mit Hilfe lokaler Elliot-Yafet-Streuprozesse können die beobachteten Zeiten gut erklärt werden.

Wir haben in dieser Arbeit auch eine neue Probe-Methode für die Magnetisierung angewandt und somit experimentell deren Effektivität, nämlich XMCD in Refletiongeometry, bestätigen können. Statische Experimente liefern somit deutliche Indizien dafür, dass eine magnetische von einer rein elektronischen Antwort des Systems getrennt werden kann. Unter der Voraussetzung, dass die Photonenenergie der Röntgenstrahlung auf die L_3 Kante des entsprechenden Elements eingestellt, ein geeigneter Einfallswinkel gewählt und die zirkulare Polarisation fixiert wird, ist es möglich, diese Methode zur Analyse magnetischer und elektronischer Respons anzuwenden.

Synopsis

In this work we investigated ultrafast demagnetization in a Heusler-alloy with chemical formula Co_2MnGa. This material belongs to the halfmetal with specific crystal structure of the type $L2_1$ and exists in a ferromagnetic phase. A special feature of investigated alloy is a structure of electronic bands. The last leads to the specific density of the states. Majority electrons form a metallic like structure while minority electrons form a gap near the Fermi-level, like in semiconductor. This particularity offers a good possibility to use this material as model-like structure and to make some proof of principles concerning demagnetization.

Using pump-probe experiments we carried out time-resolved measurements to figure out the times of demagnetization. For the pumping we used ultrashort laser pulses with duration around $100\,fs$. Simultaneously we used two excitation regimes with two different wavelengths namely $400\,nm$ and $1240\,nm$. Decreasing the energy of photons to the gap size of the minority electrons we explored the effect of the gap on the demagnetization dynamics. During this work we used for the first time OPA (Optical Parametrical Amplifier) for the generation of the laser irradiation in a long-wave regime. We tested it on the FETOSPEX-beamline in BASSYII electron storage ring. With this new technique we measured wavelength dependent demagnetization dynamics. We estimated that the demagnetization time is in a correlation with photon energy of the excitation pulse. Higher photon energy leads to the faster demagnetization in our material. We associate this result with the existence of the energy-gap for minority electrons and explained it with Elliot-Yaffet-scattering events.

Additionally we applied new probe-method for magnetization state in this work and verified their effectivity. It is about the well-known XMCD (X-ray magnetic circular dichroism) which we adopted for the measurements in reflection geometry. Static experiments confirmed that the pure electronic dynamics can be separated from the magnetic one. We used photon energy fixed on the L_3 of the corresponding elements with circular polarization. Appropriate incidence angel was estimated from static measurements. Using this probe method in dynamic measurements we explored electronic and magnetic dynamics in Co_2MnGa.

Contents

Chapter 1

Introduction

Changing of magnetization of a ferromagnetic sample is a standard physical experiment. One can increase its temperature up to the Curie temperature at which the magnetization disappears. This phenomenon is well understood and theoretically explained within the framework of thermodynamics [127]. The other possibility is to expose the sample to an external magnetic field. Elementary magnetic domains interacting with an external field will change their orientation. Typical hysteresis curves reflect the changes of the magnetization orientation and amplitude. Piezomagnetism is also a known phenomenon. It describes a magnetization change under external stress of the ferromagnetic material.

The time domain remains out of scope in these experiments. How fast can the magnetic state of the sample actually change? In 1991 Vaterlaus et al. reported about optically induced demagnetization in a ferromagnetic Gadolinium sample [140]. The Gd film was exposed to a laser radiation field of 10 ns pulse duration. The observed demagnetization time of $100\,\mathrm{ps} \pm 80\,\mathrm{ps}$ was in agreement with the existing theory of the spin-lattice relaxation [49]. Despite the agreement between the experiment and the theory a new attempt was later made towards discovering the ultimate demagnetization time. So, in 1996 Eric Beaurepaire [13] demagnetized a ferromagnetic Ni sample optically and revealed magnetization quenching on the sub-picosecond time scale. In contrast to the results reported by Vaterlaus the pulse duration of the laser used for demagnetization was 60 fs. On this time scale spin-lattice relaxation theory fails. This fact opened new questions concerning mechanism mediating ultrafast demagnetization.

Interest in the investigation of the ultrafast magnetization processes arise from different points of view. On the one hand, it is technical application in the light of new materials for information storage. Here a small spatial size and fast data recording are preferred. This focus has influenced the search for ultimate demagnetization times in different types of materials. On the other hand, one needs understanding of the fundamental mechanism

mediating magnetization loss or even reversal on the sub-picosecond time scale. The latter fundamental question, in turn, plays a crucial role in the further fabrication of materials with technical applications. The attempt at understanding of the mechanism and fabrication of new magnetic materials proceeds simultaneously.

Chronologically speaking, at first an effort was made to explain demagnetization in ferromagnetic transition metals and rare-earth elements. Later, interest spread to alloys and compounds with multiple constituents and complex electronic and crystal structure. These are materials with ferrimagnetic, antiferromagnetic and ferromagnetic order. Based on these materials the interplay between electronic structure, spin-orbit interaction, and localized and delocalized magnetic moments and their role in ultrafast magnetization can be proved. The effect of the energy gap on the demagnetization time has been researched in ferromagnetic semiconductors [141, 142].

In this work, our attention is turned towards for a material class less investigated in ultrafast magnetization research namely half-metal. We used a ferromagnetic Co_2MnGa Heusler-alloy with a well-defined $L2_1$ crystal structure and a specific, half-metallic electronic structure. The special feature here is the different behavior of the density of states for both spin components. For the majority spins, it reveals a characteristic metallic-like electronic structure and for minority electrons, it has a gap near the Fermi level, which indicates semiconductor-like states. According to the theories explaining demagnetization on the sub-picosecond time range energy gap for minority spins should reduce demagnetization time in comparison to pure transition metals. But scientific results reported so far are contradictory.

The effect of the spin polarization near the Fermi-level is widely discussed in recent papers regarding the demagnetization time. This depends, in turn, on the gap value for minority electrons. Its influence has not been understood well in relation to the demagnetization time. Recently many half-metallic materials with different gap values have been involved in research. Instead of manipulation of the energy gap we proposed to manipulate the wavelength of the pump laser. We expect to effect demagnetization time by pumping the half-metallic sample with different photon energy above and close to the gap value of minority electrons of Co_2MnGa.

To approach these goals and realize tunable wavelengths we have successfully commissioned an Optical Parametrical Amplifier on the FEMTOSPEX facility in BESSY II. It is feasible to tune the photon energy down to $1\,eV$ using fundamental $788\,nm$. Reasonable laser power until $200\,mW$ has been provided into the chamber to perform pump-probe measurements. Together with focusing lenses the laser beam yields flux up to $20\,mJ/cm^2$ by $3\,kHz$ laser's repetition rate enough for investigation of electron dynamics.

Co_2MnGa provides an additional opportunity for ultrafast demagnetization research. As a model system, it consists of two elements, which build up two ferromagnetically coupled sub-lattices. The magnetic moments of

the single elements are different in amplitude. Therefore, the interest here is to study how the demagnetization time is related to the value of the magnetic moment of a specific constituent. Additionally we can compare these dynamics to other material classes reported so far.

To achieve our aims we need a probe method with femtosecond time resolution and element specificity. One of the candidates which can be used on the BESSY II synchrotron facility is X-ray absorption spectroscopy (XAS) or its specification Near Edge X-ray Absorption Fine Structure (NEXAFS). Interaction with X-ray photons initiates transitions of core-level electrons into unoccupied states above the Fermi level. For the elements applied, the resonance energy has a specific value and makes it possible to work only with the state's density of a certain element. By the use of elliptically polarized X-ray beams, NEXAFS can be combined with the X-Ray Magnetic Circular Dichroism (XMCD) technique. Thus, it can become sensitive to the spin orientation and opens up access to the magnetization including chemical specificity. Nowadays, the fs-slicing beamline [79] at the BESSY II storage ring delivers X-ray pulses with $100\,\text{fs} - 120\,\text{fs}$ pulse duration. Therefore, it allows one to perform pump-probe experiments in ultrafast magnetization research by means of XMCD technique in transmission geometry.

In order to make a clean measurement there is a requirement for the sample thickness. It has to be one tenth of nanometer. With our bulk samples, experiments in transmission geometry are impossible. Therefore, one of the motivations of this work was the development of a new application based on the XMCD effect, which allows overcoming restrictions of the sample thickness. We focused our attention on the X-ray resonant magnetic reflectivity (XRMR) method. Impetus to this solution was the well-known dichroic effect already used [36] for the characterization of magnetic samples by means of XRMR. In this work, we used X-ray resonant reflectivity for the first time in time resolved experiments as a test of ultrafast magnetism.

We carried out experiments on the PM3 beamline [71] at BESSY II for static characterization of the Co_2MnGa sample. We performed reflectivity measurements and measured angle dependent spectra of the Cobalt and Manganese near the L_2 and L_3 edges for pre-characterization. Additionally the absorption spectra have been measured by means of the Total Electron Yield (TEY) technique. Magnetic moments of the elements have been calculated based on the recorded data. Appropriate angles have been determined for the following pump-probe measurements. We performed subsequently time resolved experiments on the BESSY II fs-slicing beamline [63]. Demagnetization times and pure electron dynamics have been measured and analyzed for both elements and for two pump wavelengths of $400\,\text{nm}$ and $1240\,\text{nm}$. A possible mechanism for ultrafast demagnetization in half-metals will be discussed.

1.1 Scope of this Thesis

In chapter 2 we will summarize the state-of-the-art knowledge in the field of ultrafast magnetization dynamics. A review of the experimental work will be given in section 2.1. Here we will mention probe techniques for magnetic states used in ultrafast research. Furthermore, the materials of interest used in the research will be listed. Phenomenological and microscopic theoretical models used nowadays for modeling and explanation of demagnetization processes will be explained in sections 2.2 and 2.3. Finally, in section 2.4 the status of the work on half-metals and Heusler-alloys will be presented and state-of-the-art knowledge will be summarized. Chapter 3.1 will be dedicated to the characterization of Co_2MnGa. Crystal structure, coupling of moments and formation of the magnetic structure will be explained on the basis of the electronic structure. In section 3.2 we will briefly describe the preparation of the sample. Optical characterization by ellipsometry and the thereby deduced index of refraction will be described in section 3.3. This information is used later on for an exact description of the observed energy in the framework of generalized matrix formalism. In chapter 4 we will present a theory for understanding resonant reflection of the sample. We link this to magnetism and perform reflectivity experiments for static characterization. The applicability of Resonant Magnetic Reflectivity in time resolved experiments will be substantiated. Total electron yield (TEY) is an absorption technique useful for the evaluation of element specific magnetic moments by applying sum rules. It will be described in section 4.1. In chapter 5 the experimental pump-probe setup is described and the results of the ultrafast demagnetization on Co_2MnGa are presented. In this chapter, we will briefly describe the principles of fs slicing and its application to pump-probe experiments. The explanation of observed demagnetization will be discussed. The final conclusion will be given in chapter 6. Here I will recapitulate the results once again and give an outlook on further experiments that will allow a deeper understanding of the processes mediating ultrafast demagnetization.

Chapter 2

Experiments and theory of ultrafast magnetization

The modern physics of ultrafast processes would be unthinkable without appropriate instruments which enable one to look inside events on the timescale of pico- and subpicoseconds. The realization of pulsed laser [92] and their further development respective higher repetition rate, shorter pulse duration, wave length tunability and simplification of their operating [30, 38] gave rise to their implementation in research of ultrafast processes in molecules and solids. Towards the end of the twentieth century time resolved ultrafast optical spectroscopy by means of pump-probe techniques, were effectively used for investigation of transient nonequilibrium electron temperatures driven from equilibrium by pico- and subpicosecond laser pulses [31, 35, 121]. Using this technique, the time evolution of electron redistribution, driven by femtosecond laser pulses, in some noble metals was observed and discussed [39, 132, 137]. Even the electron-phonon dependent redistribution of energy to the phonon system was considered [41]. Nevertheless, small attention was paid to the magnetization behavior on the time scale of transient electron temperatures and its subsequent relaxation to the Fermi distribution. This lack of information was covered by Beaurepaire and coworkers in 1996, when they performed pump-probe experiments using Kerr-effect for identification of magnetization changes in Nickel [13]. This finding opened up a new field of ultrafast demagnetization dynamics with a fundamental question: what is the driving force for ultrafast demagnetization. This chapter gives an overview of the contemporary achievement in this research field respective method of investigation, magnetic materials, time scales and theoretical models for understanding.

2.1 Review of existing experimental work

The discovery of sub-picosecond demagnetization time on ferromagnetic Ni sample by *Beaurepaire* [13] opened up a new perspective in the research field of the ultrafast magnetism. The attention of the physics society has been turned towards different types of materials for example, pure transition metals Ni and Co [11, 23], pure rare earth elements Tb, Gd [135, 144] and their alloys GdTbFe [2, 3] GdFeCo [61, 126], NiFe [73], ferrimagnetic garnets [56], ferromagnetic semiconductors [21] and other materials. In ferrimagnetically coupled GdFeCo it has been shown that magnetization can be manipulated and even reversed optically without interplay with an external magnetic field.

With respect to the demagnetization time, one statement can be made immediately: transition metals demagnetize faster. Reported demagnetization constants depend on measurement technique and resolution. They lie in the time range 50 fs - 300 fs for these elements. Rare-earth elements reveal two demagnetization times, one faster and one slower. Wietstruk et al. observed both it using (XMCD) at BESSY II [144] and Koopmans et al. explained the mechanism [9]. Pulsed laser with 100 fs pulse duration was used in this experiment. Ultrafast demagnetization occurred at around 750 fs for both elements Tb and Gd. Slower demagnetizatiation times were different, 40 ps for Gd and 8 ps for Tb [144]. In 1991 trying to estimate spin-lattice relaxation time in rare earth element Gd, in their experiments, Vaterlaus et al. applied 10 ns pulses for pumping and 60 ps pulses for probing. Measuring photoemission with spin-polarized technique times were found to be 100 pm ± 80 ps [140]. Due to the restricted time resolution Vaterlaus was only able to observe a slower demagnetization time constant.

During this experiment several parameters can affect demagnetization time and rate. The increase of the *pump fluence* has the effect that demagnetization time becomes shorter and demagnetization quenching becomes more pronounced. Reversed effects concerning times and the degree of demagnetization is observed for lower fluences. These results are well established for transition metals Ni, Co [9] as well as for rare earth elements Gd, Tb [136]. Fluence variation must lie within a reasonable range otherwise it leads to the sample damage or that the demagnetization is not induced. In some cases contradictory results have been observed. Even similar demagnetization rates might have different demagnetization times, to compare see Dalla Lonaga et al. and Koopmans et al. [25, 87].

Observations can be also affected by *sample geometry*. Here are some experiments presented with different thicknesses and differently ordered layers [67, 139]. There is no common statement concerning demagnetization dynamics and magnetization recovery. Many parameters play a role in demagnetization, namely, heat propagation through the layered system, interface effects between single layers, electric conductivity and magnetic properties

of single layers. Not even a common theory explaining the ultrafast demagnetization phenomenon exists, so that every case is considered separately. We will consider it closer in following sections.

The measurement technique chosen for probing the magnetism can also affect observed time response. For example, in reports of Güde et al. and Regensburger et al., who used *Second harmonic generation* (SHG) for probing, one can find demagnetization time constants equal to 50 fs [53, 118]. When comparing these results to the times observed by Beaurepaire et al., one can see that they are shorter than those measured by TMOKE. Both methods are based on the optical response of visible light. These measurements, or magnetic response, can be influenced significantly through additional terms in reflectivity tensor occurring during the first hundreds of femtosecond after irradiation. The challenge is to separate the pure magnetic signal from the optical one, taking the artefacts in optical response into account [86]. Briefly, optical technique like TMOKE are bulk sensitive, SHG is surface and interface sensitive and magnetic information is contained indirectly in nonlinear susceptibility. Spin-Resolved Two-Photon Photoemission (2PPS) can govern escape depth of electrons by tuning the photon energy [124].

With respect to probe technique in addition to XMCD and TMOKE there are *Two Photon-Photoemission Spectroscopy* (TPPS) [4, 82, 124, 140] and SHG [53, 60, 118]. One of these magnetism sensitive techniques can be applied according to the aim of research in magnetization dynamics.

2.2 Phenomenological models

Experimental results make ultrafast demagnetization evident. In the next sections, we review theoretical models for explaining the phenomenon of the ultrafast demagnetization. These include phenomenological and microscopic models. Both can be used for the consideration of the demagnetization in half-metals and thereby prepare the basics for the further discussion.

2.2.1 Three temperature model

The importance of Beaurepaire's observation can be summarized in the sentence that "[...] a fast subpicosecond demagnetization can be induced using femtosecond optical pulses" [13]. On the one hand, the new revelation concerning time scale of manipulation of magnetic order has been observed and questioned times known before [140]. On the other hand, the possibility of the new manipulation method actually being an optical one was explored and proven to be a fact, an important realization which is still relevant today. If one thinks about direct optical interaction between light and spin system one has to keep in mind that optical excitation in dipole approximation should preserve the electronic spin. It follows from the quantum mechanics

consideration of this process and in exact mathematical form from calculation of transition matrix elements for the solid system interacting with electromagnetic wave [107]. Experimental results revealed pump-induced Kerr rotation according to the change of net magnetization.

Trying to understand quenching of the magnetization, Beaurepaire and coworkers associated spin dynamics with spin temperature T_s and thus the existence of a thermalized spin reservoir. Spin dynamics is therefore driven by an initial hot electron distribution, leading to electron temperature T_e associated with a thermalized electron bath. The third subsystem is then lattice or phonon bath with temperature T_l. All three subsystems interact with each other exchanging energy and energy transfer is described by free parameters G_{ij} where indices i and j refer to interacting subsystems. We would like to note that from the thermodynamically point of view the concept of temperature can be assigned to the system in equilibrium. In the very short time scales this might not always be valid.

The temporal evolution of the temperature for each subsystem can be described by the three coupled differential equations:

$$C_e(T_e)dT_e/dt = -G_{el}(T_e - T_l) - G_{es}(T_e - T_s) + P(t) \qquad (2.1)$$

$$C_s(T_s)dT_s/dt = -G_{es}(T_s - T_e) - G_{sl}(T_s - T_l) \qquad (2.2)$$

$$C_l(T_l)dT_l/dt = -G_{el}(T_l - T_e) - G_{sl}(T_l - T_s) \qquad (2.3)$$

where radiation source $P(t)$ is coupled on the electronic system only. This is explained by the fact, that electromagnetic field is strongly coupled with electrons in visible range. Numerical solution of these equations is possible and was reported as well [13]. This solution strongly coincides with experimental results and reproduced temporal behavior of transient temperature curves for each thermal bath system. The main results can be summarized as follows: 1) Different temporal behavior of temperature changes for electronic, spin and lattice systems. 2) Ultrafast heating of the spin bath occurs via electron-spin interaction described with G_{es} coupling constant in equation. 3) This model reproduces the dynamics during first picoseconds driven by electron-spin and electron-lattice interactions. Processes occurred on the femtosecond time scale are driven by electron-electron interactions.

The possible scenario for the ultrafast magnetization losses can be described as follows. i) Laser pulses create electron-hole pairs (hot electrons) on a time scale of ~ 1 fs; ii) Electron system reaches equilibrium at high temperatures within 50 fs- 500 fs due to electron-electron interactions iii) Electronic excitations decay via electron-phonon coupling, increasing lattice temperature T_l. Electron-phonon relaxation time takes 100 fs - 1 ps in transition metals.

This is the so called *three temperature model* (3TM) and it is an extension of the two temperature model [66] proposed earlier. It includes an additional spin bath to describe temperature associated with spin dynam-

ics. We want to emphasize that this phenomenological description does not consider any microscopic origin of the magnetization decrease and subsequently its recovery. Understanding of whole spin dynamics therefore rests on the model of spin-temperature and its temporal evolution and it does not include any consideration of the angular momentum transfer. In order to complete 3TM, Koopmans proposed a microscopic spin-flip mechanism mediated by Elliott-Yafet-like processes and introduced it into an additional equation including probability for a spin-flip event a_{sf}. He assigned it to electron-phonon mediated momentum scattering [9]. The additional equation has then the following form:

$$\frac{dm}{dt} = Rm\frac{T_l}{T_C}\left(1 - m\coth\left(\frac{mT_C}{T_e}\right)\right) \qquad (2.4)$$

with material specific scaling factor R (unit s^{-1}). It, in turn, is related to material specific parameters $R \propto a_{sf}T_C^2/\mu_{at}$. This equation is established for normalized magnetization $m = M/M_s$ to the saturation magnetization M_s and therefore shows directly the magnetization behavior which is proportional to the spin-bath temperature. T_C and μ_{at} are *Curie temperature* and *atomic magnetic moment* respectively. Together with equations for 3TM, this additional equation (2.4) is able to fit magnetization transients and extract spin-flip parameter a_{sf} and is named the *microscopic three temperature model* (M3TM). It reproduced qualitatively laser-induced demagnetization for a wide range of ferromagnetic materials like poor transition metals Ni, Co and rare-earth Gd and as well their compounds and multilayers NiFe, Fe/Gd and others [9]. It has been found that the ratio T_C/μ_{at} can be considered as a figure of merit for demagnetization time and it plays a crucial role in the prediction of any demagnetization process. Therefore, M3TM has helped to explain the discrepancy between findings of Vaterlause [140] and Beaurepaire [13], what the 3TM was not able to do.

2.2.2 Model based on Landau-Lifschitz equation

Landau-Lifschitz equation (LLE)

$$\frac{dM}{dt} = -\gamma\left[M \times H\right] - \alpha\frac{\gamma}{M_s}[M \times [M \times H]] \qquad (2.5)$$

$$H = \frac{\delta F}{\delta M} \qquad (2.6)$$

has been proposed to describe temporal behavior of magnetization $M(r,t)$ in single-domain ferromagnetic samples. Simple phenomenological consideration helps to understand the meaning of the terms on the right side of this equation. The first term describes precession of M in an external magnetic field with homogenous magnetization in the sample. The second relaxation

term describes approaching to the equilibrium. In *molecular field approximation* the *effective field H* is estimated from the density of *free energy* see equation 2.6 which is known from the thermodynamic relations. The dependence of the free energy of the sample symmetry and magnetic anisotropy should be predetermined given and might adopt different forms according to the particular system. Parameter γ is the gyromagnetic relation. The second parameter in this equation $\alpha > 0$ defines relaxation velocity of magnetization. M_s is the saturation magnetization. There is another identical form of LLE which is known as *Landau-Lifschitz-Gilbert equation* (LLG).

$$\frac{dM}{dt} = \widetilde{\gamma}[M \times H] - \frac{\alpha}{M_s}\left[M \times \frac{dM}{dt}\right] \tag{2.7}$$

$$\widetilde{\gamma} = \frac{\gamma}{1 + \alpha^2} \tag{2.8}$$

In this equation M is a quantity of fixed length and its possible longitudinal relaxation due to dissipation processes is not taken into account. Interaction with the environment by means of coupling to thermal bath is not implemented into mathematical form and a temperature dependent change of magnetization is therefore not possible to simulate with that. At elevated temperatures, such an approach is not sufficient and has to be augmented. Desirable formalism should describe magnetization dynamics in entire temperature range below and above *Curie point T_C* and include heat source as laser for the further understanding of ultrafast processes. Despite of this lack, LLG equation has been successful applied in problems of *ferromagnetic resonance* and provide results in agreement with experimental observations.

Granin [44] derived such an equation resting on the former theoretical works. He enunciated main assumptions, which have to be incorporated in the model and expressed it in mathematical form. This can be postulated in the following way. It supposed to be a semiphenomenological model, where an isolated classical spin is considered as interacting with a thermal bath. This bath can be described by *Langevine field $\zeta(t)$*. This attempt has been made before by Brown [16] who included thermal fluctuations in LLE as random fields. Spin-spin interactions leading to the formation of ferromagnetic order are implemented by means of mean-field theory. At least the dynamics is described by *Fokker-Planck equation* (FPE), in which reduction leads to the *Landau-Lifschitz-Bloch equation*. This later can be adopted for special cases and applied for simulations of the magnetization motion in particular systems. It is not in the scope of this work to derive LLB equation from FPE and therefore we use a more general form of this equation to discuss their importance and connection to the 3TM. This is its most common form, see [6]

$$\dot{m}_i = \gamma(m_i \times H^i_{eff}) + \frac{\gamma\alpha_\parallel}{m_i^2}[m_i \cdot (H^i_{eff} + \zeta^i_\parallel)]m_i -$$

$$-\frac{\gamma\alpha_\perp}{m_i^2}m_i \times [m_i \times (H_{eff}^i + \zeta_\perp^i)] \qquad (2.9)$$

and was applied for modeling of thermal fluctuations of single domain particles [45], for the explaining of *Ferromagnetic resonance* phenomenon [6] and it is consistent with the measurements of domain wall mobility [88]. Temperature dependence of static properties of magnetization $M(T)$ are well predicted with this LLB equation [22].

This equation already includes longitudinal $\alpha_\parallel$ and transverse $\alpha_\perp$ temperature dependent damping parameters which can be expressed as

$$\alpha_\parallel = \lambda\frac{2T}{3T_C} \qquad (2.10)$$

$$\alpha_\perp = \lambda\left(1 - \frac{T}{3T_C}\right) \qquad (2.11)$$

for temperatures $T < T_C$. For temperatures higher than T_C both damping parameters are equal $\alpha_\parallel = \alpha_\perp$ [6, 22]. Effective field consist of several contributions $H_{eff}^i = H + H_A^i + H_{ex}^i$ with applied magnetic field H, anisotropy fiels H_A^i and exchange field H_{ex}^i. This can be inserted as experimentally observed values or can be estimated theoretically from f*irst principle calculations* or take it from *mean field approximation* [6, 77]. The parameter γ is the same gyromagnetic ratio as in equations 2.6 and 2.8

LLB equation only is not sufficient for modeling of ultrafast demagnetization behavior. One needs to couple it with the laser source which transfers energy into the sample heating it. Magnetization in LLB equation is related to the temperature of the system. This last is hidden in exchange field H_{ex}^i in form of the temperature dependent micromagnetic exchange parameter $A(T)$, in temperature dependent damping parameters $\alpha_\parallel$, $\alpha_\perp$ and susceptibilities χ. To accomplish LLB equation one needs to implement laser source through an additional set of equations. This is made by means of *two temperature model* mentioned in section 2.2.1. Laser source is coupled with an electronic system initiating ultrafast temperature increasing up to T_C [6, 7, 76]. This augmented form of the LLB equation is used for simulations of ultrafast demagnetization on FePt driven by ultrashort laser pulses [76, 77].

Modeling of the thermally driving processes based on LLB equation leads to results which show that demagnetization rates are limited by the longitudinal relaxation, and that this is a general phenomenon for ferromagnetic materials. The longitudinal relaxation itself depends on the coupling strength between electron and the spin system. This coupling parameter is implemented in LLB by λ, therefore this parameter should be considered, not only as a damping factor, but more like a coupling strength of spins to the heat bath [76]. The magnetization recovery depends also on this parameter.

2.3 Microscopic models

Phenomenological models deliver good results by modeling demagnetization times. Nevertheless they do not explain the microscopic origin of the angular momentum transfer. In the case of M3TM suggestion of the electron-photon scattering mediated spin redistribution has been made. The probability for spin flip a_{sf} introduced in equation 2.4 can be used only as fits the parameter of results gained by measurements [9]. In the LLB model, scattering λ parameter can be considered from the quantum mechanical point of view and therefore contains matrix elements representing scattering effects. These, in turns, are proportional to the spin-flip rate due to the coupling of the spin-system to environment [7]. Suggestions about a spin-flip phenomenon is already done in a phenomenological frame. Nevertheless this suggestion was not discussed in detail by mean of microscopic models of particles and quasi-particles interactions. This is done in this section using the three most discussed channels for spin reorientation since the discovery of the ultrafast demagnetization.

2.3.1 Theory based on spin-flip processes

There are three possible mechanisms which could govern that electrons flip their spins: i) Stoner excitations ii) an inelastic scattering of electrons on the spin-waves iii) Scattering on impurities or phonons mediated by Elliot-Yafet mechanism.

In transition metals electron-electron interactions lead to the separation of the bands to *majority* and *minority* electrons with opposite spin orientation. Exchange-split of the electrons across the Fermi level makes it possible for single-particle magnetic excitation. After this excitation, the electron leaves an occupied *majority* band and relocates to an unoccupied *minority* band. The resulting electron-hole pair is known as Stoner excitations. These are very important in itinerant-electron magnets.

Foundations of this model are works of Yafet [151] and Elliot [33]. Process of demagnetization is considered here as a reorientation of spin, due to the scattering. Each initial state shows a certain orientation which, in turn, means that electrons occupy either one band of *minority* or *majority*. After the scattering event, a spin-flip occurs and an electron's final state is that of the opposite state. Nowadays, possible partners for scattering processes are theoretically predicted to be phonons, electrons, magnons, impurities. Depending on the particle involved in scattering, one call *el-el* scattering [89, 131] mediated by Coulomb interaction, *el-ph* scattering [87, 128] and others. Demagnetization by spin-flip scattering has been already mentioned in the previous section in M3TM [9]. What makes spin-flip possible, is coupling with some other subsystem, otherwise interaction with photons would preserve the spin moment. In the case of spin-orbit coupling, the state of

the single electron is a mix of "up" and "down" sates and average over all single electron states $\langle b^2 \rangle$ involved in scattering events is proportional to the a_{sf}.

For the modeling of the demagnetization processes one needs to solve differential equation for distribution function n of the form

$$\frac{\partial n_k^\mu}{\partial t} = \sum_i \left(\frac{\partial n_k^\mu}{\partial t} \right)_i \qquad (2.12)$$

with μ electronic band index taking into account *majority* and *minority* bands, vector momentum k [89]. Chang in the distribution n occur due to different processes. These are labeled with index i. This equation is known as kinematic equation or Boltzman equation. More information about the model describing non-equilibrium electron and phonon dynamics can be found in [119]. The contribution to the demagnetization mediated by *el-el* or *el-ph* in absence of any scattering channel can be analyzed applying this model [104]. The mechanism of spin-flipping due to the scattering events, is one of the promised mechanisms for explaining ultrafast demagnetization.

2.3.2 Direct and coherent interactions

This theory considers direct interaction of a photon field with electronic charges, as the underlying mechanism that governs the ultrafast demagnetization. Here I can mention two representatives supporting this point of view: Bigot et al. [68] and Zhang et al. [154]. Bigot and coworkers disentangled the whole temporal behavior of spin dynamics from the initial excitation to the relaxation in two time regimes. The first one is a coherent regime, where the interaction between electromagnetic field with electronic charges and spins takes place. It induces demagnetization with coherent components. The second regime is an incoherent one. Here the relaxation of electrons and spins by means of thermalization occurs. Bigot discusses first the temporal regime by looking for its origin in relativistic quantum electrodynamics. Experimental results obtained with two-beam pump-probe experiments using MOKE reveal a linear decrease of the rotation θ and ellipticity η with an increase in pump fluency. The research group considers it as a main argument for the confirmation of coherent coupling between the electromagnetic field and the spins. Theoretically they consider Dirac Hamiltonian after a Foldy-Wouthuysen transformation where they pick two important contributions out for the precise observation. One of terms contains electric potential which is dynamically modified by irradiating laser field. Modified electric potential should affect the spin dynamics. The research group addresses it to the coherent process occurring during the interaction with laser pulse. The second term includes *spin-orbit coupling* (SOC). Bigot argues that it is not of the great importance for the modification of the magnetization.

Zhang et al. also suggested direct interaction between electronic charges, spins and photon field [154]. In contrast to Bigot they postulate the importance of spin-orbit coupling as well as external laser field for the demagnetization process. Arguments are based on consideration of commutation rules for spin operator and total Hamiltonian, with and without spin-orbit coupling components. In the absence of SOC, spin operator commutes with total Hamiltonian, which makes an action of spin operator on the wave function time independently. It preserves the total magnetic moment. Without SOC spin relaxation is mostly impossible [154]. We would like to note the special role of spin-orbit coupling supposed to be important in demagnetization dynamics. This is discussed in several works and different arguments concerning their role, as are presented nowadays.

Taking into account this mechanism of demagnetization Dalla Longa et al performed pump-probe experiments using circular polarized pump laser pulses. There were not observed any helicity dependent neither demagnetization nor electron-phonon equilibration times [25]. Additionally Koopmans et al reported, that the number of photons involved in direct "non-thermal" process of demagnetization is too small to detect sizable effects [86].

2.3.3 Superdiffusive spin transport

One of the latest attempts made to explain the ultrafast demagnetization of 3d metals was based on the theory of superdiffusive spin transport and has been proposed by Battiato et al. [11] and more detailed later [12]. The name of theory originated from the microscopic mechanism explaining ultrafast demagnetization, namely spin dependent transport of the electrons. Transport equation for electrons was developed taken into account in previous works [82, 95, 157] and numerically solved, showing considerable contribution to the ultrafast demagnetization.

Mechanism of the demagnetization can be described as follows: Laser beams interact with material and creates hot electrons. After the laser excitation electron absorbing photon is translated from d-band in case of transition metal to the sp- like band above the Fermi level. In contrast to the quasilocalized d-electrons sp-electrons are more mobile, so that one can consider their motion neglecting the motion of d-electrons. Excited hot electrons can subsequently move in random directions. Due to the different lifespan between majority and minority hot electrons, one electrons with one spin orientation remain longer in motion while the other decays into the d-state. Therefore, the mean free path of one electron sort is larger than of the other one. In the case of Ni [24], laser pulse creates abundance of minority and lack of majority spins in the pump area.

Inspired by the success of this microscopic theory, other groups initiated additional experiments by trying to confirm or disprove it [24, 37, 99]. One such experiment deserves closer attention, namely the experiment performed

by Rudolf et al. [24]. This group used two ferromagnetic materials Ni and Fe with separating layer of Ru and investigated the time dependent magnetization behavior on the Fe and Ni. It was done in cases of parallel and antiparallel alignment of magnetization between Fe and Ni layers. The sample was irradiated by pulsed laser from the Ni side. In the case of parallel orientation of magnetic moments the enhancement of magnetization in Fe was observed. By antiparallel alignment the demagnetization of Fe was observed. Authors explained it with spin transport proposed by Battiato et al..

Despite the evident confidence of this theory, supported by experiments, some contradictory results were presented. Schellekens et al. performed experiments which aimed at distinguishing between the contribution of local dissipation of angular momentum and the spin transport to the ultrafast demagnetization process [67]. Ni grown on insulating sapphire was used with a front- and back side pumping setup. In case of the front side pumping, insulating material should prevent electron flow from Ni to sapphire. In the case of back-side pumping thermal effect should be predominant. Results for demagnetization times were comparable for two pumping regimes. The conductive Al buffer layer between Ni and sapphire did not change results significantly [67]. The conclusion was, that spin transport does not play a significant role in the ultrafast demagnetization. In this period of time, results from Turgut et al. appeared, in which ultrafast demagnetization was performed on trilayers Fe/X/Ni with different X-spacer in respect to spin dependent scattering properties of electrons [139]. The influence of spacers was investigated on the spin transport and spin-flip mechanisms. The main statement of this group is, that not only spin transport dominant by the ultrafast demagnetization, but also both microscopic mechanisms like spin-flip and transport should be taken in account. It was substantiated by using insulating spacer [139].

2.4 Overwiew of the last results for ultrafast demagnetization on half-metals

Since the observation of the ultrafast demagnetization on Ni, an attempt has been made to spread the study of the magnetodynamic to several material classes. One of these priorities were Heusler-compounds or more general half-metals presented by wide classes of differently composed chemical elements [75]. The main question arranged was how the band-gap affects the demagnetization time and how it could be understood with theoretical models developed at this time for transition and rare-earth metals. Data, collected by several groups, seems to be striking and not unified, regarding the times observed and theory applied for discussion of the results. Here I would like to summarize some findings in field of demagnetization dynamics

on half-metal and Heusler structures.

CrO$_2$ was one of the first materials with half-metallic properties [94] where the demagnetization dynamics was observed by means of optical technique using MOKE [155]. It has a spin polarization of 95% [70]. The demagnetization time constant observed at temperature $T = 300\,K$ is $\tau = 375\,\mathrm{ps}$ which is quite long compared to transition metals. These findings are in agreement with the common understanding of the microscopic demagnetization processes. The gap in the minority states suppresses the spin-flip probability because of the lack of accessible states. Slow demagnetization could occur due to the spin-lattice interaction which is on the same time order [155] and can be explained with week electron-lattice interaction [64]. In the Three Temperature Model this observation can also be explained. Owing to the minority gap,the spin-electron channel for energy transfer is blocked and this transfer can be realized only via lattice implementation, which demands longer time. Additionally a pump-probe experiment was performed with two pumping wave length, actually $800\,\mathrm{nm}$ and $400\,\mathrm{nm}$. The photon energy of electro-magnetic field in this case is $1.55\,\mathrm{eV}$ and $3\,\mathrm{eV}$ respectively. Using the augmented Three Temperature Model the temperature increase of the spin system was calculated. The result is that in case of $400\,\mathrm{nm}$ pumping the temperature increase is faster than in case of $800\,\mathrm{nm}$. According to the model proposed by the group, it can be explained with a higher excitation probability in the minority band. While $1.55\,\mathrm{eV}$ are not enough to get the access to the dipole transition for minority electrons, the $3\,\mathrm{eV}$ energy allow this excitation pathway. The spin gap in CrO$_2$ is around $1.8\,\mathrm{eV}$ [155]. By pumping the system with photon energy quite above the minority gap, one can achieve the enhancement between the nonthermal electrons in the minority bands.

Despite of the fact, that long time scales for CrO$_2$ were observed, some other groups came to the realization, that the demagnetization time might be faster. Using two Heusler structures based on Co namely, Co$_2$MnSi (CMS) and Co$_2$FeSi (CFS), the group of Aeschlimann et al performed pump-probe experiments using MOKE as proof of magnetization [130, 131]. These structures are distinct in their position of the minority band-gap regarding to Fermi-level. While the gap in CMS is located over the Fermi-level in CFS it is located below. Demagnetization times measured are $\tau = 198^{-39}_{+64}\,\mathrm{fs}$ for CFS and $\tau = 265^{-32}_{+42}\,\mathrm{fs}$ for CMS respectively. Result for CMS was also confirmed by other groups. Mizukami et al. reported a demagnetization constant of $300\,\mathrm{fs}$ [102]. The initial step in the demagnetization is similar in both Heusler-alloys. This result is contradictory to the understanding of the demagnetization mechanism from the point of scattering mechanism leading to the spin-flip. The chemical disorder should provide defect states which increase the phase-space for spin-flips and therefore increase the initial demagnetization speed, which is identical in both compounds [103]. The

group proposed the following explanation based on the calculation of optical excitations and spin-flip probabilities via. *Elliot-Yaffet model*. According to the simulations optical excitations occur mostly in minority states and the electronic transition in majority states are not allowed. Therefore, majority electrons occupy empty minority states via spin-flip below the Fermi-level. The makes the hole-mediated mechanism responsible for the demagnetization time observed on short timescales, chemical order might be neglected. Therefore, equal demagnetization time in first 100 fs is elucidated [130, 131].

The idea of the deep-lying states due to the chemical disorder is not also confirmed by the investigation of the demagnetization in so-called ferromagnetic semiconductors. Here the ultrafast demagnetization dynamics were observed in a special class of *ferromagentic semiconductors* based on III-Mn-V elements [108] which representatives are Ga, In and As respectively [21, 84, 141, 142]. The magnetic moment is located on the Mn side and mechanism of the magnetic moment's formation and their coupling is similar to the mechanism explained for Heusler alloys. As I have already written previously in the absence of ferromagnetic elements in the compound, the total magnetic moment is localized on the Mn sides. This we can see also on the ferromagnetic semiconductors. If one tries to demagnetize GaMnAs or InMnAs it means that the whole magnetization loss would occur on the Mn atoms side.

Pump-probe measurements were performed on GaMnAs ferromagnetic semiconductor and reported by Wang et al. [21]. Pulse duration used for pumping was 120 fs with photon energy of 3.1 eV corresponding to 400 nm and this is comparable to the condition used in our experiment. MOKE technique was applied to measure laser-induced magnetic response of the material. Demagnetization time reported is τ =200 fs. On the same material the influence of the MIR pumping on demagnetization was observed and revealed an ultrafast demagnetization time regime within firs 1ps [142].In other material InMnAs 2 μm a wave length corresponding to 0.62 eV photon energy was used for pumping. The observed demagnetization time is τ =220 fs [141]. In both systems the magnetic moment is localized on the Mn sublattice, so when the demagnetization occurs, the MOKE technique measures averaged magnetization generated by Mn atoms. The comparable demagnetization times and the similarity of the formation mechanism for magnetic moment, would also justify the attempt to adopt the microscopic mechanism of demagnetization, which explain whole magnetization loss in Heusler structure.

Demagnetization time τ_M for structures with a gap in one spin channel, proposed by Mueller [103], should be proportional to $(1 - P_n)^{-1}$. With the polarization degree P_n at Fermi-level. However, in CMS and CFS it was not observed. A slower demagnetization time was also not observed in other Heusler-structure $Co_2Cr_{0.6}Fe_{0.4}Al$ [148]. Müeller et al. explained these findings with an absence of the gap. However, the absence of slower

demagnetization times in other alloys measured in other groups makes it necessary to refuse the assumption about the lack of the gap. The effect of the minority gap cannot be completely excluded from the consideration of the demagnetization. However it can be reduced since the half-metallic Heusler compounds of L2$_1$ structure are very sensible to the structural disorder. It leads to the defect states in the band gap [113]. The spin polarization degree depends on fully achieved L2$_1$ order. The observation of fast times for demagnetization in complex Sr$_2$FeMoO$_6$ [81] makes it one of the proofs of ultrafast demagnetization time in half-metall. The behavior of spin dynamics is explained by means of the lattice mediated relaxation mechanism.

The group of Münzenberg et al. investigated the influence of the annealing process on the demagnetization time in wide group of half-metals. Thermal treatment is necessary to initiate a transition from B2 to L2$_1$ phase after the growth procedure. It was possible to vary the spin polarization which, in turn, affected the demagnetization time. With the polarization of $P = 80\%$ observed demagnetization time was $\tau = 380$ fs [98]. In summary, one can see the tendency of the increase of the demagnetization time to coincide with the increase of spin polarization at Fermi-level in half-metals.

Chapter 3

Electronic structure, magnetism and optical characterization

In 1903 F. Heusler reported on the fabrication of ferromagnetic alloys from non-ferromagnetic constituents based on copper-manganese bronze alloyed with the elements tin, aluminum, arsenic, bismuth. The fact is, that all magnetic crystals or compounds known before the 20 th century contained one of the transition metals cobalt, iron or nickel. The existence of the alloys with ferromagnetic order and simultaneously without any ferromagnetic constituent, raised additional questions in the understanding of magnetism. Now full-Heuslers are established as ternary intermetallic compounds with magnetic order and $L2_1$ crystal structure. A change in the chemical order or their type effects the magnetic phase, which can adopt ferromagnetic or antiferromagnetic order [50, 74, 143].

In addition to the interesting magnetic properties Heusler alloys reveal particular behavior of electronic structure. As we know, in relation to the band structure, condensed matter can be divided into three major groups: conductors, semiconductors and insulators. Semiconductors and insulators reveal a direct or an indirect gap, while conductors do not have any gap between branches of dispersion bands. These features can also be seen in *Density of States's* (DOS) behavior of materials. Where DOS, as a function of energy, exhibits non-zero density at Fermi level for metallic elements and especially transition metals [26, 69, 150], semiconductor's DOS reveals gap at Fermi level [65, 96]. For the Heusler-structure it is typical to have a hybrid behavior of DOS for minority and majority electrons. This means, that in Heusler-alloys, DOS for minority or spin-down electrons have a gap at Fermi level and one can consider them as exhibiting semiconductor-like behavior. For the majority or spin-up electrons there is no gap and one can consider metallic-like behavior for DOS.
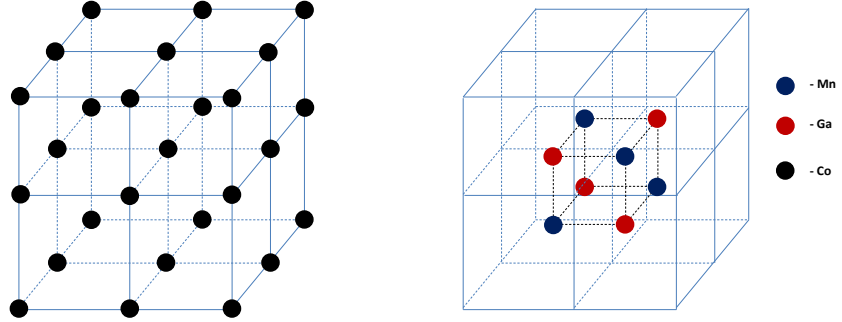
Figure 3.1: *L2₁ structure of Co₂MnGa Heusler alloy. On the left side of the figure are demonstrated pure Co-ions positions. On the right side of the figure are mounted Ga- and Mn-ions. Nodes of the lattice are occupied by Co-ions.*

There is a close relation between crystal structure, electronic structure and magnetism in Heusler-alloys. Hence, in the following chapter, we would like to enable an insight into the crystalline structure, the origin of the gap for minority band and the magnetic properties of full-Heusler alloys and in particular of Co₂MnGa.

3.1 Crystal electronic and magnetic structure

3.1.1 Crystalline structure and magnetic order

In our work we consider Co₂MnGa a full-Heusler alloy with the common generic formula X_2YZ. Here X and Y are transition metals, which can be substituted by $X = Co, Ni, Cu, Pd$ and $Y = Mn$, Z can be represented by main group elements $Z = Al, Sn, Ga, Ge, Sb$. Co₂MnGa crystalizes in the $L2_1$ crystal structure with cubic space group $Fm\bar{3}m$. According to the Wyckoff position, X atoms occupy 8c $(1/4, 1/4, 1/4)$, Y 4a $(0, 0, 0)$ and Z 4b $(1/2, 1/2, 1/2)$ positions. The structure of a full-Heusler consists of four interpenetrating *fcc* sublattices [42, 43, 143]. Two of these sublattices are occupied by X atoms.

In figure 3.1 the structure of the $L2_1$ type is illustrated. To make the structure more clear, the draft is separated into two parts. In the first one, the unit cell with Co-ions is illustrated and in the second one, the rest of the ions like Ga and Mn are inserted in the unit cell.

From the crystallographic point of view, a full-Heusler structure can be considered equal to a CsCl-like superstructure. This structure is known

as simple cubic structure with two atoms in basis. First, let us consider Cs, is placed at (0, 0, 0) position while second one (Cl) occupies position $(1/2, 1/2, 1/2)$. Looking at figure 3.1, one can see, that this representation of the Heusler structure might be reasonable. X-atoms build simple cubic lattice, while Y and Z atoms occupy the centers of these lattices leading to the CsCl-like superstructure. The full-Heusler structure can also be described with a NaCl-like structure. Y and Z elements, with cationic character are the building blocks in this structure, and with dominant ionic interaction they are seated octahedral. Thereby, tetrahedral holes are filled with X atoms. It is like a zinc blende sublattice, with X and Z atoms, with a second one X atom in the tetrahedral hole. The Y atom occupies the octahedral position [51].

If one looks at the Co atoms, in this manner it is evident that ions are sitting on cubic lattice and have octahedral symmetry (O_h). This remains true only if other atoms are neglected; that is to say the Mn and Ga atoms. Mounting the Mn nd Ga ions in the symmetry will be reduced to the tetrahedral one (T_d) which is subgroup of the O_h symmetry group [42]. The occupied symmetry will be important in the crystal-field treatment of the energy splitting and will be explained in the following sections.

The electronic and magnetic properties of Heusler alloys strongly depend on their atomic order. There are studies which show, that even a small disorder in the atomic distribution causes changes in physical properties [101, 113]. There are different types of disorder known in Heusler compounds. To gain an insight, one can read [51]. One of the most frequent types disorder is that leading to the B2-type structure. Here Y and Z atoms are equivalently distributed, so that $4a$ and $4b$ positions become similar. This leads to the formation of the CsCl-like structure and to the B2-type structure. Therefore, symmetry is reduced to the space group $Pm\bar{3}m$.

3.1.2 Formation and coupling of moments

Heusler-alloys of the type X_2YZ are ternary, magnetic, intermetallic compounds [143]. X and Z chemical units might belong to nonmagnetic elements like *paramagnetic* Aluminum and Palladium. In such cases, magnetization is mostly formed by an Mn atom, which takes the X position in the unit formula. A magnetic moment can emerge additionally on the X side if built-in elements are magnetic, like *ferromagnetic* Ni, Co. Heusler alloys can adopt different kinds of magnetic orders in ground state. These are the antiferromagnetic and ferromagnetic phase [90]. The major part of the full-Heusler considered here, are ferromagnets and the reason for adopting the ferromagnetic phase will be elucidated further.

Trying to understand the formation of the magnetic moments and their coupling Kübler et al. [90, 147] performed energy-band calculations on different types of Heusler materials with ferromagnetic and antiferromagnetic

ordering. Self-consistent calculations were based on augmented-spherical-wave formalism [146], local-spin-density of electronic exchange [83] for the solution of the effective single-particle equation. The main result is, that in all observed Heusler-alloys with a Mn constituent the magnetization is confined to Mn atoms. An further interesting point is that this effect occurs by means of delocalized d-electrons in the common d-band formed by X and Mn atoms. The reason for this localized behavior is the fact that d-electrons in minority bands are excluded from the Mn 3d shell [90, 147]. This conclusion is based on the analysis of the DOS for different Heusler structures. How is the fact of the localization of the magnetic moment in the DOS manifested? The majority electronic states of Mn atoms are located below the Fermi level and are completely occupied. The bandwidth additionally reveals that d-states of Mn atoms are delocalized as d-states of X-toms. Minority states, in contrast, are located above the Fermi level and therefore are not occupied or partly filled. As such, majority electrons joint the d-electrons of X atoms and form a common d-band, while minority electrons are excluded from the Mn sides. As a result, a formation of the region with localized magnetization confined on the Mn atoms is completely formed from itinerant electrons [90, 147]. In figure 3.3 DOS is calculated for Co and Mn separately. In case of Co_2MnGa it is not obvious that minority states are completely located above the Fermi level. Nevertheless, the main part of Mn states is localized predominantly above the Fermi-level.

The next question is about the correlation between localized moments and how they couple ferromagnetically. The distance between two neighboring Mn-Mn atoms are around 4.2Å. Consequently, the indirect interaction mediated by the free electrons of other constituents in the compound might be supposed for the formation of the ferromagnetic order. One of these mechanisms could be presumed to be the *Ruderman-Kittel-Kasuya-Yosida* exchange interaction [74, 97]. Kübler et al. and Kasuya underlined this fact, making clear, that the calculated DOS would have other shapes in case of evident direct interaction between Mn-Mn atoms [74, 90]. The ferromagnetic or antiferromagnetic coupling between Mn-Mn atoms depends on the type of atoms which mediate their coupling. If it is mediated by X-atoms (I still consider Heusler compounds with generic formula X_2MnZ) then the interaction is ferromagnetic. That we have for particular compound Co_2MnGa. If the interaction is mediated by Z atoms, then the sign of the interaction depends on the location of the DOS of p-d hybrids respective to the Fermi level [90, 147].

Of importance is the mechanism responsible for the formation of the *ferromagnetic* or *antiferromagnetic* state. According to Kübler et al. [90, 147] there are two fundamental mechanisms responsible for the parallel or antiparallel alignment of the sublattices. On the one hand, there is intra-atomic exchange splitting of the d-states in Mn atoms, and on the other hand, there is a competing interatomic covalent interaction between d-states

on different Mn atoms. The last mechanism is mediated by p-states of Z atoms. In the case of covalent mechanisms, the *antiferromagnetic* order is energetically preferred. Z atoms or in the case of Co_2MnGa compound, Ga atoms provide p-orbitals and by means of this orbital covalent Mn-Mn interaction occurs. X atoms define the lattice constant while Z atoms define the type of magnetic order.

3.1.3   Origin of the band-gap

In the Co and Mn based full-Heulser alloy of the type Co_2MnZ, where Z stands for Ga, Ge, Al, Si, two hybridization mechanism contribute to the formation of the gap in minority electrons states. The first one, is the hybridization of electron's orbitals of Co ions and secondly, the hybridization of Co-Co states follows subsequently with electrons of Mn atom. We have mentioned in a previous chapter that Co atoms only adopt octahedral symmetry (O_h). This occurrence makes possible the existence of the localized states at the Co sites, which obey the octahedral symmetry (O_h).

Lying far below the Fermi level, sp-bands lose their importance for the gap formation and are therefore excluded from consideration. Only 15 d-states are involved in the hybridization and formation of the energetic gap [43]. Nevertheless s- and p-bands formed by sp-elements are important for controlling the total magnetic moment. There is one s- and three p-bands presented in valence band. These are fully filled with 4 majority and 4 minority electrons. This number is fixed for all sp-atoms like Al, Si, Ga, Ge. It means that the rest of total valence electrons are distributed in hybrid band formed by coupling of constituents.

Here we will follow the description given by Galanakis et al. We consider first the hybridization of Co d-electrons. There are five d-orbitals according to the quantum mechanics degeneration rule $2L + 1$ with $L = 2$. So we have five following d-orbitals: $d_{xy}, d_{yz}, d_{xz}, d_{3z^2-r^2}$ and $d_{x^2-y^2}$. According to the crystal-field theory, the octahedral position of the Co atoms leads to the splitting of 5 d-orbitals into two levels with e_g and t_{2g} symmetry. Here, $d_{3z^2-r^2}$ and $d_{x^2-y^2}$ orbitals belong to the doubly degenerated e_g level and d_{xy}, d_{yz}, d_{xz} to the triply degenerated t_{2g} level. Each of the new levels has the same energy. Splitting occurs in the way that $E_{e_g} > E_{t_{2g}}$.

Interacting $d_{3z^2-r^2}$ and $d_{x^2-y^2}$ orbitals of each Co atom create bonding e_g and antibonding e_u twofold degenerated states, while interaction between d_{xy}, d_{yz}, d_{zx} states leads to the formation of triply-degenerated bonding t_{2g} and antibonding t_{1u} states, see figure 3.2 . The tetrahedral symmetry is a subgroup of the octahedral symmetry, therefore, it makes the existence of the states possible only on the Co sites [42].

On the figure 3.2 degeneration is marked by indices in front of states. Due to the symmetry reason e_g and e_u orbitals on the one Co atom can only make hybrids with e_g and e_u orbitals respectively of the other one. It
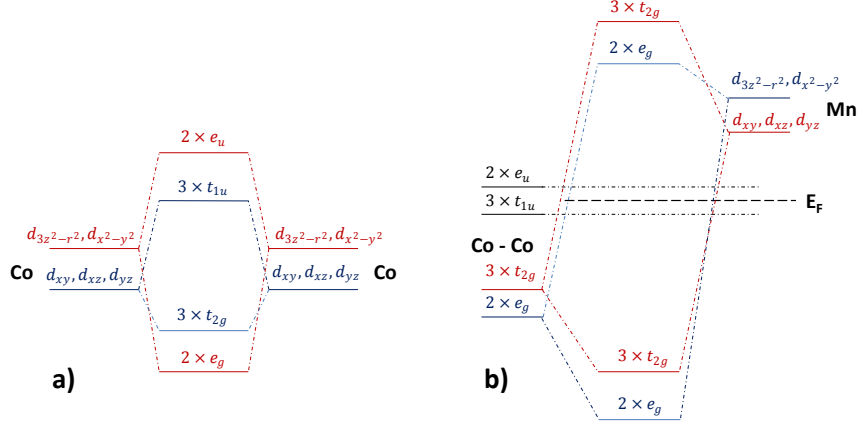
Figure 3.2: *Diagram of minority state splitting (the origin is the publication of Galanakis et al. in [42]) a) formation of bonds due to Co-Co interaction b) splitting due to interaction between hybridized Co-Co and Mn orbitals.*

holds also for t_{2g} and t_{1u} orbitals. Each Co atom in a simple cubic lattice is surrounded by six other Co atoms and the crystal field energy is split in such a way, that $E_{e_g} < E_{t_{2g}}$ see figure 3.2 . Now we consider the formation of hybrids between coupled Co-Co and Mn d-states. Doubly degenerated e_g orbitals of Co-Co coupling hybridize with $d_{3z^2-r^2}$ and $d_{x^2-y^2}$ states and form double degenerated bonding e_g and antibonding e_u states. They are different in energy and placed differently in respect to the Fermi level. While bonding e_g states lie below the Fermi level and are therefore occupied, antibonding e_g states lie above the Fermi level and are unoccupied. The t_{2g} orbitals of Co-Co hybrid couple to d_{xy}, d_{xz}, d_{yz} states of Mn. It leads to the formation of three t_{2g} states above the Fermi level and three t_{2g} states below the Fermi level. e_u and t_{1u} states of Co-Co remain uncoupled and these states are non-bonding with respect to Mn and Ga atoms. Occupied t_{1u} lie below the Fermi level while unoccupied e_u lie above. Without hybridization between these states and the states of Mn atoms, the octahedral crystal field splitting leads to the following relation between energy levels $E_{e_u} > E_{t_{1u}}$. The real gap at E_F is affected by $d-d$ hybridization between atoms of transition metals see 3.2 . Trying to summarize all available states, we can count bonding Co-Mn states five antibonding Co-Mn states. There are five non-bonding Co-bands
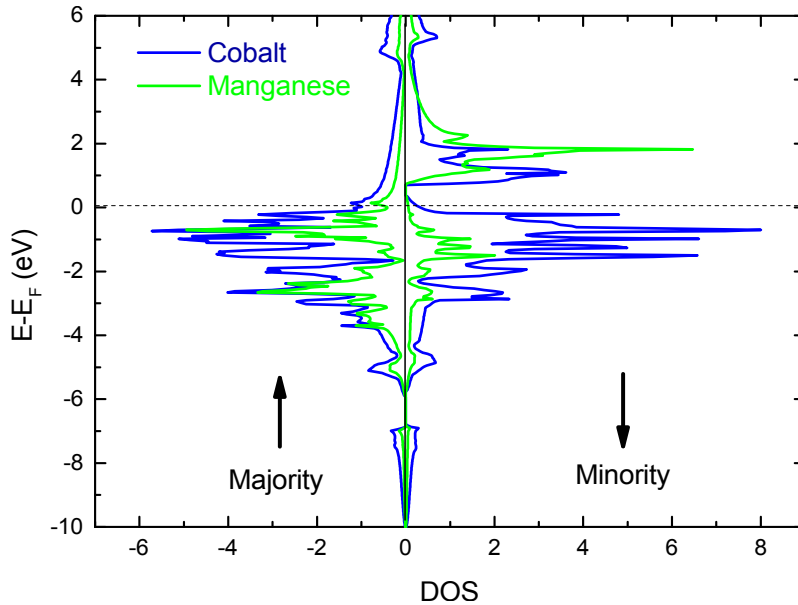
Figure 3.3: *Spin resolved partial Density of states (Calculated by Galanakis et al. [42]).*

so that two e_u bands are empty and three t_{1u} are occupied. The number of minority states lying above the E_F is therefore seven. If all majority d-states were occupied, the highest value of the moment would be $7\mu_B$.

We would like to note, that states in minority bands are localized at the Co sites and do not couple with the Mn atoms. In the figure 3.2 one can see, that these are doubly degenerated e_u and triply degenerated t_{1u} states. As I showed, these states appear due to the coupling of Co atoms. The distance of the Co atoms is considered as a second neighbors distance and therefore the splitting between e_u and t_{1u} is small. This fact is also evident in element resolved DOS, see figure 3.3.

3.1.4 *Ab-initio* calculation of the DOS and theoretical prediction of magnetic moment

Using the crystal structure electronic properties can be inferred subsequently using first-principle calculation of the electronic structure. *Ab-initio* calculation of the band structure for Heusler-alloys with ferromagnetic order were performed by several groups [8, 90, 112]. In this work we would like to mention the results of I. Galanakis at al.. *Ab-initio* calculation of the DOS for the Co_2MnGa alloy has been done using full-potential screened Korringa-Kohn-Rostoker Greenn's function method [110] complemented with local spin density approximation. The formalism used by Galanakis et al. is

different to the augmented-spherical-wave formalism applied by Kübler et al. [90] and discussed in previous chapter. Both methods predict the existence of the gap for minority electrons and metallic behavior for majority electrons. The presence of the gap in minority bands was observed with *Spin-Resolved Ultraviolet Photoemission Spectroscopy* (SR-UPS) [85]. The spin polarization value observed and reported is 55% which does not satisfy 100% expected for full-Heusler alloy.

The prior discussed ferromagnetic coupling of the Co atoms to the Mn atoms is well confirmed in the work of Galanakis et al. [42]. Magnetic moments of the constituents predicted from the calculation are: $m_{Co} = 0.688$, $m_{Mn} = 2.775$, $m_{Ga} = -0.093$ in units of μ_B [43]. It is different to the values predicted by *Ayuela et al.* which are: $m_{Co} = 0.76$, $m_{Mn} = 2.72$, $m_{Ga} = -0.07$ [8]. While the formalism used for the DOS and magnetic moment calculations are identical, one can see a little disagreement between the values for the magnetic moment. The reason might be a different lattice constant, taken as parameter for these calculations. While Galanakis et al. used a lattice constant of 5.802Å from [80], Ayuela et al. applied lattice constant from the older report of Webster [143].

One particular feature attracts attention in the values of magnetic moments: they are not integer numbers. As were discussed in subsection 3.1.3 both the number of valence electrons and the number of occupied minority states are integer numbers. As consequence of this circumstance the number of the total magnetic moment should be an integer. That is not the case. Galanakis et al. assigns it to the particular feature of the Korringa-Kohn-Rostoker Green's function method which does not include all angular moments. Due to this fact the state normalization is broken. This shortage can be overcome applying Lloyd's formula used in [29]. This formula makes it possible to get an integer number for the magnetic moment. Galanacis et al. refers to the result of the group, where the estimated total magnetic number for Co$_2$MnGe was $5\mu_B$ instead of $4.941\mu_B$ [42].

Slater-Pauling behavior for the total magnetic moment

In prior sections, we have mentioned that the total magnetic number of the full-Heusler alloy should be an integer number. This conclusion arises from the fact, that the number of valence electrons and the number of occupied minority states is an integer. This is a result of the electronic and the energy gap in minority bands. The total magnetic moment is a difference between spin-up and spin-down of occupied states: $M_t = N\uparrow - N\downarrow$ measured in μ_B units. The total number of electrons accordingly is $Z_t = N\uparrow + N\downarrow$. Now we can write the total magnetic moment in the following way: $M_t = Z_t - 2 \cdot N\downarrow$. Z_t is the total number of valence electrons and $N\downarrow$ is a number spin-down electrons or electrons which occupy minority bands. The aim at present is simply to count all possible minority states on hand of structure presented

in figure 3.2 , which can be occupied in ground state and valence electrons contribute by elements in the compound. Here we have d-bands of Mn and Co atoms and sp-bands of Ga atoms, which can be occupied with electrons. The first electron comes into the s-state and the next two come into the p-state, which yields Ga atom. d-bands coming from the coupling of Co-Co and Co-Mn atoms can be counted. These are $2 \times e_g$, $3 \times t_{2g}$ and $3 \times t_{1u}$ states. The presence of the gap in minority bands makes it possible, that only these states are filled in ground states below the Fermi-level. Together with sp-electrons the total number of electrons in minority bands is 12. So the magnetic moment can be written as $M_t = Z_t - 2 \cdot 12 = Z_t - 24$. This expression represents the so-called Slater-Pauling rule for the description of magnetic moments in binary metallic compounds [78]. Fecheer et al. also confirmed the validity of this behavior for full-Heusler alloys [40]. In the case of Co_2MnGa the total number of valence electrons is 28. This means that, the possible magnetic moment should be $4\mu_B$. Since the number of valence and conducting states in a Heusler alloy with Co and Mn constituents is fixed, the number of electrons in the system can be changed through the introduction of other sp-atom as Ge, Si with 4 valence electrons and Al, Ga with 3 valence electrons. This increases the number of electrons to 25 in case of valence with four electrons and the magnetic moment accordingly become $5\mu_B$. This is one of the particular features of the full-Heusler alloys where the magnetic moment can be adjusted with the incorporation of an appropriate sp-element.

The hybridization scheme leading to the formation of the band structure described in the section 3.1.3 is common for the compounds with the generic formula X_2YZ with the transition metal on the position of X and Manganese in Y position. As such, the substitution of the Co atoms though Nickel or Iron, would lead to the same Slater-Pauling behavior of the magnetic moment. Therefore, the advantage of such substitution is the manifold possibility of manipulation not only of magnetic moment but also of the polarization rate at the Fermi level.

3.2   Sample preparation

To our best knowledge, one of the first reports about the fabrication of the Heusler-alloy was published by Suits in [134]. The structure of the X_2YZ was produced with Rh on the X and Mn on the Y side. The adopted crystal structure was of the type $L2_1$ and established as ferromagnetic. Later, Kanomata et al. synthetized Ru based Heusler-alloy on the X side with antiferromagnetic order. Heusler-alloys can be fabricated nowadays by molecular beam epitaxy. There are sufficient reports on the fabrication technique for thin films and single crystals. Here I can mention some works in the field of the epitaxial growth of some Heusler-compounds. Ambrose et al. reported

about the fabrication of Co$_2$MnGe on GaAs(001) substrate [5]. Raphael et al. succeeded to produce thin films as well single crystals of Co$_2$MnSi [117]. Finally Geiersbach et al. reported about fabrication of Co based Heusler-alloys with (110) orientation on the MgO(001) substrate [46]. To put it precisely, one can find the variety of the substrates, growth conditions, crystallographic growth directions and other parameters by the fabrication of alloys. It is out of the scope of this thesis to discuss this. We would mention the growth procedure of our Co$_2$MnGa sample.

For the fabrication of Co$_2$MnGa Heusler-alloy MgO substrate with (001) orientation has been used. All parameters like substrate temperature and pressure in the epitaxy chamber and deposition methods for the deposition of single stacked layers are summarized in the table. After this growth process, the real structure of Co$_2$MnGa is $B2$, in order to induce transformation to $L2_1$ sample has to be annealed at $500°C$.

Layer	Deposition method	Temperature	Chamber pressure	Beam pressure
Al, 3nm	RF Magnetron Sputtering	Room temperature	$1e^{-9}$ mBar	0.05 mBar
Co$_2$MnGa, 100nm	RF Magnetron sputtering	Room Temperature	$1e^{-9}$ mBar	0.1 mBar
MgO, buffer layer, 10nm	Electron beam evaporation	$400°C$	$2e^{-10}$ mBar	$2e^{-7}$ mBar

Table 3.1: *Method and growth conditions for single layers.*

3.3 Optical properties of Co$_2$MnGa

The interaction between an electromagnetic field and matter can be described with Maxwell's equations. Depending on the type matter, like a dielectric material, or a conducting solid, these constitutive equations can be slightly modified. From the mathematical point of view this are four partial differential equations which special solution need boundary and continuity conditions. Especially two cases can be considered by solving Maxwell's equations: the first one is a static case, where the external field is time independent and the second one, where the external field is time dependent. A time dependent magnetic or electric field has a particular feature, namely it propagates like a wave in space. It follows directly from Maxwell's equations, which in the case of time dependent fields, can be modified to

wave equations. The response of solids to the external irradiation can be described with optical constants which are functions of circular frequency ω. There are different types of response functions and their applicability depends on the particular problem. Going into detail, one can deal with the *susceptibility* χ, *permittivity* ϵ, *refractive index* η and *impedance* Z. While χ is useful at a microscopic level, ϵ can be used for more macroscopic phenomena. The form of these functions can be found in a classical way by the solving of Newton equations or with the application of Quantum mechanic for more detailed solution. These response functions can be expressed by means of each other. So knowing one of them allows possibility to get an expression for another one of interest. All of these functions are complex functions with real and imaginary parts and generally have tensor character. For more information I revise to standard literature [27, 32].

Optical characteristics of Co_2MnGa is of great importance for making a statement about wave dependent pump-induced demagnetization. So we would like to inform briefly of the experimental way of getting information about an index of refraction and we will shortly explain how this index can be used in transfer-matrix formalism for the estimation of an absorption profile.

3.3.1 Experimental estimation of refractive index

To calculate absorption or reflection, it is convenient to use functions for macroscopic response. This is described by the refraction index $\hat{n} = \eta - i\kappa$. It consists of real and imaginary parts η and κ respectively, which are responsible for the dispersion and absorption processes of the electromagnetic wave by propagation in the environment. Knowledge of this index makes it possible to estimate the reflected and absorbed intensity of incoming light. This estimation is of great interest for the interpretation of ultrafast processes. For the determination of these coefficients there are two possibilities. The first is *ab initio calculation*. A detailed explanation for glass can be found in reference [133]. The second is to perform measurements. One of the most powerful tools nowadays is *spectroscopic ellipsometry* which can be used for the optical characterization of differently stratified thin films, see example [48]. Using ellipsometry, one can measure ellipsometric parameters and then extract parameters of interest, such as the index of refraction. In figure 3.4 both parts of the refractive index are depicted. Measurements were performed on commercial ellipsometer "Sentech SE850" in ISAS Institute. Using different four angles, ellipsometric parameters were recorded at room temperatures and the refractive index was extracted.

Knowledge of optical constants for other material in the stack was of interest. Therefore, the refractive index of MgO substrate was measured separately and compared with literature and the refractive index of Al has been taken from literature. Knowing optical parameters of constituents in
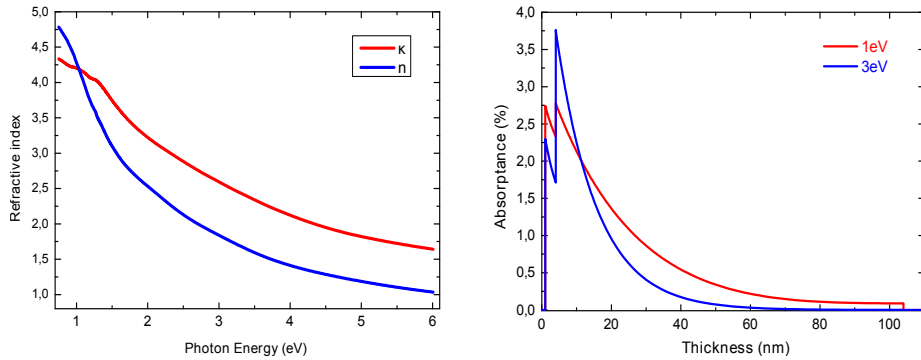
Figure 3.4: **Left**: *Real and imaginary part of refractive index estimated under the suggestion of absent Aluminum capping layer.* **Right**: *Absorbance profile calculated using matrix formalism.*

layers and the gained ellipsometric parameters index of refraction for Heusler could be estimated.

The aluminum content in a capping layer was not observed by measurements. Any assumption might be a damaging to this layer. On the other side ultra-thin layers can have different optical responses than bulk systems as described in [93]. The thickness of the Aluminum capping layer is $3\,\mathrm{nm}$ and can support this assumption. The simulations for the layered system are performed under the assumption, that Al does not affect the total optical constant of the system so pronounced.

3.3.2 Calculation of absorption profile of Co_2MnGa

Absorption calculation in layered systems is a well-known problem in theoretical optics. It has been widely used, for instance, in photovoltaic [47] to estimate the spectral absorption in stratified isotropic mediums with different optical constants. In this work we have adopted a useful framework of generalized matrix formalism for the calculation of the absorption profile in Co_2MnGa. To compute absorption in layers one can use

$$A = \int\limits_{z_1}^{z_2} \alpha(z)I(z)dz \tag{3.1}$$

integration over the thickness profile along z-Orientation using absorption coefficient $\alpha(z)$ and light intensity $I(z)$. Another way is to use energy flux Φ so that absorption is expressed as

$$A = \Phi(z_1) - \Phi(z_2) \tag{3.2}$$

To perform calculation where the energy flux is expressed over a Poynting vector, two main cases have to be considered. *Coherent layers*, where internal interference is taken into account and *Incoherent layers*, where internal interference is omitted [19]. An absorption calculation using the second approach with energy flux leads to the so-called generalized matrix formalism. It is described in papers [19, 28, 109]. The main idea is to describe all possible processes like refraction, reflectivity, phase changing and so on, which occur on the interface between two media in the form of matrices. So the propagation Matrix **S** can be expressed in the form of matrix multiplication between propagation at the interface **I** and propagation in the layer **L** [19]. If such matrices are built for every interface and layer so the final propagation matrix simply results from the matrix multiplication of all matrices like $\mathbf{S} = \mathbf{I}_{ij}\mathbf{L}_j\mathbf{I}_{i+1,j+1}...$ and the problem is simplified by establishing $\mathbf{I}_{ij}$ and $\mathbf{L}_j$ matrices. Coefficients of this matrices are generally functions of refractive index and consequently, wave length dependent [109].

We have applied the analytic method for calculation of absorption profile in Co_2MnGa for two pump regimes 400 nm and 1240 nm. The original Matlab code was developed by Dr. Loïc LeGuyader and adopted for our system. In figure 3.5 you can see it. The formalism is based on a matrix form of propagation and the reflection of incidence light in spatial cases of p-polarized light. Here the electric field of wave lies in the incidence plane and this is similar to the pump conditions. It is out of the scope of this work to discuss the whole challenge of propagation of electromagnetic field in metallic medium and here we just would like to emphasize that the formalism has been applied in existing forms, described in references we have mentioned. When knowing the parameters of layers, for example thickness and the index of the refraction, absorption profile can be calculated see figure 3.4. Integrated over the whole depth profile of Co_2MnGa we can obtain the absorbed fluency in samples. In figure 3.5 percental absorption per depth is illustrated.

Information about absorbed photons can provide information for the deeper understanding and analysis of experiments. Further we would like to extract some useful parameters for discussion of final results. Using the aperture in form of pin-hole with $100\,\mu m$ diameter together with Si-photodiode we were able to measure laser profile in focus. Laser beams were previously aimed at the photo detector. Using motors for horizontal and vertical motion of pin-hole transmitted, the intensity of laser was measured. The result is a Gauß-like profile of transmitted intensity. With the convolution procedure, real size of a laser spot was determined. Pump-probe measurements were performed under angle of 7°. This means that it is necessary to find the projection of the laser at the surface for the correct estimation of total fluency. The sample was pumped with a 3 kHz pump laser. The power was measured with a powermeter for 400 nm wavelength was 170 mW. The full width of half maximum was derived for vertical motion of the aperture was
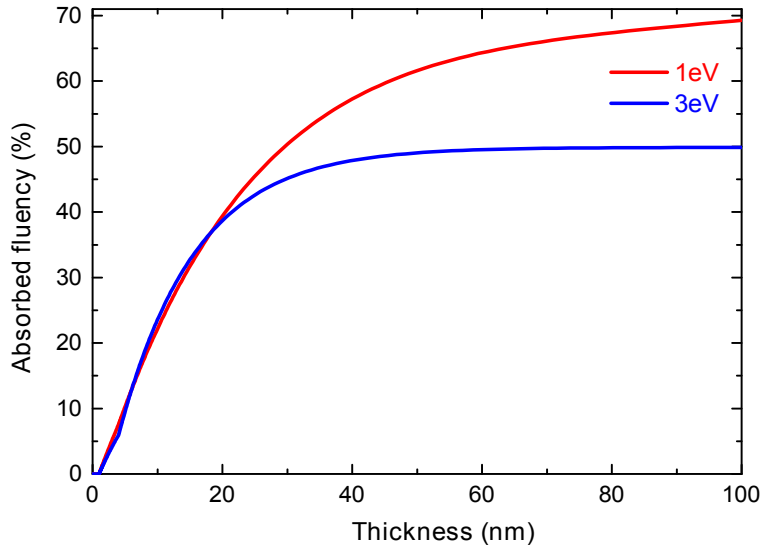
Figure 3.5: *Absorbed fluence in percent per depth in Co_2MnGa for 400nm and 1240nm wave length.*

FWHM$_v$= 212 μm and for horizontal FWHM$_h$= 246 μm. Using these values we can calculate pump fluency at 2.1mJ/cm^2. Knowing the absorption profile of the whole stack layers, we can additionally calculate the amount of the energy absorbed by single layers. So we found that Al-layer absorbs 5.92% of the total intensity and Co$_2$MnGa layer absorbs 43.95% of the whole irradiated intensity. We can proceed to the analysis of energy absorption and distribution in the sample and try to figure out the number of photons absorbed per unit cell or per layer unit. In order to realize it, we need an excited volume and the absorption, which is already calculated. The size of the unit cell is well-known a=5.77Å. The surface covered by the laser can be estimated at $A = \pi r_1 r_2$, where r_1 and r_2 are taken from FWHM. Taking the incidence angle into account, the laser spot size on the sample surface is $A = 34 \cdot 10^{-4}$cm^2. The further distribution of the incoming photons proceeds on this surface. The whole number of photons coming with one laser pulse can be estimated as well.

In the case of the 1240 nm pump, the wavelength absorbed energy differs from 400 nm. Here we have 7.55% for Al layer and 62.1% for Co$_2$MnGa layer. Calculated fluency was 1.9 mJ/cm^2. In figure 3.5 we see that absorbed energy down to 20 nm is quite homogenous. These results will be used in furthers chapter in the analysis of optically induced magnetization dynamic.

Chapter 4

Resonant X-ray magnetic reflectivity and absorption used for sample characterization

X-ray synchrotron radiation is a powerful tool for the investigation of electronic and magnetic structures of thin films. Based on the common principles of propagation, reflection and absorption of electromagnetic waves in solids, it can provide information about thickness, roughness, optical constants and other parameters of interest. This chapter describes the principle of absorption spectroscopy and X-ray resonant magnetic reflection. Afterwards we present characteristics of Co_2MnGa, an essential basis for further discussion. Furthermore, a new probe method for magnetization dynamics is justified in this chapter. It is our main aim to show that demagnetization dynamics can be probed by means of resonant X-ray reflectivity. We will show that at certain conditions, like photon energy tuned to resonant excitation and suitable incidence angles, demagnetization can be measured with good approximation. For this reason, a number of static characterizations, like angle dependent reflectivity and absorption spectra have been performed. From the static experiments, values of interest for dynamical measurements can be deduced.

4.1   Absorption technique and sum rules

Progress in the development of synchrotron radiation gave rise to an increasing number of X-ray absorption spectroscopy (XAS) experiments. Here the advantage of the tunable photon energy and polarization of the X-ray radiation was used as an important feature to access intrinsic element specificity.

In order to obtain information about magnetic properties one needs to develop methods with access to the atomic spin and orbital moment. In the year 1987 the X-ray magnetic circular dichroism (XMCD) effect was discovered by Gisela Schütz and others [91, 125]. A theory explaining the observed effect was later developed by Thole at al. [18, 138]. Since then XMCD became a unique technique, which provides element specific information about magnetic properties of the material. Symmetry selective sum rules allow separation between spin and orbital magnetic moments.

In X-ray absorption near edge structure (XANES), one considers transitions of electrons from initial core level states into the empty void, like e.g. 2p core states in case of transition metals into empty states above fermi level. Due to the spin-orbit splitting, two states are available ($2p_{3/2}$ and $2p_{1/2}$) with an energy gap of about $15\,\text{eV}$. Using the Stoner picture we can consider the DOS of the d-electrons as split into two bands of majority and minority spin. Within this model the X-ray absorption mechanism is spin dependent. For XMCD circularly polarized X-rays are applied with well-defined helicity $\sigma = \pm 1$.

X-ray quanta with fixed helicity transfers its momentum to one of the spin sorts and therefore initiates electron transition with preferred spin orientation. Coming to the final state, the empty hole will be occupied by an electron. Absorption can be considered as a two-step process. In the first step, the angular momentum of the photon is transferred to the excited electrons from the spin orbit split $2p_{3/2}$ (L$_3$) and $2p_{1/2}$ (L$_2$) core states. The quantization axis of the spins of photoelectrons and X-ray photons is identical. Thus, spins of both systems are aligned parallel or antiparallel. In the second step photoelectrons make transitions into the 3d valence shell, thereby occupying available empty states.

In simple absorption experiments, one can observe differences in absorption spectra by applying positive and negative helicity $\sigma = \pm 1$. This change in absorption coefficients for two spin sorts is defined as the dichroic effect. In figure 4.1 the absorption for both spin sorts is depicted.

Dichroic effects in absorption can be considered in more detail within the framework of quantum physics. In a simple picture absorption is the transition of an electron from an initial to a final state after interaction with light quanta. In the one electron approximation, where the electron does not interact with the environment, the probability for a transition can be described with *Fermi's golden rule*.

$$
T_{if} = \frac{2\pi}{\hbar} \left| < f \left| \hat{H}_{int} \right| i > + \sum_n \frac{< f \left| \hat{H}_{int} \right| n >< n \left| \hat{H}_{int} \right| i >}{\epsilon_i - \epsilon_n} \right|^2 \delta(\epsilon_i - \epsilon_f)\rho(\epsilon_f)
$$

(4.1)

Here the first term denotes absorption, the second one, scattering processes according to time perturbation theory [34]. The transition matrix depends

on the applied photon energy. The energy conservation is included in the delta-function. ρ is the distribution of empty states, which in equilibrium obeys the Fermi-distribution. In the dipole approximation only interactions with the electric component of the electromagnetic field is considered. Therefore, $\hat{H}^{int} \sim \mathbf{p} \cdot \mathbf{A}$ with the momentum operator $\mathbf{p}$ and the vector potential $\mathbf{A}$.

The polarization of the electromagnetic wave, which leads to polarization dependent absorption, is included in $\mathbf{A}$. We know that $\mathbf{A} \sim \hat{\epsilon} \cdot e^{i\kappa r}$ with $\hat{\epsilon}$ the unit polarization vector and κ the wave vector. The exponential function can be extended into Taylor series where only the first term is considered. Thus, the final form of the transition matrix element will be approximately related to the term $< i\,|\mathbf{r} \cdot \hat{\epsilon}|\,f >$. Now the polarization and position vector should be expressed in an appropriate form according to the coordinate axis. In the case of solids, initial and final states are core level wave functions, Ligand Field wave functions and Bloch functions, respectively.

Using absorption spectra, one can calculate magnetic moments of the system using sum rules. The exact theoretical background can be found in publications of B. T. Thole and P. Carra et al. [18, 138]. Despite the complex phenomenon, very simple formulae for practical application can be extracted. In the case of transition metals, i.e. $2p \rightarrow 3d$ electron transitions have the following form:

$$m_{sp} = -\frac{6\int_{L_3}(I^+ - I^-)dE - 4\int_{L_3+L_2}(I^+ - I^-)dE}{\int_{L_3+L_2}(I^+ - I^-)dE}(1 + \frac{7}{2}\frac{\langle T_z \rangle}{\langle S_z \rangle})n_h\mu_{Bohr}$$

(4.2)

$$m_{orb} = -\frac{4}{3}\frac{\int_{L_3+L_2}(I^+ - I^-)dE}{\int_{L_3+L_2}(I^+ + I^-)dE}n_h\mu_{Bohr}$$

(4.3)

They disentangle spin 4.2 and orbital 4.3 moments. This formula has been proven by Chen et al. [20]. They measured the XMCD signal in transmission on a Fe sample and estimated orbital and spin moments applying sum rules. Integrals are calculated over the L_3 and L_2 resonances. I^+ is the intensity recorded parallel X-ray and electron spins. I^- describes the antiparallel case. n_h is the number of holes in the 3d-shell. The term $\langle T_z \rangle$ describes the magnetic dipole contribution. It corresponds to the quadrupolar spin density distribution. Nonetheless, when working with bulk materials this term can be neglected according to the theoretical calculation of R. Wu et al. [149]. To apply sum rules, absorption spectra have to be measured. Below, the method used for absorption measurements will be discussed. The magnetic moments of Co_2MnGa will estimated.

4.1.1 Total electron yield

X-ray absorption and dichroic effects on thin films can be measured in a simple way. This method is widely used. The transmitted X-rays passing the sample are analyzed. However, in the case of soft X-rays this requires extremely thin substrates with small absorption coefficients. We typically use 100 nm Al-foils or 100 nm Si substrates. Structures, which cannot be grown on these substrates, such as our Co_2MnGa Heusler alloy, fail to be analyzed in transmission geometry. The second possibility is the detection of the photo or electron current related to the absorption. The mechanism can be understood as follows. Absorbing an X-ray photon, a core electron is excited while leaving a core hole. This hole will be occupied by another electron from an energetically higher state. The process is accompanied by the emission of either electrons or photons. The measurement of the emitted photons is called fluorescence yield (FY). In the case of electron emission, the measurement method is called total electron yield (TEY). Auger or secondary electrons with energies larger than the work function can leave the sample and be detected. In this work we used TEY to analyze element specific magnetic moments in Co_2MnGa. Below we will give a theoretical overview regarding the related physical processes.

According to TEY, only electrons escaping from the sample surface can be detected. There is a certain probability that an electron can reach the surface. This depends on the mean free pass and the distance between excitation and surface. A mathematical expression for the number of electrons leaving the sample is given by [105]

$$dY_e = dY_0 exp[-z/\lambda_e] \qquad (4.4)$$

with the electron escape depth λ_e and the number of secondary electrons dY_0 created in a layer of thickness dz at a distance z from the surface. Hence, dY_0 can be summarized as follows [105]:

$$dY_0 = I_0 G \frac{\mu}{cos\theta} exp[-\mu z/cos\theta]dz \qquad (4.5)$$

with absorption coefficient $\mu(\theta, E)$, which is angle dependent according to the expression $\mu(\theta, E) = \mu/cos\theta$. G is the averaged number of secondary electrons in a cascade initiated by a single Auger electron. Now dY_0 can be inserted in dY_e and integrated over the sample thickness dz. The result of this integration will be the TEY intensity. Integration boundaries can be set from $z = 0$ to $z = \infty$. The final form of TEY intensity is

$$I_{TEY} = \frac{I_0 G \mu \lambda_e}{\lambda_z} \frac{1}{\lambda_e/\lambda_z + 1}. \qquad (4.6)$$

λ_z describes the attenuation depth of X-rays incoming along the x-direction. It depends on the absorption coefficient μ and the incidence angle θ as
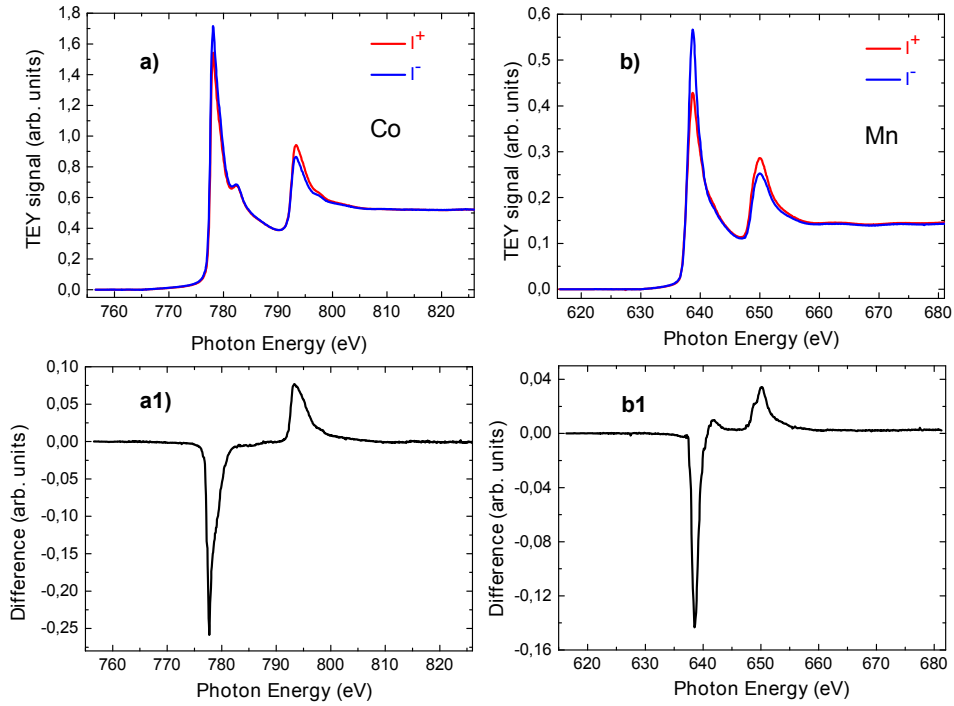
Figure 4.1: *TEY spectra measured for a) Cobalt and b) Manganese near L_3 and L_2 absorption edges for both orientations of magnetization. a1) and b1) difference.*

$\lambda_z = cos\theta/\mu$. Depending on the relation between electron escape depth λ_e and attenuation depth λ_0, TEY intensity has two limiting cases. If $\lambda_z >> \lambda_0$, then $I_{TEY} = I_0 G \lambda_e \mu / cos\theta$. In the second case, where $\lambda_z << \lambda_e$, $I_{TEY} \approx I_0 G \lambda_e / cos\theta$. In the latter case, TEY is independent of the absorption coefficient. This is the evidence for saturation. Saturation effects may lead to the underestimation of magnetic moments and therefore should be seriously taken into account.

Experimental results and magnetic moments

TEY of Co_2MnGa has been measured at BESSY II facility using circular polarized X-rays on PM3 beamline [71, 72]. The spectra are depicted in figure 4.1. The angle between incident X-ray and the surface used for measurement was 25°. Saturated magnetic field was used to change the magnetization while the helicity of the X-ray was fixed. All technical details of this measurement techniques are published in [1]. Measurements were performed at room temperature. Tunable energy made it possible to measure spectra near L_3 and L_2 edges for chemical elements Cobalt and Manganese

and estimate magnetic moments applying sum rules. Spectra measured for the Co_2MnGa sample is depicted in figure 4.1. Spectra have been normalized to the ecran in order to subtract fluctuation and decay in the ring current. Applying sum rules magnetic moment for Manganese and Cobalt were estimated separately, in units of μ_B $m_{Co} = 0,5965$ and $m_{Mn} = 1,8729$ respectively. The relation between $m_{Co} : m_{Mn}$ is 1:3. This relation is in agreement with the calculations and measurements reported so far. Small values of the magnetic moments we refer to the saturation effects explained previously.

4.2 X-ray reflectivity as probe tool for magnetism

In this section we introduce experimental results and theory on specular X-ray reflectivity. In these experiments we measured the integral intensity of the reflected light. This means that the measured signal includes elastic and non-elastic components of the scattered X-ray quanta. We worked out a procedure for the treatment of the recorded signal. Hence, we can extract magnetic and non-magnetic contributions from the measurement and use it with perspective to the dynamical pump-probe measurements.

First we define I^+ and I^- signals. These are reflected intensities recorded for two opposite magnetization directions. The magnetization vector lies in the sample's surface parallel to the plane of incidence. Subsequently, we define sum- and difference signals, so that sum-signal includes pure charge dynamics and difference according to magnetization dynamics and will explain it below. The parameter space appropriate for dynamical measurements will be established and discussed in this chapter. All static experiments were performed with the aim of figuring out suitable conditions for pump-probe experiment in reflection geometry.

4.2.1 Reflectivity vs. absorption

In previous sections, the effect of magnetic dichroism on the absorption spectra has been considered. The origin of this effect lies in the spin dependent absorption of circularly polarized X-ray quanta and consequent excitations from 2p into 3d levels in transition metals. Different occupation rates of 3d minority and majority bands lead to different intensities in the absorption spectra. This effect can be used to estimate the total magnetic moment and the quantitative analysis of its spin and orbital contributions. XMCD can be applied in absorption experiments, i.e transmission spectroscopy and, indirectly, in case of TEY. In both cases a specific optical response of the material is used and mostly the absorption coefficient influences the measurement process.

We have already mentioned the role of the sample thickness on the TEY signal. In the case of transmission experiments, this parameter is of major

importance as well. Therefore, the thickness of samples measured in transmission geometry is typically of some tens of nanometers. It preserves homogeneous pumping of the sample and a feasible measured signal. Samples grown on thick substrates like Co_2MnGa are not appropriate for measurements in transmission experiments. Particularly in the soft X-ray regime used at the BESSY II synchrotron facility. Nevertheless, there is an interest to preserve chemical specificity of X-ray absorption spectroscopy (XAS) and simultaneously allow an investigation into materials grown on thick substrate, e.g. single crystals. In this thesis, we propose to probe magnetization dynamics in reflection geometry using XMCD effect. By this technique we have to overcome certain problems and define conditions or experimental parameters for measurements.

First, we would like to make some preliminary considerations. The optical response of matter to electromagnetic irradiation can be described by the macroscopic optical constant. In X-ray region it takes the form:

$$n = 1 - \delta + i\beta \tag{4.7}$$

with components depending on frequency and polarization of the X-rays. In conventional transmission or TEY experiments, there is access mostly to the absorption coefficient β. This follows from simple considerations of the propagating electromagnetic wave in matter. The spatial component of the electric field can be described as

$$E = e^{in\kappa z} \tag{4.8}$$

Here we show the E vector normalized to one, which propagates in z direction. Here, κ is the wave vector and n the refractive index. Using 4.7 this equation can be expanded into

$$E = e^{i\kappa z}e^{i\delta\kappa z}e^{\beta\kappa z} \tag{4.9}$$

In this expression, all three components have their own contribution: initial amplitude E_0, phase shift, and absorption, respectively. Therefore, the intensity can be written as

$$E^* \cdot E = |E_0|^2 e^{-2\beta\kappa z} \tag{4.10}$$

and this is the exactly expression for the intensity absorbed in the matter:

$$I(z) = I_0 e^{-\mu z} \tag{4.11}$$

It is evident that $\beta = \mu/2\kappa$. As we can see, it is possible to extract information about the absorption coefficient directly from the transmission experiment and this, in turn, is related to the magneto dichroic effect. It allows one to apply sum rules and directly calculate magnetic moments.

In reflection geometry, the intensity of the reflected X-ray beam is additionally affected by the index of refraction δ. The index of refraction depends on the orientation of the magnetization. Therefore, it is correct to write it as

$$n^{\pm} = 1 - (\delta \pm \Delta\delta) + i(\beta \pm \Delta\beta) \qquad (4.12)$$

with $\Delta\delta$ and $\Delta\beta$ representing magnetic contributions to the coefficients. While in transmission experiment one has direct access to the $\beta \pm \Delta\beta$, in reflection the analysis becomes difficult through additional parameter $\delta \pm \Delta\delta$. In our experiment, we want to use a fixed circular polarization of the incident light. Subsequently, we measure the intensity of X-rays reflected from the surface and postulate to disentangle magnetic dynamics from charge contributions. Subsequently, we are able to provide the time resolved demagnetization and estimate demagnetization parameters.

4.2.2 Reflectivity experiments

As postulated, we want to gain information from the reflectivity measured for two opposite magnetization orientations. The circular polarization of the X-ray has to be fixed. Therefore, the dichroic effect in reflectivity has to become apparent as in absorption. It must be proven. Thus, we start with reflectivity spectra at different angles and investigate how they changes. We show, how big the dichroic effect doe to the ferromagnetic order in the Co_2MnGa on elements Co and Mn is and at which photon energies. We introduce reflectivity measurements for different photon energies and figure out the appropriate angle. At this angle the distinction between charge and magnetic contribution will be substantiated. We additionally present hysteresis curves to verify ferromagnetic order in our Heusler-alloy.

Reflectivity spectra

We begin with a consideration of reflectivity spectra near the L_3 and L_2 edges of Cobalt and Manganese. In figure 4.2 and 4.3 we depicted reflectivity spectra for different angles. Here we used circular polarization. Measurements were performed in an external magnetic field, which was applied parallel to the sample surface and to the incident plane. Each spectrum was recorded for two different magnetization orientations while the helicity of the X-ray photons remained unchanged. We designate these spectra as I^+ and I^-. In figures 4.2 and 4.3 the angles are given with respect to the sample surface. We can see that dichroic effect in reflectivity spectra is evident. This means that we observe reflected signal dependent on magnetization orientation. It is comparable with absorption spectra, see 4.1. For non-resonant photon energies blue and red lines are identical. Near resonant photon energies (L_3 and L_2 edges) the difference becomes significant.
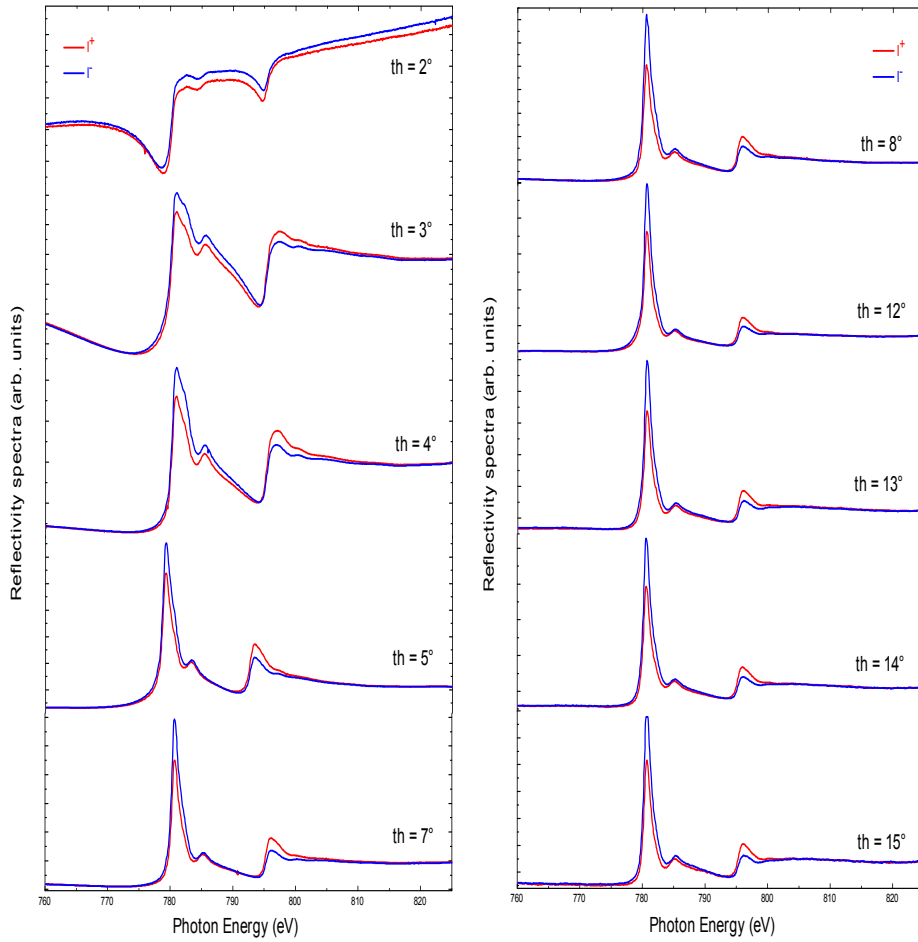
Figure 4.2: *Reflectivity spectra measured for Cobalt near L_3 and L_2 absorption edges for both orientations of magnetization. We define it as I^+ red line and I^- blue line.*
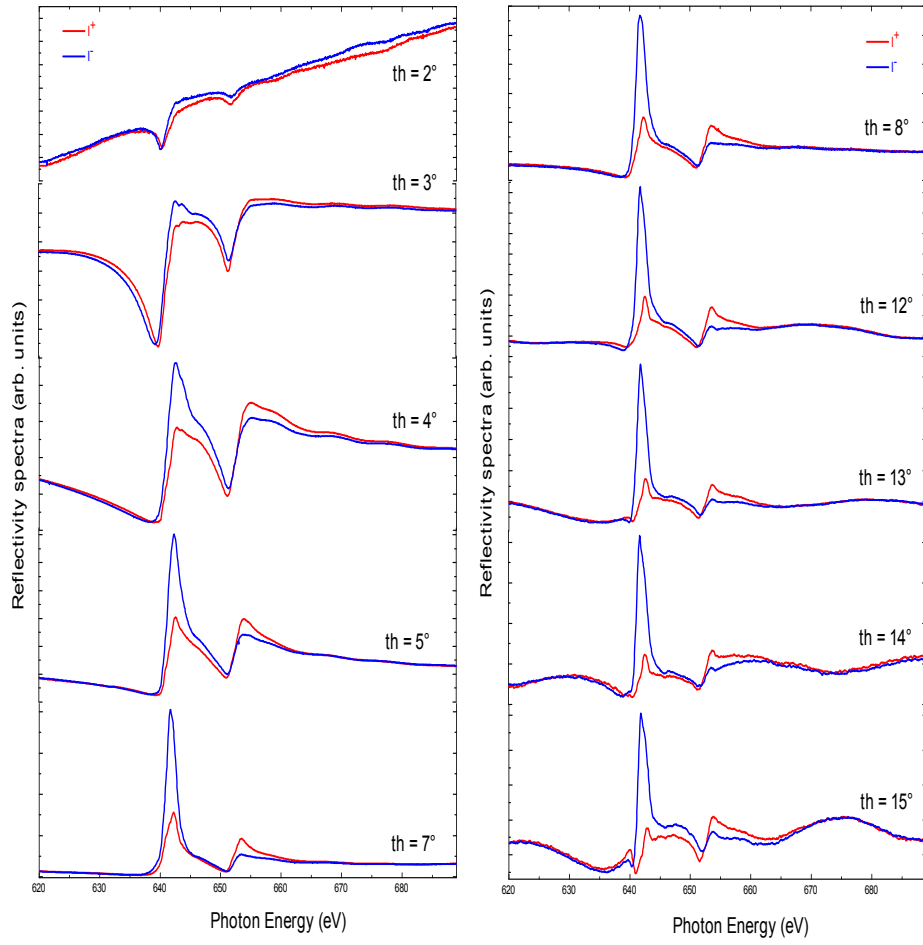
Figure 4.3: *Reflectivity spectra measured for Manganese near L_3 and L_2 absorption edges for both orientations of magnetization. We define it as I^+ red line and I^- blue line.*

We have to mention that in figures 4.2 and 4.3, the scale of the ordinate axis is different for all angles. It means that one cannot see absolute intensity and therefore compare magnitude of the reflected spectra. The aim is to show spectra shape at various angle positions. Generally, with the increas of the angle, the reflected intensity decreases.

At angles between 7° and 8°, the shape of the spectra is very similar to the absorption spectra in figure 4.1. The dichroic effect ΔI due to the magnetization orientation is also apparent. At small angels 2° - 4° surface effects as roughness and broken translation symmetry become significant. At these angles, the spectra undergo a substantial change of the spectral shape. Below a certain angle (between 2° and 3° for Co and between 3° and 4° for Mn, intensity dips appear at the L_3 and L_2 absorption edges. Above these angles, the resonances are seen as intensity peaks. The angle under discussion is the photon energy dependent critical angle or angle of total reflection [58].

With larger angles of incidence, the penetration depth of the X-rays into the sample increases. In this case, reflection takes place on several sublayers and thus their superposition reflects a less surface sensitive picture. For incidence angles above about 9°, intensity oscillations become visible in the spectra, in particular for Mn. We assign these variations to interference effects at the cap layer.

From these measurements we see that only in narrow angle regions, namely between 7° and 8° degree, the reflectivity spectra is comparable with absorption spectra. At these angles, we stay away from critical angles and interference effects, significant for Manganese. The dichroic effect is thereby preserved. Now we have to work up procedure for the signal treatment and disentangle magnetic and charge contribution.

Magnetic and charge contribution, proceeding of data treatment

We define the sum of I^+ and I^- as $\sum I = I^+ + I^-$. This expression determines the non-magnetic part of the reflection, as will be discussed in more detail later on. The difference $\Delta = I^+ - I^-$ represents the magnetic contribution to the reflectivity. We postulate this hypothesis and consider how this signal changes over the angle at a fixed photon energy. For this reason we took certain photon energy values for X-ray photons and fixed them. Subsequently we performed reflectivity measurements. Energies involved into the measurements are depicted in figure 4.4. Our choice was done for resonant and non-resonant energies. We performed these measurements for both magnetization orientations, those parallel and antiparallel to the X-ray propagation. We calculated the sum (non-magnetic) and difference (magnetic) signal and normalized their maximum to one.

In figures 4.5 and 4.6 one can see the results of this calculation. The blue line is for sum-signal and the red line is for difference-signal. For non-
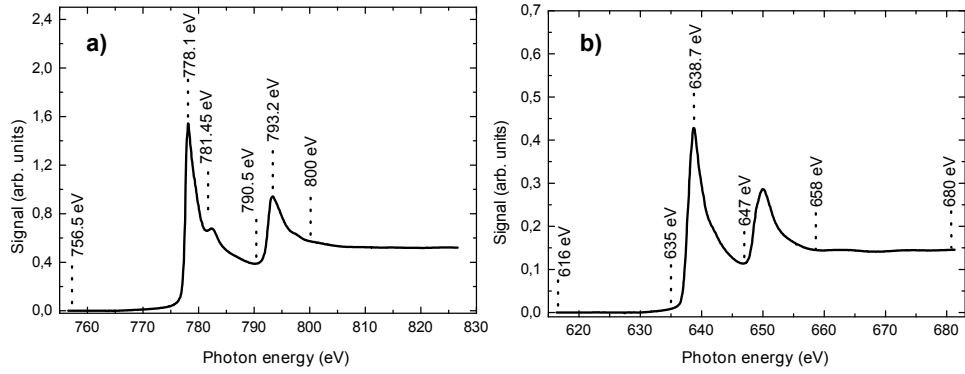
Figure 4.4: *Absorption spectra measured by means of TEY technique near the L_3 and L_2 absorption edges: a) Cobalt b) Manganese.*
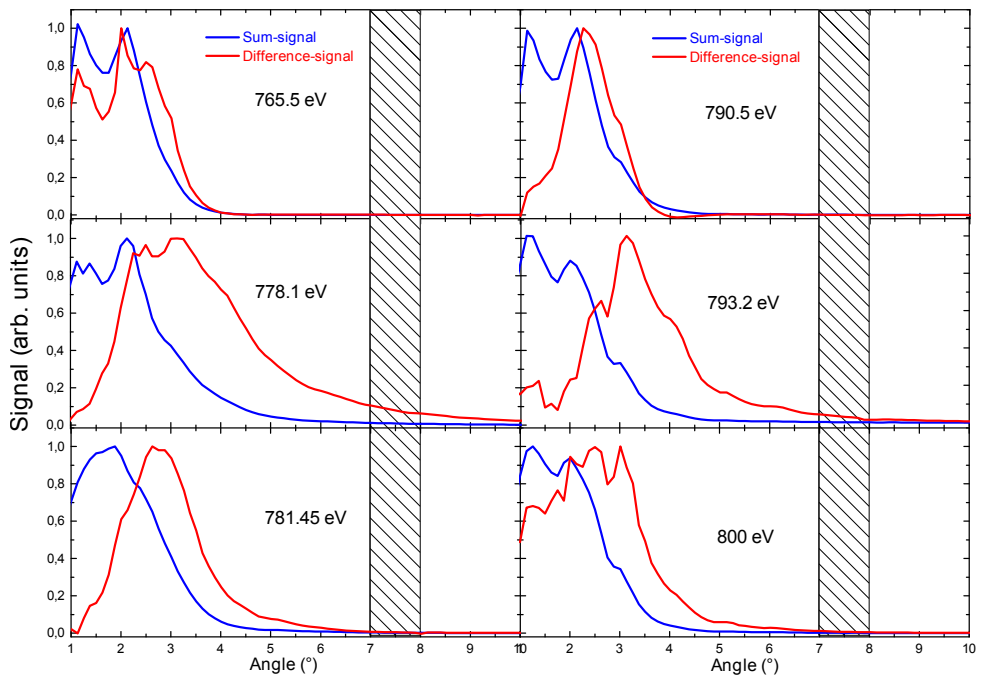

Figure 4.5: *Normalized to one sum and difference for reflectivety signals measured for different X-ray photon energy. Energy is labeled in the figure. In the figure 4.4 energy position can be found. Measurements were performed near the L_3 and L_2 absorption edges of Cobalt.*
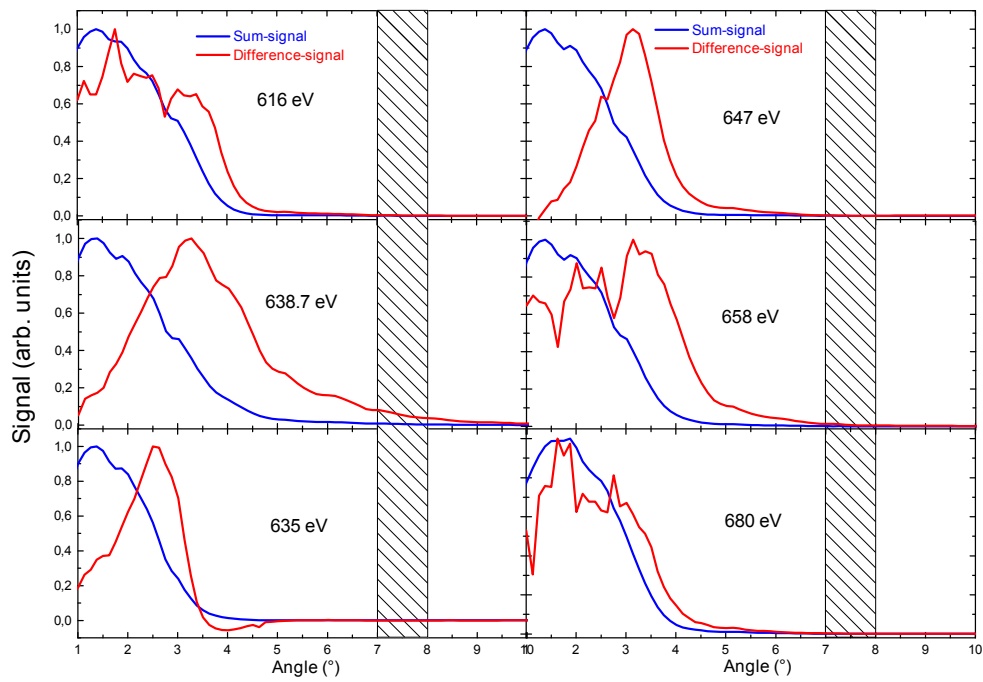
Figure 4.6: *Normalized to one sum and difference for reflectivety signals measured for different X-ray photon energy. Energy is labeled in the figure. In the figure 4.4 energy position can be found. Measurements were performed near the L_3 and L_2 absorption edges of Manganese.*
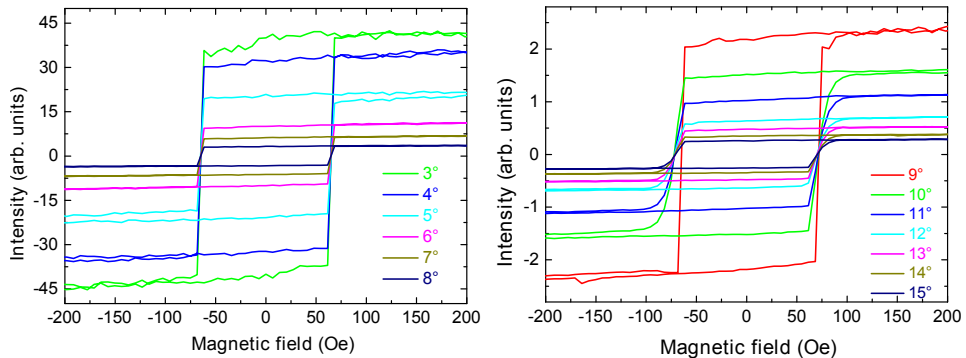
Figure 4.7: *Hysteresis measured at different angle for constant energy tuned to L_3 edge for Cobalt.*

resonant energies there is no difference between magnetic and non-magnetic signal starting from 5.5° up to higher angles. We do not consider this region for smaller angles. We know that there we are in the area of a critical angle. We therefore conclude, that the magnetic contribution to the reflectivity for non-resonant energies disappears. In the case of resonant energies we see that magnetic and non-magnetic lines are different, especially in the region between 7° and 8°. Magnetic reflectivity becomes significant and overcomes pure charge reflectivity. For Cobalt there are energies 778.1 eV and 793.2 eV corresponding to L_3 and L_2 edges respectively. For Manganese 638.7eV corresponding to the L_3 absorption edge. As we already mentioned in previous subsection between 7° and 8° the spectra is comparable to its natural absorption shape.

According to the treatment of the signal proposed in this subsection, we can disentangle the magnetic and non-magnetic contribution from the reflected signal. We should build sum (non-magnetic) and difference (magnetic) between I^+ and I^- and normalize the maximum of both to the one. From the reflectivity measurement we should figure out regions with a maximum difference. In the next step we substantiate this statement with theory.

Hystereses

In figures 4.7 and 4.8 are hysteresis recorded for fixed circular polarization of an incoming X-ray at different incident angles. Energy was tuned to the L_3 edge for Manganese and Cobalt and remains constant. Hysteresis were shifted to the common zero point. Therefore, we can consider the relative changes of reflected intensity depending on the incident angle. With the increase of the incidence angle, the reflected intensity decreases. Beginning at 7°, the penetration of the X-ray into the sample's surface becomes significant. As a result we see that hysteresis change their shape. They are
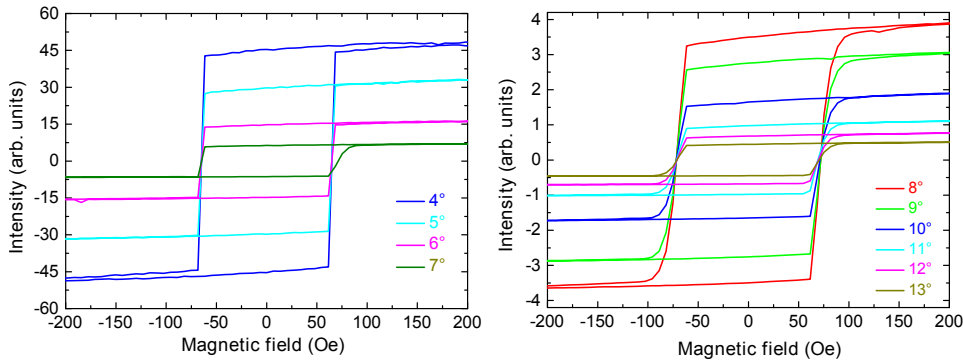
Figure 4.8: *Hysteresis measured at different angle for constant energy tuned to L_3 edge for Manganese.*

not more rectangular. The coercivity field is increased and hystereses have a slope on the place of maximum coercivity. We suppose that this can be explained as follows. Penetrating deeper into the sample, the X-ray interacts with more magnetic domains. So, upon changing the magnetic field orientation, will not flip later instantaneously but remain their orientation. To orient all domains one has to apply higher magnetic field. This leads to the higher coercivity field. At small angles, the X-ray interacts statistically with a smaller number of domains. Hence, in average, they flip at a certain coercivity field simultaneously. It makes hysteresis rectangular. From the hystereses shape we conclude that they all exhibit ferromagnetic behavior independently on the angle. The Co_2MnGa material has an in-plane easy-axis magnetization. The rectangular forms of hystereses are an indication of this particular magnetization.If we base our hypothesis on the consideration of the hystereses's form, we can argue that this Heusler structure is a single domain structure.

All kinds of reflectivity measurements presented in this chapter make clear that Co_2MnGa has a ferromagnetic order, verified by the hystereses. Due to the dichroic effect we can consider magnetization dependent changes in the reflectivity spectra. We see a different reflected intensity of the X-ray beam at L_3, L_2 edges for two different magnetization directions in the spectra. This is similar to the absorption spectra we measured with absorption spectroscopy by means of TEY. From the preliminary consideration of the spectra, we conclude first that the appropriate angle for measurements is between $7°$ and $8°$. In this range we are far away from the critical angle.

On the other side, we are not in the region where interference effects make significant impact on the spectra's shape. Therefore, the spectra are similar to the absorption spectra. Additionally, in this angles region, the spectra are not affected by surface effects. We see that at resonances dichroic effect

has its maximum. Intuitively we suppose that the magnetic response of the sample in pump-probe measurements has to be measured at resonance. This point will be substantiated in the following chapter.

4.2.3   Theoretical overview

In the section 4.2.2 we presented the results of static reflectivity experiments. By means of spectra and reflectivity measurements for resonant and non-resonant energies, we supposed that it is possible to disentangle magnetic and non-magnetic contribution to the reflected signal. It is possible for a certain angle range and resonant energies. Additionally, reflectivity has to be measured for both parallel and antiparallel magnetization directions. Then, the difference-signal is proportional to the magnetic and sum-signal to the non-magnetic contribution to the reflected signal. In this section we consider some theoretical approaches and verify this thesis.

Magneto-optical approach

Magneto-optical effect in a visible range was established as a powerful tool for the investigation of ultrafast magnetism. Due to the sample's magnetization incoming light changes its phase and amplitude and finally polarization after reflection. The degree of polarization can be analyzed and attributed to the magnitude of the magnetization [114]. Theoretically, changes in the polarization can be described with reflection matrix $\hat{\mathbf{r}}$. Components of this matrix depend on the geometry of the experiment. So mostly known MOKE families are transversal (T-MOKE) longitudinal (L-MOKE) and (P-MOKE) polar. In T-MOKE magnetization is perpendicular to the incidence plane while in L-MOKE magnetization lies in the incidence plane. In both cases magnetization is parallel to the sample's surface. In P-MOKE the vector of magnetization is perpendicular to the surface. We performed our experiments in L-MOKE geometry so we restrict our attention on this special case and consider boundary between vacuum and magnetic surface. The initial electromagnetic irradiation is incident on the sample's surface from the vacuum. In figure 4.9 the geometry of the experiment is defined. The electric component of the reflected field can be transformed according to [100]

$$\mathbf{E}_r^{\pm} = \begin{pmatrix} \hat{r}_{ss} & \pm\Delta_{sp} \\ \mp\Delta_{ps} & \hat{r}_{pp} \end{pmatrix} \mathbf{E}_i \tag{4.13}$$

with $\mathbf{E}_i$ and $\mathbf{E}_r$ incoming and reflected electric field respectively. Non-diagonal components of the matrix contribute to the magnetization dependent changes in polarization. Plus and minus are attributed to the orientation of the magnetization. We would like to note, that all components of this matrix are a complex function, as such one has to keep it minded by the matrix calculus. Vector $\mathbf{E}$ can be decomposed into the orthogonal
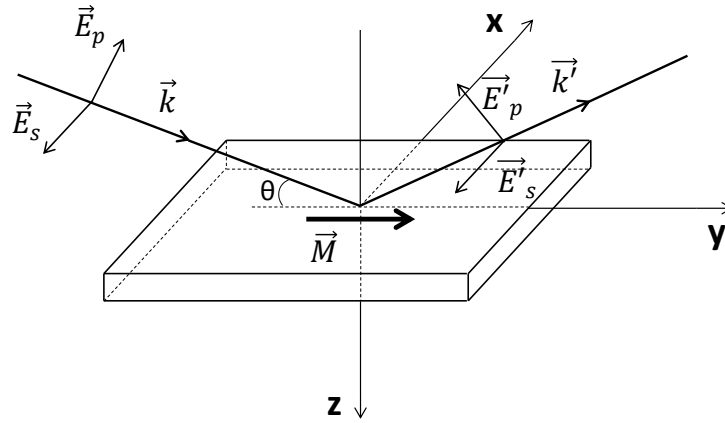
Figure 4.9: *Experiment in reflection geometry. Boundary between vacuum and magnetic matter with the in-plane magnetization $\boldsymbol{M}$. In this experiment the vector of magnetization is in the plane of incidence. The wave vector $\vec{k}$ build an angle θ with the sample's surface and the magnetization's vector. Additionally to the global coordinate system (xyz) the local rectangular system for the incoming and reflected waves is defined. The basis of this system are vectors $\vec{E}_p$ in the incidence plane, $\vec{E}_s$ normal to the plane of incidence and the wave vector $\vec{k}$. Sample is magnetized along the axis $\boldsymbol{y}$. The basis for the reflected wave is defined with $\vec{E}'_s$, $\vec{E}'_p$ and $\vec{k}'$.*

components $\mathbf{E} = \mathbf{E}_s + \mathbf{E}_p$. These vectors are defined in the figure 4.9. $\mathbf{E}_p$ lies in the plane of incidence and $\mathbf{E}_s$ is perpendicular to the plane of incidence. The action of the reflectivity matrix on the vector $\mathbf{E}_i$ represents changes in the magnitude and in the phase of the components of electric fields in a local coordinate system. In the visible range it is quite easy to analyze the polarization of the reflected light, for instance with a Wollaston prism. In the soft X-ray regime it is difficult due to the photon losses, even with X-ray optics. Our aim is to evaluate magnetic contribution in the reflected intensity using calculus developed in the magneto-optics.

Thus, we do not analyze the polarization of the reflected beam but measure its intensity. This intensity I_r is proportional to the $\mathbf{E}_r^* \cdot \mathbf{E}_r$. The incoming circular polarized light can be written in the form $\mathbf{E}_i = \frac{1}{\sqrt{2}} E_0 (\hat{e}_s + i\hat{e}_p)$. Now one can calculate or use reference [100] and see how I_r depends on the components of the reflection matrix. This cannot help for further application and analyzing of magnetic signal due to the complicity of the entire expression. So we calculate in the next step the sum signal of the intensities for both magnetization orientations. Let's define as I^+ and I^- the amplitude of the signal recorded for magnetization parallel and antiparallel to the projection of $\vec{k}$ on the $\mathbf{M}$. So the sum is $I^+ + I^-$ can be expressed as:

$$I^+ + I^- = I_0 \cdot (|r_{ss}|^2 + |r_{pp}|^2 + 2|\Delta_{sp}|^2) \tag{4.14}$$

Here, the following relation $\Delta_{sp} = -\Delta_{ps}$ [106] is used. Terms $|r_{ss}|^2$ and $|r_{pp}|^2$ are non-magnetic Fresnel's reflectance R_s and R_p. They can be expressed in terms of index of refraction $\hat{n}$ see 4.7 and the incidence and refractive angle. In the magneto-optics index of refraction is not only one quantity which determines response to the irradiation. Response to the magnetic contribution is described with magneto-optical constant $\mathbf{Q}$. This is a complex function and depends on the wavelength. As we already wrote previously, the index of refraction in external magnetic field gets additional components see equation 4.12. There is a relation between $n^{\pm}$ and $\mathbf{Q}$: $n^{\pm} = \hat{n}(1 \pm \frac{1}{2}\mathbf{Q}\cos(\vec{k}, \mathbf{M}))$. This relation is valid to first order approximation in $\mathbf{Q}$ [114].

Magnetic contribution Δ_{sp} is very small quantity [114]. In the expression 4.14 it is in power of two. It makes this quantity negligible compare to the diagonal coefficients. The main impacts on the signal make Fresnel coefficients $|r_{ss}|^2$ and $|r_{pp}|^2$. In the first order in $\mathbf{Q}$, they depend on the unperturbed refractive index $\hat{n}$ see 4.7 as:

$$r_{ss} = \frac{E_s^r}{E_s^i} = \frac{\sin\theta - \sqrt{\hat{n}^2 - \cos^2\theta}}{\sin\theta + \sqrt{\hat{n}^2 - \cos^2\theta}} \tag{4.15}$$

$$r_{pp} = \frac{E_p^r}{E_p^i} = \frac{\hat{n}^2 \sin\theta - \sqrt{\hat{n}^2 - \cos^2\theta}}{\hat{n}^2 \sin\theta + \sqrt{\hat{n}^2 - \cos^2\theta}}. \tag{4.16}$$

In these equations only a pure index of refraction $\hat{n}$ is used without magnetic contribution compare to $n^{\pm}$ in 4.12. We rewrote this equation
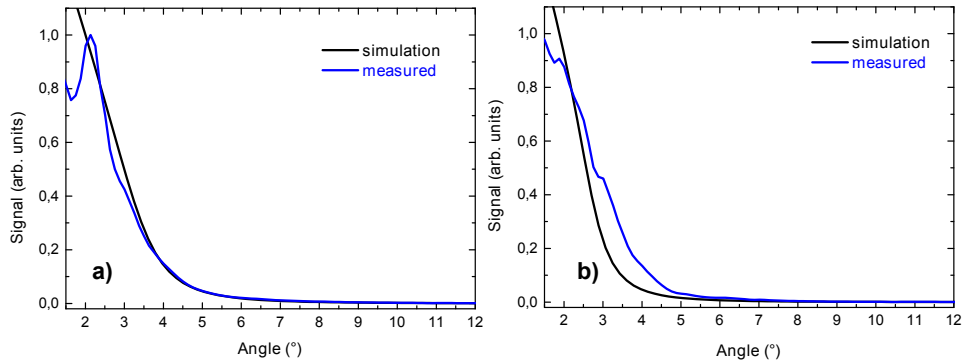
Figure 4.10: *Sum for reflectivity measure (solid blue line) and simulated (black solid line) using index of refraction. a) L_3 resonance for Cobalt b) L_3 resonance for Manganese.*

for only the incidence angle using Snell's law. The equation 4.14 describes very well the behavior of the sum signal. Using the values for the index of refraction n which we got from the simulations described in other sections section, we can simulate reflection on the surface. This picture is simplified and considers only one boundary between vacuum and the magnetic solid. See figure 4.10 to compare measured and simulated sum-signal. By simulating the sum signal we used only r_{ss} and r_{pp} coefficients without Δ_{sp} contribution. It is in correlation with measured curves see figure 4.10. For the L_3 resonance on Manganese measured curve is shifted slightly. As we already know from previous sections it might be due to the higher magnetic contribution compared to Cobalt. The magnetic moment of Manganese is higher. Nevertheless, near the angles $7°$ and $8°$ the contribution of Δ_{sp} is insignificant for the sum signal. We can see it on the simulated and measured curves. In the case of a stronger magnetic contribution on the reflectivity we would get a mismatch between lines. Consequently, we can conclude, that the sum signal reflects, approximately, the pure electron's dynamics by the pump-probe experiments.

The difference between reflected intensities has the following form

$$I^+ - I^- = 2I_0 \cdot Im(-\Delta_{sp}^*(r_{ss} + r_{pp})) \tag{4.17}$$

Compare in [100]. As we can see, this equation is more complex for analysis. To simulate the difference signal one needs to know the magneto-optic constant **Q** and link it to Δ_{sp}. The difference signal is a mixture between real and complex components between Δ_{sp} ,r_{ss} and r_{pp} coefficients. It makes the simulation more difficult. In the following section, we will show that it is possible to connect the difference and the sum signal to microscopic quantities like permittivity and afterword to the index of refraction.

Formalism of the Resonant X-ray scattering (RXS) and microscopic origin of the magnetic dichroism

In this section we would like to mention briefly the origin of magnetic dichroic effects which we consider by the reflection of the X-ray on the surface. In contrast to the magneto-optic approach, here we would link it to the microscopic or even to the spectroscopic parameters coming from the quantum mechanics consideration. In further sections we combine microscopic and macroscopic description.

Reflectivity is a particular case of the scattering. Every scattering process is characterized by the quantity named *differential scattering cross section*, independent of whether one considers particles or electromagnetic waves. Conventionally, the cross section is proportional to the electron density but it is also possible to reflect the magnetic density by certain conditions even in the soft X-ray radiation range.

So in soft X-ray region there are two different scattering regimes of importance, resonant and non-resonant scattering, dependent upon whether applied photon energy is comparable to the electron transition energy or not. Other important cases are elastic and inelastic scattering events dependent on whether the energy of the scattered photon is going to change or not. *M. Blume* verified that if the photons energy is of amplitude of binding energy of electrons, then in magnetic materials the resonant magnetic scattering effects can be enhanced [15]. This means that in the presence of magnetic order, additional terms in differential cross section due to the local magnetic moment, can reach amplitude enough to be disentangled from a pure charge contribution.

In the case of the X-ray scattering on single crystals, the differential cross section has common form [111]

$$\frac{d\sigma}{d\Omega} = \left| \sum exp(iQr_n) f(Q, \hbar\omega) \right|^2, \qquad (4.18)$$

where $\hat{Q} = \hat{k} - \hat{k}'$ is the photon momentum transfer for incoming and scattered wave vector respectively $\hat{k}$ and $\hat{k}'$, and $\hbar\omega$ is the photon energy and $f(Q, \hbar\omega)$ scattering amplitude. As we can see in equation 4.18, the cross section depends on the transition matrix expressed in equation 4.1.

To calculate the differential cross section one needs to know the Hamiltonian which describes the problem. According to the rules of the quantum electro dynamics, this Hamiltonian can be expressed in terms of the unperturbed systems atoms and photons and in terms of their interaction. These expressions are complex. By interest we refer the reader to [15].

Putting the explicit form of the Hamiltonian into the 4.1 one can get differential cross section or the expression for the scattering amplitudes. This equation would contain all scattering cases of interest resonant and non-resonant as well elastic and inelastic. Taking into account the specification

of the problem, one can calculate a cross section, thereby simplifying the equation.

The non-resonant case was already considered in the work of M. Blume [15], where he calculated the ration of pure charge and magnetic cross section. According to this calculation this was $\sigma_{mag}/\sigma_{charge} = 4 \times 10^{-6} < \mathbf{s} >^2$. We are interested in terms which have contribution to the resonant part of the scattering amplitude by elastic scattering.

In the resonant case the energy of the X-ray photon is near to the energy of the intermediate state. By means of these states the scattering of the quantum proceeds into the final state. These intermediate states might be holes over the Fermi energy or electrons under the Fermi energy. The occupation number of these states in a ferromagnetic are different for different spin sorts and are therefore differently involved in the transition process. Hence, the differential cross section should be different for minority and majority states. This is, in turn, the origin of the different amplitude of the reflectivity signal for parallel and antiparallel magnetization.

The calculation of the transition matrix elements can be made with a different approximation order. In dipole approximation it has been successfully done and we refer to the work of J. P. Hill et al. [59] and J. P. Hannon et al. [55]. Wave functions used for estimation matrix elements have to be expressed in terms of atomic orbitals with radial components $R_{n,l}(r)$ and spherical harmonics $Y_{l,m}$ for angular momentum and χ_{s,m_s}. For $2p$ states with strong spin-orbital splitting the *Glebsch-Gordon* coefficients become very helpful. In this representation spin-orbit coupling terms can be linearized and expressed in form of linear combination of uncoupled terms. Dipole selection rules have to be taken into account.

Dipole approximation is one of the simplest for the calculation of scattering amplitudes. As such, the scattering amplitude in resonant case for the dipole $E1$ transition with $l = 1$ and $m = 0, \pm 1$ can be written as

$$f_n = (\hat{\epsilon}' \cdot \hat{\epsilon})F^{(0)} - i(\hat{\epsilon}' \times \hat{\epsilon}) \cdot \hat{z}_n F^{(1)} + (\hat{\epsilon}' \cdot \hat{z}_n)(\hat{\epsilon} \cdot \hat{z}_n)F^{(2)} \qquad (4.19)$$

with

$$F^{(0)} = (3/4k)[F_{11} + F_{1-1}] \qquad (4.20)$$

$$F^{(1)} = (3/4k)[F_{11} - F_{1-1}] \qquad (4.21)$$

$$F^{(2)} = (3/4k)[2F_{10} - F_{11} - F_{1-1}] \qquad (4.22)$$

All three terms in 4.19 have their contribution to the scattering. The first term does not include magnetic moment and therefore it describes contribution to the charge Thomson-Bragg scattering. The second term depends on 4.21 so transition matrix element for left and right circular polarized light. Additionally, there is a term which is the product of X-ray polarization vector and magnetization direction. Therefore, 4.21 is responsible for

magnetism dependent scattering and describe XMCD effect by scattering. The last term in 4.22 is responsible for *X-ray magnetic linear dichroism* (XMLD) effect. The equation 4.19 for the scattering amplitude, delivers a clear relation between the incident and reflected polarization of the X-ray and the microscopic origin of this polarization dependent scattering.

The formalism of the resonant magnetic scattering delivers the origin of the dichroic effect described by the second term in the equation 4.19. On the other side we do not have a direct access to the microscopic quantities from the experiment. We perform our experiment in reflection geometry and mostly we measure reflected intensity of X-ray which is $I \sim |E|^2$. Due to the square operator phase, information is going missing. To obtain a full picture about reflected light, one needs to analyze reflected polarization components separately. Our aim is to show, that at a certain angle, the magnetic information in measured intensity of a reflected X-ray is dominant, so that we can use resonant reflectivity of a circular polarized X-ray as a probe for magnetism even without anlalysator for the reflected beam.

We will show in the next subsection that microscopic parameters are included in the macroscopic one. This is index of refraction. In the difference signals only contributions from non-diagonal elements of the refraction index are involved. And non-diagonal elements are linked to the magnetic contribution to the reflected light.

Formalism of Resonant Reflectivity

In the previous section the quantum mechanics picture for the resonant magnetic scattering has been introduced. In experiments we measure signals and dependent on changes in this signal we try to understand what is happening in the matter. More helpful for us are macroscopic quantities, like the index of refraction. So in the section about magneto-optics we saw that we can use it to describe reflectivity and the contribution of matrix elements to the reflectivity signal. It is also possible to connect macroscopic quantities and spectroscopic quantities described in the section on resonant scattering.

Reflectivity is a particular case of scattering. As we already saw the response to the light irradiation can be described with refraction index which is appropriate for macroscopic description. This quantity can be linked to the electric permittivity ε which is good for microscopic treatment. In the soft X-ray regime the relation between the index of refraction n and the electric permittivity ε can be expressed in the equation [36]

$$n \approx \sqrt{\varepsilon \pm i\varepsilon_{x'y'}} \qquad (4.23)$$

with x' and y' local coordinate system being linked to the incident wave. The electric permittivity is related to the scattering amplitudes already defined

in a previous section [36]:

$$\varepsilon = 1 + \frac{4\pi}{k_0^2}\rho F^{(0)} \tag{4.24}$$

$$\varepsilon_{xy} = -i\frac{4\pi}{k_0^2}\rho u_z F^{(1)} \tag{4.25}$$

$$\varepsilon_{xz} = i\frac{4\pi}{k_0^2}\rho u_y F^{(1)} \tag{4.26}$$

$$\varepsilon_{yz} = -i\frac{4\pi}{k_0^2}\rho u_x F^{(1)} \tag{4.27}$$

In this equation u_i is a unit vector in direction of magnetization, k_0 wave vector of the X-ray and ρ number of atoms per unit volume. If we put these expressions into the equation 4.23 we will get the result

$$n^{\pm} \approx 1 + \frac{4\pi}{k_0^2}\rho(F^{(0)} \pm \hat{k} \cdot \mathbf{u}F^{(1)}) \tag{4.28}$$

As we can see the magnetic contribution to the index of refraction is described though $\pm\hat{k} \cdot \mathbf{u}F^{(1)}$. Scalar product $\hat{k}_0 \cdot \mathbf{u}$ describes projection of the wave vector on the magnetization direction in the solid. Thus, this expression links macroscopic quantity like the index of refraction and the spectroscopic parameters like scattering amplitudes $F^{(i)}$. The formula is valid in spherical symmetry. Treatment of the materials with defined symmetry can lead to the more complex expressions. For closer information I refer the reader to [57].

Now we see that the macroscopic and microscopic quantities can be linked to each other over the pure spectroscopic functions describing scattering events by means of quantum electrodynamics. It is also possible to link microscopic response to the reflectivity signal measured in the experiment. For ferromagnets with cubic symmetry elements of dielectric tensor are related to the sum and difference signal as follows [156]:

$$\varepsilon_{xx} \approx (I^+ + I^-)/\omega^2 \tag{4.29}$$

$$\varepsilon_{xy} \approx (I^+ - I^-)/\omega^2 \tag{4.30}$$

The elements of the dielectric tensor, including z components, vanish due to the reasons of symmetry. When compare 4.29 and 4.25, one can see that diagonal components of the permittivity or in other words dielectric tensor depend only on the scattering factor $F^{(0)}$, which describes pure charge scattering. If the magnetic contribution disappears, the index of refraction depends in turn only on $F^{(0)}$. From the section about magneto-optic we know that diagonal elements of the reflection matrix 4.13 depends on an unperturbed index of refraction. This means it depends only on $F^{(0)}$ and on the angle as well. According to this logic, the effect of $|\Delta_{sp}|^2$ disappears
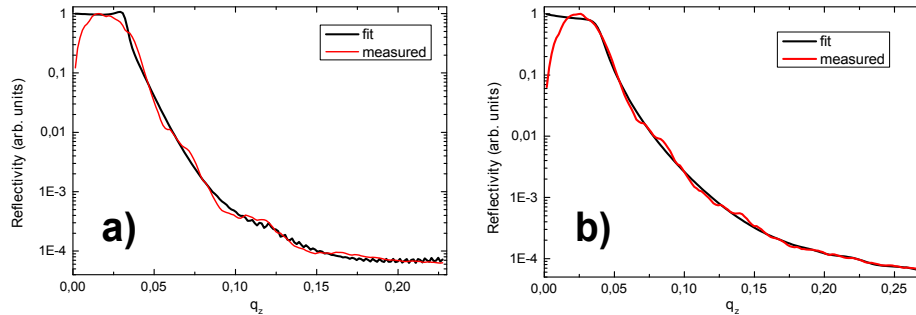
61

Figure 4.11: *Reflectivity curves and fits made with ReMagX a) for Manganese measured on L_3 edge b) for Cobalt measured on L_3 edge.*

in the sum signal. We can see that the sum signal in the range of angles with appropriate spectroscopic features and have a similar trend, especially between $7°$ and $8°$ degrees see figures 4.5 and 4.6. For resonant and non-resonant energies of photons, the sum signal is quite the same. Non-diagonal components of the dielectric function include magnetic scattering amplitude $F^{(1)}$.

4.2.4   Simulations of reflectivity with ReMagX software

Zak-matrix formalism [152, 153] developed for the simulation of reflectivity and transmission of the light in layered media with magnetic boundary allows the estimation of the parameters of interest, i.e. index of refraction with magnetic contribution, roughness of the surface, thickness of single layers and other. This formalism needs to define boundary and propagation 4×4 matrices originated from the common requirement of the classical description based on the Maxwell's equations. Similar to the general-matrix formalism mentioned in section 3.3, it allows one to describe reflection and propagation of the X-ray in a magnetic layered system.

We used software developed for reflectivity simulations named **ReMagX** by Sebastian Brück et al. [17]. This packet is based on the Zak-matrix formalism. Using reflectivity curves on Co_2MnGa we estimated the index of refraction in the energy domain of interest. This was L_3 edge for Manganese and Cobalt. First we can use it for the simple simulation of the reflectivity in case of one boundary between vacuum and the magnetic matter. We show it in section 4.2.3.

Additionally, we can evaluate the penetration depth of the X-ray into the sample and estimate which region of Co_2MnGa has been probed. We have already indicated the absorption profile of pump light in the sample. It has been done in section 3.3.2. The intensity of the X-ray decays comes deeper into the sample. One can suppose that initiated dynamics might be
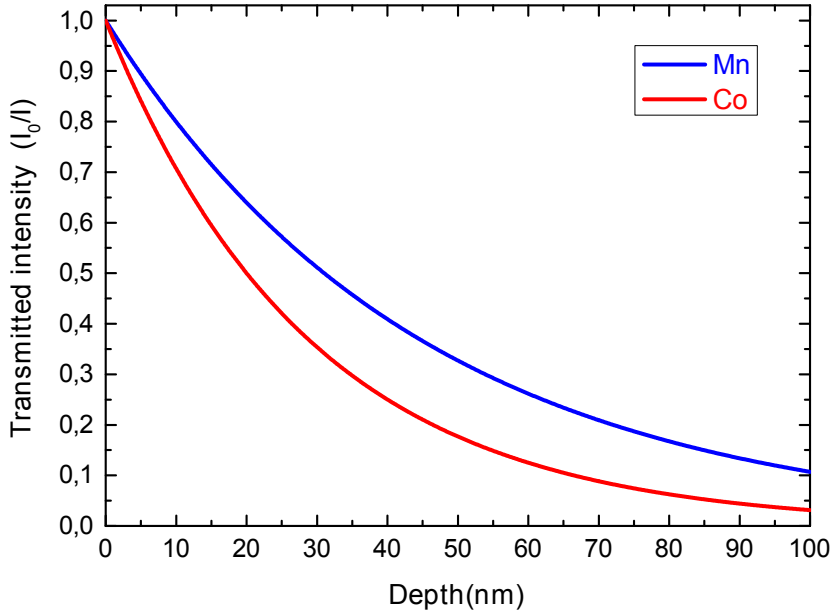
Figure 4.12: *Transmitted X-ray intensity.*

of a different order of amplitude, or in other words, the sample is excited inhomogeneously. Now we can evaluate how deep the sample can be probed using an optical constant for the X-ray energy. Also the photon energy for probing is different for Manganese and Cobalt L_3 edges. This can have the effect that the X-ray penetrates differently into the sample.

The reflectivity on the Co_2MnGa has been measured on the PM3 beam-line. In the figure 4.11, the measured reflectivity on the sample is presented for energies E_{Mn}=638.7 eV and E_{Co}=778.1 eV which correspond to the L_3 resonant edges of elements. As previously mentioned, we can extract the index of refraction from these simulations. In particular, we are interested in the imaginary part, namely β, in order to evaluate the penetration depth of the X-ray and δ. This can be used in equation 4.11, where $\mu = 2\kappa\beta$. Wavenumber κ can be expressed through the wavelength $\kappa = \lambda/2\pi$. The wavelength corresponds to the photon energy according to the form $E = hc/\lambda$. The imaginary part of refractive index extracted from simulations are $\beta_{Mn} = 4.6 \cdot 10^{-4}$ and $\beta_{Co} = 6.13 \cdot 10^{-4}$ for Manganese and Cobalt respectively. Delta coefficients are $\delta_{Mn} = 9.4 \cdot 10^{-4}$ and $\delta_{Co} = 1.6 \cdot 10^{-3}$.

Using the Beer-Lambert law, the transmission of the X-rays is evaluated, see figure 4.12. The X-ray penetrates completely into the sample. With a thickness of 100 nm almost 90% is absorbed by the sample.

4.3 Summary

From the absorption experiment performed by means of the TEY technique we evaluated magnetic moment of the Heusler-alloys. We can see that the spectral shape of the lines corresponds to the Manganese and Cobalt spectra observed in this type of Heusler alloys [143]. Especially, shoulder in the Cobalt spectra near the main L_3 peak promises good Heusler-quality. The relation between the magnetic moment of the Cobalt and Manganese 1:3 is in agreement with literature.

Using reflectivity measurements, we found out the experimental conditions for the pump-probe setup preferred for the detection of the magnetization changes. Similar to the XMCD applied in transmission geometry, the energy of the X-ray photons has to be fixed at the L_3 absorption edge by transmission metals. This corresponds to the transition from 2p core level to the 3d valence band. The incidence angle used for the measurement has to meet certain requirements. It should be away from the critical angle. Otherwise this value should lie outside of the region with dominant oscillation behavior especially in case of the Manganese. Angle dependent reflectivity measurements help to deduce it. Hence, we evaluated the region between $7°$ and $8°$ to be appropriate for measurements.

From the reflectivity measurements we found out that the difference between two signals measured for both opposite magnetization orientations is proportional to the magnetic response, while its sum sorresponds to the pure electronic response. These requirements are valid for the geometry known in the magneto-optic as longitudinal MOKE. In the case of Co_2MnGa, efficient angles for the measurements of the magnetization dynamics are in the range of $7°$ and $8°$. Between these values the spectra for both elements satisfy requirements listed above and the magnetic contribution is much higher than the pure electronic one.

Chapter 5

Wavelength dependent magnetization dynamics in Co$_2$MnGa

In this chapter, we will present the results of our experiments concerning the ultrafast magnetization dynamics of Co$_2$MnGa. We will first recapitulate idea behind these experiments. Co$_2$MnGa Heusler-alloy is a ferromagnetic material. Two ferromagnetic coupled sublattices are built by Cobalt and Manganese atoms. The magnetic moment corresponding to single elements is different in amplitude with relation $m_{Co}/m_{Mn} = 1/3$. Using the probe method described in previous chapters we are able to probe magnetization changes on Cobalt and Manganese atoms after the laser pulse irradiation. We want to use CMG (Co$_2$MnGa) as a prototype or a model system to perform our experiments and to comprehend, how behave the demagnetization vs. electronic response.

The electronic structure of this material possesses an energy gap in the minority band described in chapter 3. The majority gap has metallic like DOS 3.3. Pumping this system with ultra-short laser pulses, we initiate optical induced demagnetization. The main interest here is the role of the minority gap in demagnetization dynamics. Does it affect demagnetization time? In all microscopic theories represented in chapter 2.3 the initial step is excitation of electron by photons. The existence of the energy gap for minority electrons has to suppress electron transition. The absence of the final states should reduce the probability for electron spin-flip or transport probability. We propose to manipulate the demagnetization time by pumping our system with different wavelengths. The aim is to approach the gap-energy with pump photons and suppress completely electronic transitions in the minority gap (see. 5.1)

DOS (see fig. 3.3) for Cobalt and Manganese reveals a different energy gap for minority electrons. It explains also the different magnetic moments
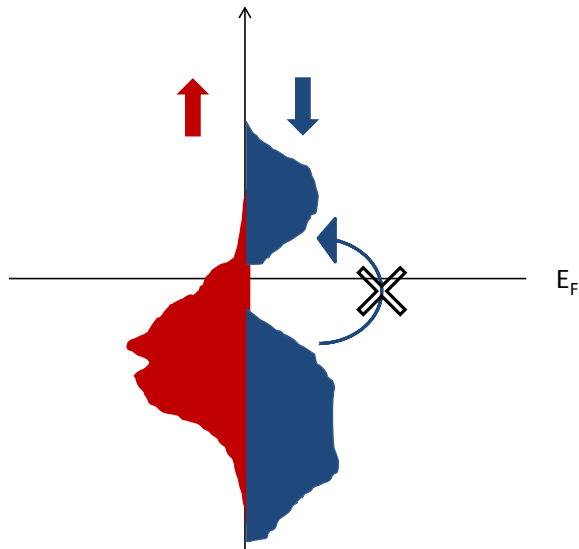
Figure 5.1: *Schematic representation of the transition suppression.*

of the sublattices. How different are demagnetization times for both elements? According to the report [52], the demagnetization of the sublattice with the higher magnetic moment occurs slower. This fact was proofed for ferromagnetic alloy GdFeCo. And how does it differ if we use two different wavelengths? Changing photon energy, especially when tuning it to a lesser value than that of the minority energy gap, we should theoretically change the probability of the electron's transition. Now, together with the commissioning of reflectivity XMCD, we should answer this question and justify a new technique, namely reflection XMCD for element resolved investigation of ultrafast magnetization.

In the next sections we will first explain the experimental setup, in particular, the optical pathway and realization of ultra-short X-ray pulses on BESSY II fs-beamline. Subsequently, results of the demagnetization dynamics will be presented and discussed.

5.1 Experimental setup

The time resolved magnetization dynamics has been measured by means of the pump-probe technique. The common principle here is that a laser pulse initiates transient changes of local features in the matter and subsequently, the second pulse, probe its properties. The probe method can be chosen according to the physic problem that has to be answered.

The pump-probe experiment has been performed for two pump wavelengths, namely for 400 nm and for 1240 nm . Their energy corresponds
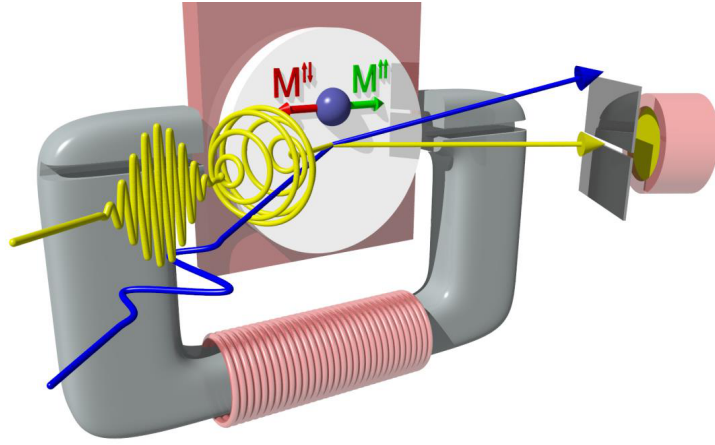
Figure 5.2: *Experiment setup. Blue solid curve: laser pulse with p - polarization. Yellow curve: X-ray pulse. Detector with horizontal (energy resolving exit) slit. Electromagnet with tunable magnetic field.*

respectively to $3\,\mathrm{eV}$ and $1\,\mathrm{eV}$. Demagnetization dynamic was probed with circular polarized X-ray in reflection geometry where the angle of incidence was between $7°$ and $8°$ to the surface. The energy of the X-rays photons has been set on the L_3 resonance for Cobalt and Manganese. Accordingly, the undulator's gap has been moved to the appropriate value. The incoming laser was mostly collinear with the X-ray beam but with small deviations in the direction of the propagation, in order to prevent direct irradiation of the APD after reflection from the sample surface (see fig. 5.2). The helicity of the X-ray remains unchanged while the generated external magnetic field was flipping, changing the magnetization direction of the sample. For more experimental details and visualization see in fig. 5.2. Our sample has an in-plane magnetization. Therefore, the magnetic moment lies in the incidence plane of the X-ray. A reflected signal was recorded with *Avalanche Photodiode* (APD) for following attitudes: 1) projection of the X-ray wave vector on the sample surface was parallel to the unit magnetization vector ($\hat{k} \uparrow\uparrow \hat{m}$). Let us define this recorded signal as I^+ and 2) projection of the X-ray wave vector on the sample surface was antiparallel to the unit magnetization vector ($\hat{k} \uparrow\downarrow \hat{m}$). Let us define this recorded signal as I^-. The time resolved changes of reflectivity were measured and analysed for both orientation of magnetization on Cobalt and Manganese L_3 edge. In the following sections the setup will be described closer.

500 MHz master clock for synchronization

Ti:Sa laser oscillator

Laser amplifier 3kH

780 nm

OPA

1240 nm

780 nm

Laser amplifier 6kH

U139 modulator

femto bump

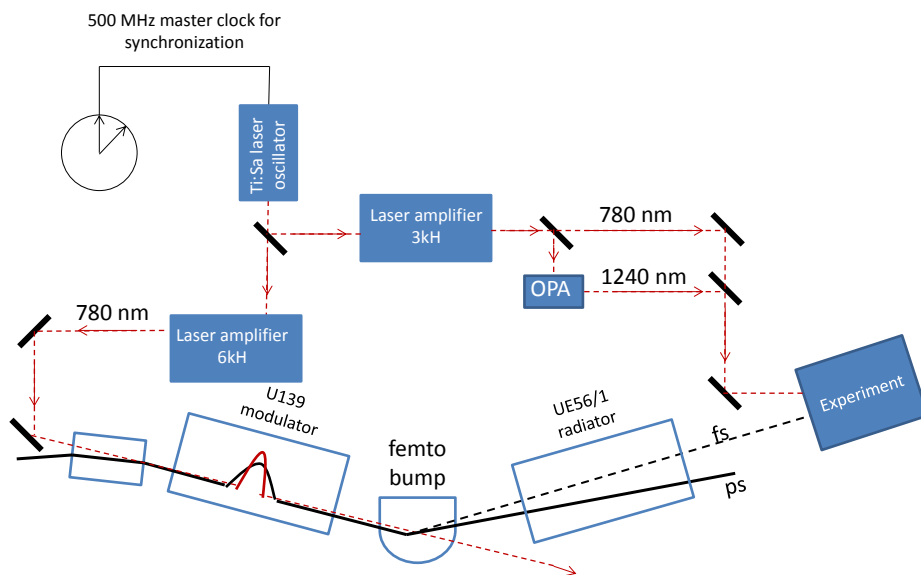UE56/1 radiator

fs

ps

Experiment

Figure 5.3: *Schematic representation of X-ray generation with femtosecond pulse duration.*

5.1.1 Pump-probe setup

As we discussed in chapter 4, to probe the magnetization, one requires a dichroic effect arising from different spin orientations in majority and minority bands. This can be realized with circular polarized X-ray in absorption or reflection geometry. To study ultrashort dynamics the duration of X-ray pulses should be comparable to the timescale of observable processes. Here we would like to discuss the pump-probe setup on BESSY II facility and briefly describe generation of elliptical X-ray pulses with 100 fs duration and setup for pump laser.

Generation of X-ray pulses with 100 fs duration

For the generation of X-ray pulses with sub-picosecond duration we used a method mostly known as 'slicing'. It was theoretically described and realized at the Advanced Light Source (ALS) in Berkley, USA [122, 123]. This technique has been applied at the BESSY II facility. An ordinary electron bunch in the storage ring is energetically modulated by a laser pulse of 40 fs duration. This happens in a planar undulator. Since the laser pulse is shorter than the electron bunch only a small part of the bunch is modulated. Subsequently, the 'sliced' part of the electrons and rest of the bunch arrive at the radiator, where the X-rays are emitted. In our case, for the realization of this scheme the U139 planar wiggler of 10 periods as 'modulator' and UE56 elliptical undulator of 30 periods as radiator are in operation. This last undulator of the APPLE II type can produce linear and elliptical polarized photons in the range $100\,\text{eV} - 1400\,\text{eV}$ and preserves the temporal characteristic of the X-ray pulse.

Energy modulated electrons excited by the slicing laser field reach a certain energy modulation. In order to provide good slicing conditions it has been established that a ratio between modulation energy and energy of the electrons in the storage ring has to be $\cong 1\%$. It demands the laser power to be around 10 mJ. To control the quality of modulation a special feature of the modulated electrons is used. The longitudinal bunch profile has a sub-picosecond dip and side lobes. Passing the undulator it emits a THz signal [62]. The intensity of this secondary radiation is detected in real time. Using this signal, we can optimize the spatial and temporal overlap between laser pulses and electron bunches from the operator pool.

Energy modulated electrons remain in the storage ring and passing the undulator, emit photons even after many turns. This parasitic radiation is known as 'halo background'. In contrast to sliced signal, the halo radiation has a picosecond pulse width. It decays and disappears a few milliseconds within the first slicing event. For the repetition rates above 1 kHz their presence becomes significant [120]. Using a special storage ring filling pattern with special timing, when the laser system initiates the slicing event, this

undesirable effect can be suppressed [63]. Three additional hybrid bunches with a time delay of $12\,\mathrm{ns}$ are created in the ring. Working in the so-called "sequence mode", the laser pulse jumps from one to another hybrid bunch, effectively reducing the repetition rate of the laser hitting a single electron bunch.

The electrons interacting with the laser field (energy modulated) have an energy different from the rest of the bunch. This property is used to separate them horizontally. For this purpose, a special bending magnet is mounted between modulator and radiator (see fig. 5.3). Because of their different energy, electrons are dispersed in the magnetic field differently from the ordinary trajectory. This affects the radiation axis of X-rays. Hence, the picosecond radiation is separated from the femtosecond one, which makes it possible to properly separate both beams by the optimization of the femto-bump's position.

In order to synchronize the time between the slicing laser and the pump laser a special synchronization scheme is used based on the ring master clock as trigger. A digitalized scheme with delay generators and logical cells makes it possible to synchronize the timing between sliced X-rays at $6\,\mathrm{kHz}$ and the pump signal at $3\,\mathrm{kHz}$. Particularly, in our experiments we used the $3\,\mathrm{kHz}$ pump laser and probe regime of $6\,\mathrm{kHz}$. Therefore, we could measure reflectivity when it was pumped and unpumped.

Energy settings for X-rays are defined by the undulator gap and the monochromator settings. The monochromator by fs-slicing experiments has to satisfy several conditions like time and energy resolution together with high photon transmission. We cannot achieve all these demands simultaneously but a compromise can be found. For our experiments we used the UE56/1-ZPM beamline. It consists of a single optical element: a 9-fold array of zone plates in the reflection mode. It provides transmission up to 21%. The current ZPM works in the energy range $380\,\mathrm{eV}$ to $1333\,\mathrm{eV}$. Standard energy resolution is $\lambda/\Delta\lambda = 500$. For Fe 2p excitation also a high resolution $\lambda/\Delta\lambda = 2000$ RZP is available. The details can be found in references [10, 145].

Pump laser setup and changing of wavelength

The laser system for sample pumping consists of Ti:Sa amplifier (Legend Elite Duo; COHERENT) is driven by an oscillator (Micra: COHERENT). The same oscillator is used to drive the amplifier for slicing generation. The amplifier emits pulses with $800\,\mathrm{nm}$ wavelength and pulse duration of around $50\,\mathrm{fs}$ as determined by autocorrelation. The laser repetition rate used for pumping was $3\,\mathrm{kHz}$, while the repetition rate of the slicing laser used to be $6\,\mathrm{kHz}$. An operation of the slicing laser with doubled frequency allows one to measure the response of the system in pumped and unpumped regime.

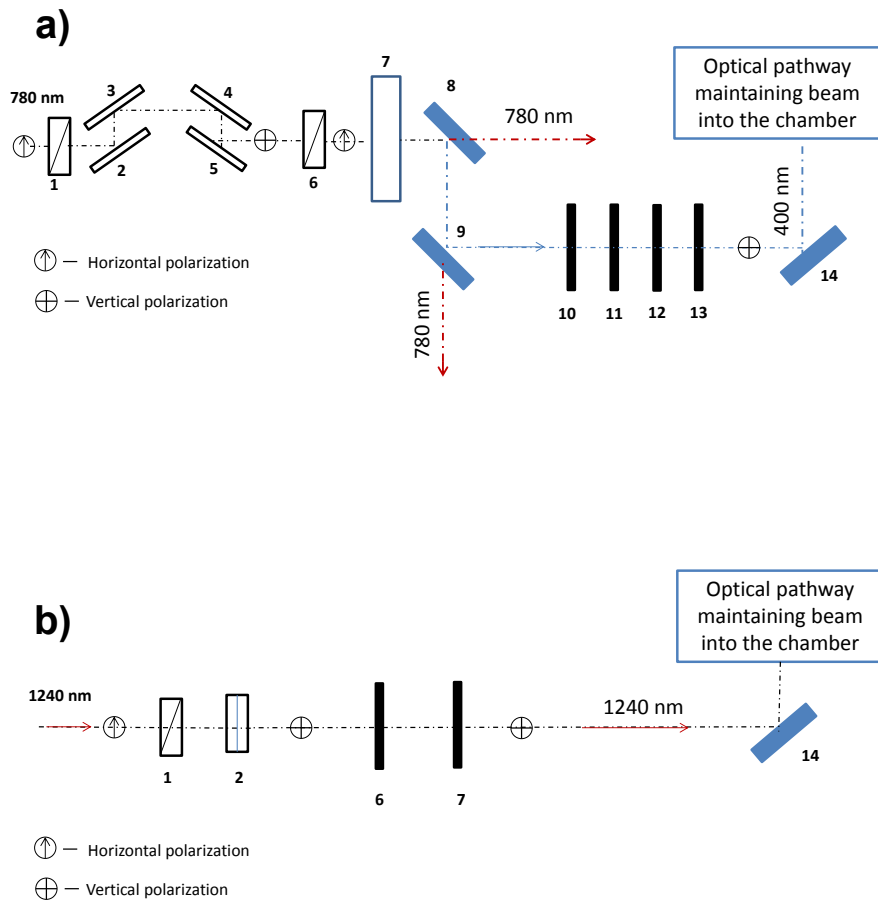For the generation of $400\,\mathrm{nm}$ wavelength corresponding to the $3\,\mathrm{eV}$ pho-

Figure 5.4: *A part of the optical pathway for power tuning and beam focusing optics of the pump laser. a) 400 nm(1,6) λ/2 plates (2 - 5) system of mirrors (7) BBO crystal (8-9) dichroic mirrors, made to reflect 400 nm. Fundamental wave of 800 nm comes through (10-13) system of plan-concave and plan-convex cylindrical mirrors for focusing of the beam (14) mirror. b)1240 nm (1) λ/2 plate (2) polarisator (6-7) spherical plan-concave and plan-convex CaF lenses.*

ton energy, Barium Borate (BBO) crystal was used to produce second harmonics from 780 nm fundamental. The optical pathway is depicted in the figure 5.4 together with the focusing scheme and the mechanism for power control of the pump laser. For the regulation of the laser power, a system of a $\lambda/2$ plate depicted as (1) in the figure 5.4 and mirrors (2-5) was used. The initial polarization of the incoming laser beam is linear parallel to the table surface. It passes the $\lambda/2$ plate so that the orientation of the polarization can be controlled. By the set of mirrors, the horizontal component of the polarization loses its strength while the vertical component preserves its intensity. This principle is based on the common properties of the electromagnetic field on the boundary of two surfaces. After several reflections, only the vertical component of the electric field is present. This type of intensity control preserves the temporal duration of the pulses while transmission elements like polarizers would induce a chirp, i.e. a wavelength dependent pulse elongation. Subsequently, the polarization is rotated by the $\lambda/2$ plate (6) to be parallel to the table and to be aligned to the active axis of the BBO crystal. After the BBO, fundamental and second harmonic frequencies have to be separated. To gain only second harmonic, a system of two dichroic mirrors (8-9) is applied. This reflects 400 nm and transmits 800 nm. After two times reflection the out coming beam is monochrome.

Lenses used for focusing the beam, are cylindrical convergent plano-convex and divergent plano-concave acting as Galilei telescopes. The set of cylindrical lenses allows for independent horizontal and vertical focusing. The first incidence occurs on the divergent lens. Subsequently, the convergent one focuses the beam. Using translation stages for the lenses the focus can be simply adjusted on the sample. For this reason, a phosphorus plate on the sample holder is used to visualize the X-rays together with the laser beam spot. A CCD camera delivers the picture on a monitor. The beam profile can be determined exactly by the pinholes mounted in the chamber. They are of a well-defined diameter $20\,\mu m$, $100\,\mu m$ or $500\,\mu m$. The laser power inside the chamber is measured by a Si-diode.

The generation of 1240 nm wavelength corresponding to 1 eV photon energy is realized with an Optical Parametrical Amplifier (OPA) (Coherent OPerA Solo). For the focus of this beam, a system of two spherical lenses was applied, fabricated from CaF material suitable for this wavelength range. Optical components (6-13) used for 400 nm beam-path are replaced. A system of cylindrical lenses is changed to the spherical divergent and convergent lenses (6-7 in fig. 5.4). Components (2-5) responsible for the flux-control are replaced as well. The beam impinges directly on the mirror 14. Therefore, a change between the two different pump wavelengths is accompanied by a change of the focusing optics and mirrors.

In order to perform pump-probe measurements, time and spatial overlap has to be matched. The spatial overlap is found using a phosphor plate with a $100\,\mu m$ pinhole. Laser and X-ray spots are located on it to see roughly

the position of both beams. A CCD camera with focus on the plate is applied to see the picture on the monitor. For a fine adjustment of the spatial overlap in a second step, the in-coupling mirror with μm motors for horizontal and vertical translation of the laser spot on the sample surface is used to maximize of pump-induced change in the reflectivity data by fixed time delay. The upgrade of the femtoslicing beam line with a piezo-driven in-coupling mirror simplifies the determination of the overlap largely. A coarse temporal overlap is done by observing Avalanche Photodiode (APD) signals of the direct beams of laser and X-rays on an oscilloscope. The fine-tuning is possible only by the observation of the signal's change by during the experiment.

5.2 Experimental results

In this section, we will describe the pump-probe results. For the magnetic response we use the difference between both recorded signals I^+ and I^-. As described in chapter 4 we use the difference signal as a measure for the magnetic response. It describes changes in reflectivity for parallel and antiparallel magnetization orientations after laser irradiation. The difference is defined as $I_{Diff} = I^+ - I^-$. We measured pump induced reflectivity for both wavelengths λ_1=400 nm and λ_2 =1240 nm with corresponding photon energy E_1=3 eV and E_2=1 eV respectively. We probed with X-rays tuned to the resonance of the L_3 absorption edges for Cobalt and Manganese in reflection geometry. Pump conditions as fluence has been already evaluated in section 3.3.2. In case of 400 nm wavelength pumping, the fluence was 1.9 mJ/cm^2 and for 1240 nm 2.1 mJ/cm^2. In figures 5.5, 5.6, 5.7 and 5.8 results for magnetic and electronic signals for both elements are depicted. Measured curves were fitted with a function $F(g*f)$. This is a convolution of the Gaussian function g and function f. Function g describes the temporal resolution, mainly given by the X-ray pulse duration. f describes the real response of the system. The latter one is supposed to have the following form

$$f = A_0 - B \cdot (1 - exp[-(t - t_0)/\tau]) \qquad (5.1)$$

Overall, four parameters have been varied during the fit iteration: the amplitude of decay B, the time constant τ, the time zero t_0 and the initial amplitude A_0 of the measured signal. Carrying out the fit procedure it is possible to determine decay time constants for magnetic response and pure charge response. In the case of the pump wavelength λ_1=400 nm, we have evaluated following time constants for the magnetic signal: τ_{Co}=135 fs $\pm$ 50 fs and τ_{Mn}=120 fs $\pm$ 50 fs. Changing the pump wavelength to $\lambda_1 = 1240 \, nm$ we obtain another result. Time constants here are also derived from the fit function: τ_{Co}=257 fs $\pm$ 30 fs and τ_{Mn}=273 fs $\pm$ 30 fs. The electronic re-
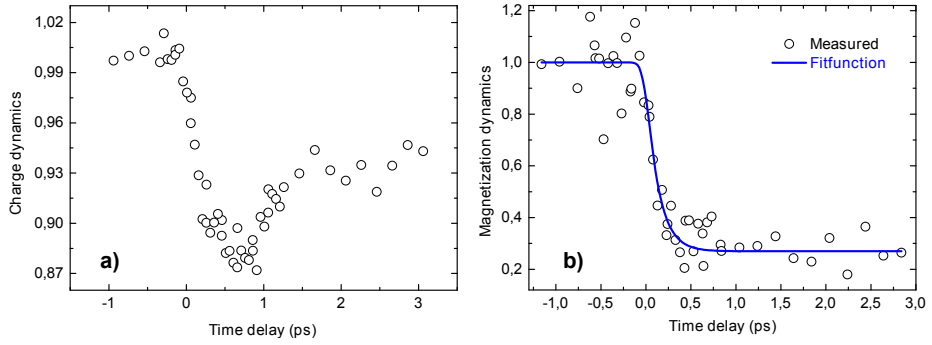
Figure 5.5: *(a) charge and (b) magnetic dynamics for Cobalt after 3 eV photon energy pumping.*
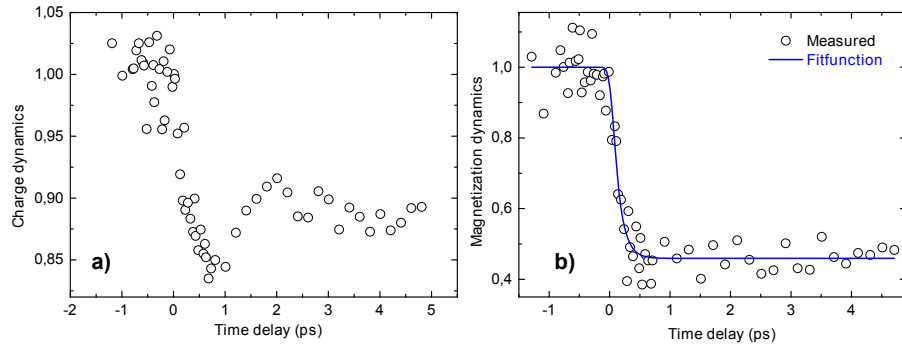

Figure 5.6: *(a) charge and (b) magnetic dynamics for Manganese after 3 eV photon energy pumping.*

sponse has also been analyzed for both elements. We recapitulate these time constants in table 5.2.

	400 nm		1240 nm	
Element	electronic	magnetic	electronic	magnetic
Cobalt	100 fs±30 fs	135 fs±50 fs	100 fs±30 fs	257 fs±30 fs
Manganese	98 fs±30 fs	120 fs±50 fs	100 fs±30 fs	273 fs±30 fs

Table 5.1: *Time constants for electronic and magnetic signall.*

From the demagnetization curves and results for the time constants, we can summarize our observation as follows:

1. The resonant X-ray reflectivity is a measure for fs-probe of magnetization.

2. The resonant X-ray reflectivity is a measure for fs-charge response.
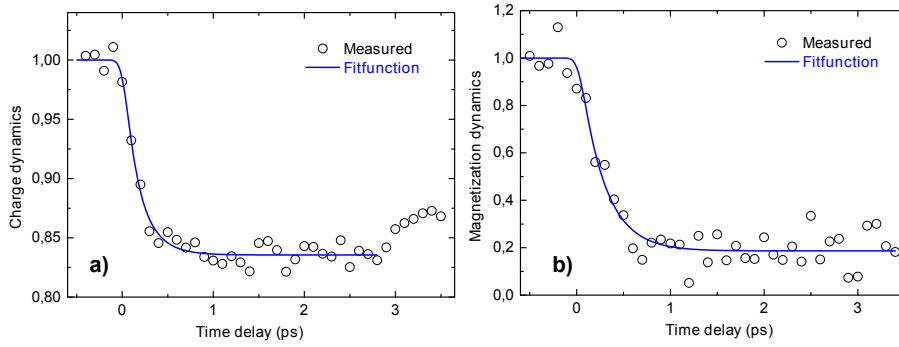
74

Figure 5.7: *(a) charge and (b) magnetic dynamics for Cobalt after 1 eV photon energy pumping.*
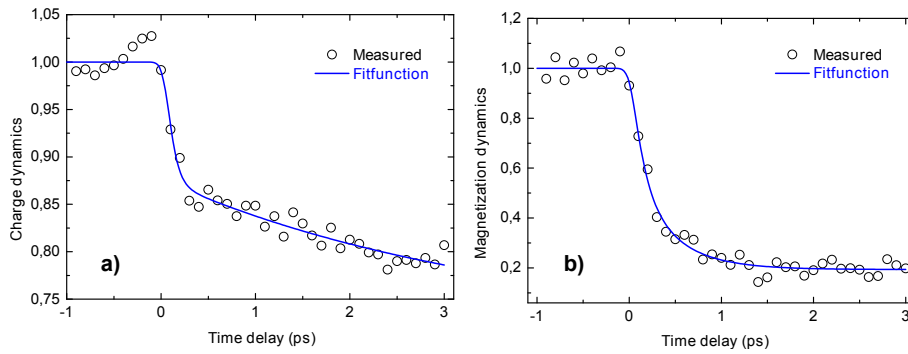
Figure 5.8: *(a) charge and (b) magnetic dynamics for Cobalt after 1 eV photon energy pumping.*

3. The charge response appears very fast in all cases and determines the experimental time resolution.

4. The magnetic response is slower than the time resolution in all cases.

5. Magnetic and electronic response times are minimally element dependent and very important in contrast to other models.

6. The magnetic response is strongly wavelength dependent.

5.3 Understanding of ultrafast demagnetization in Co$_2$MnGa

5.3.1 Laser excitation and relaxation of electrons

Independently on the theoretical model involved in the explanation of ultrafast demagnetization, the first step is an excitation of the system by the laser pulse. We pumped our system with wavelengths of 400 nm and 1240 nm. In this regime, photons interact mostly with electrons. Hence, the sub-system of electrons is excited first. A laser pulse excites electrons out of equilibrium. Therefore, electrons are not in the Fermi distribution. Typically, electrons achieve this highly non-equilibrium state within a few fs. With our time resolution of 100 fs or less, we cannot determine charge dynamics with high resolution. Hence, we are restricted in the relaxation time determination of electrons dynamics. A relaxation to the ground state by interaction with the environment occurs in the next step. It can be electron-electron, electron-phonon interactions, and others.

Available decay channels affect the lifetime of excited electrons. There are different models developed in the last years describing electron relaxation and energy dissipation in metals [95]. In the electron gas model, decay times scale with

$$\tau_{ee} \sim \frac{1}{(E_i - E_F)^2} \tag{5.2}$$

This result is valid for decays affected by electron-electron interaction. In different models, this relation can be multiplied with pre-factors characterizing a metal system [115, 116]. The decay time depends on the photon energy interacting with the electron system. The consequence is the following. We excited our system with two different photon energies. Because of equation 5.2, we should observe faster electron dynamics for higher pump photon energy. Nevertheless, we are restricted in our experimental resolution at around 100 fs and cannot observe times faster than this limitation. However, this model does not take the band structure and spin dependent lifetime into account. Therefore, the effect of the band-gap in the minority states remains out of consideration. Nevertheless, pump-energy dependent inelastic decay of electrons can explain our observation of pure electron dynamics and this is faster than the probe pulse-duration for both pump wavelengths.

We find that demagnetization goes after the electron-dynamics and it is in agreement with reports published so far. Spin-dynamics are retarded compared to electrons. The fact that we measure two different times for charge and magnetic signals (see tab. 5.2) is proof of the proposed probe method of charge and spin dynamics. According to the absorption profile (see fig. 3.5) of the laser pulse for 400 nm and 1240 nm and X-ray transmission profile (see fig. 4.12) we can make the following conclusions:

i The effective penetration and, therefore, excitation profile for one laser pulse is around 20 nm. For 1 eV photon energy this depth is deeper and reaches 30 nm.

ii At 20 nm – 30 nm, X-ray transmission reaches 30% or 60% depending if we measure on the Cobalt or Manganese L_3 edge. It means that we are able to probe deeper regions than the laser pulse is able to penetrate. This has a consequence for the discussion of the model based on the superdiffusive spin transport (see below).

5.3.2 Table-top pump-probe experiment

In order to check the pump-pulse duration and to figure out if the electronic response for 1240 nm is real fast, we build up a table-top pump-probe experiment using Ti:Sa amplifier (Legend Elite Duo; COHERENT) driven by an oscillator (Micra: Coherent) (see previous sections). The experimental setup is depicted in the figure 5.9. Using a Lock-In amplifier, we could measure the reflected signal as a function of time-delay in the pump-pulse. In the absence of the dispersion optic, the pulse duration is around 60 fs for pump and probe signal. We used 800 nm wavelength for probing and 1240 nm wavelength for pumping. Experiments were performed for pump signal in p-geometry (polarisation in the incidence plane). This corresponds to the geometry used in slicing experiment. In the figure 5.10 one can see results. The rapid decay follows first after excitation and response arives its minimum. Afterwards the relaxation begins, which takes a long time. This picture is in agreement with other optical pump-probe experiments [13, 68].

Fitting of the observed data was performed with a function 5.1 used for curves from the slicing experiment. We fitted fast decay and figured out that the response time corresponds to the resolution of the experiment. It means, the Full Width of a Half Maximum (FWHM) of the probe signal restricts the fastest time which can be measured. In our case it is of ∼60 fs. Knowing that the electronic response in metallic system is of the order of some few femtoseconds this result is reasonable. This result demonstrates additionally that the pump pulse is very short. Otherwise we would observe longer decay times in the slicing experiment.

5.3.3 Superdiffusive spin transport

The idea behind the superdiffusive spin transport was already discussed in chapter 2. States with majority and minority electrons have different lifetimes after laser excitation. Hence, the majority electrons with shorter lifetimes drift to the non-excited region. Locally an area with a lack of majority spins arises. This leads to the loss of magnetization. It is well known that the drift-range is around 1 nm. In our experiment, we probe a depth
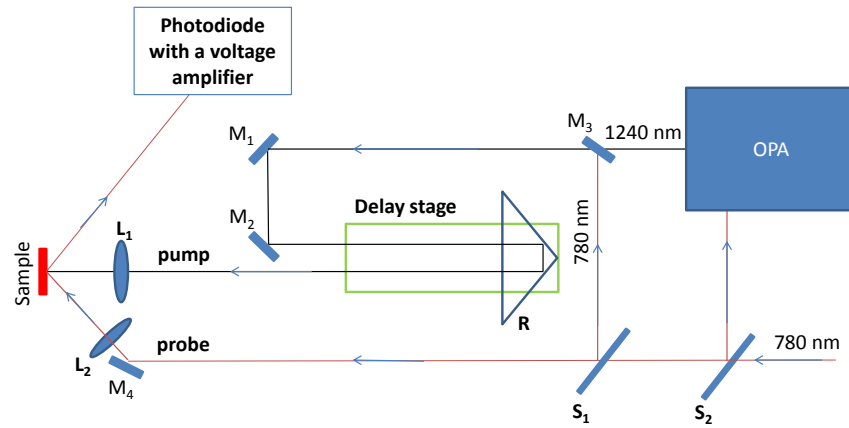
Figure 5.9: *Scheme of the optical table-top pump-probe experiment. Components used in this experiment: S - optical splitters, M - mirrors, L - lenthes, R - retroreflector. With the system of splitters we could simply change from 780 nm pump wavelength to 1240 nm wavelength. This means, that splitters could be used optionally either S_1 or S_2. OPA was used to produce 1240 nm wavelength.*
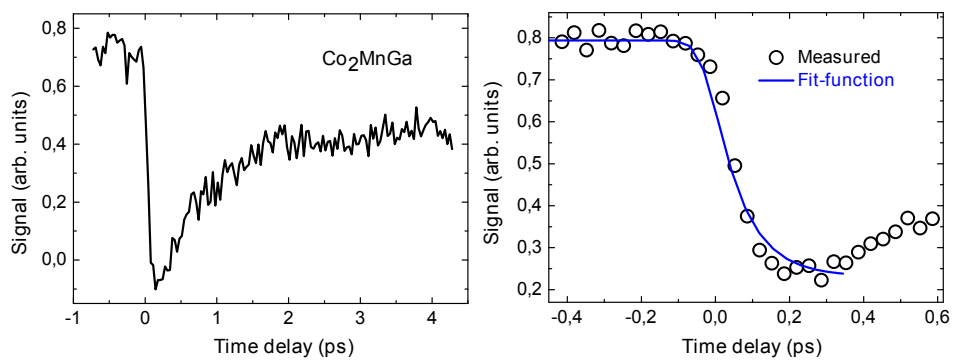

Figure 5.10: *Pump induced reflectivity as function of delay time to the pump pulse. Left: long range scan. Right: short range scan. Pumped with 1240 nm wavelength.*

larger than the excitation can penetrate. With a laser pulse, we generate a lack of majority electrons in the first 20 nm. All these electrons should be accumulated within the next 20 nm. We know that this region is probed by an X-ray. Due to the interference of propagated X-ray photons with oppositely magnetized layers, we should not measure any significant demagnetization. We observed demagnetization of 80% - 60%. This means that the demagnetization occurs homogeneously on the whole excitation region. Non-excited layers remain in the initial magnetic state. Majority electrons moving to the next layer should produce an abundance of majority electrons within in this layer. Hence, there should arise oppositely magnetized layers. In this case, the measured demagnetization should be smaller. The observation of 80% demagnetization cannot confirm this assumption. On the other hand, superdiffusive spin transport could be a good candidate for the explanation of demagnetization. This model preserves the total magnetic moment. The decrease of local magnetization arises due to the transport into the neighboring region. Hence, integration of the magnetization over the whole body volume remains constant:

$$\int \vec{\mathbf{M}} \mathrm{d}V = const \tag{5.3}$$

MOKE measurements in the visible range [11, 24] allow the interpretation of the demagnetization based on superdiffusive spin transport. This is possible because the penetration depth of the probe signal is of the same order as the penetration of the pump-pulse. Furthermore, these experiments have been carried out on thin films. Therefore, the probe laser scans a restricted area with a lack of majority electrons. With the X-rays, we probe many more atomic layers not only near the surface. The final reflected signal is averaged over all elementary reflections on the sublayers. Therefore, we cannot explain our observations based on a spin dependent transport of electrons only.

5.3.4 DOS and ultrafast demagnetization in half-metals

Superdiffusive spin transport cannot be involved into explanation of the ultrafast demagnetization in Co_2MnGa. The next candidate would be spin-flip caused by scattering events. In the theory of electron relaxation, scattering effects offer additional channels for energy dissipation. In ferromagnetic materials this process can initiate a spin-flip. In a previous section we saw that the lifetime of excited electrons in an electron gas model is proportional to $\sim (E_i - E_F)^{-2}$ [95]. This relation delivers a simple understanding of the relaxation time of electrons dependent on the excitation energy. We try to figure out if the DOS could predict or explain in any way the demagnetization times observed in the experiment.

Due to the presence of the energy gap in minority bands, we should consider the following scenario. With tuning the photon energy of the pump
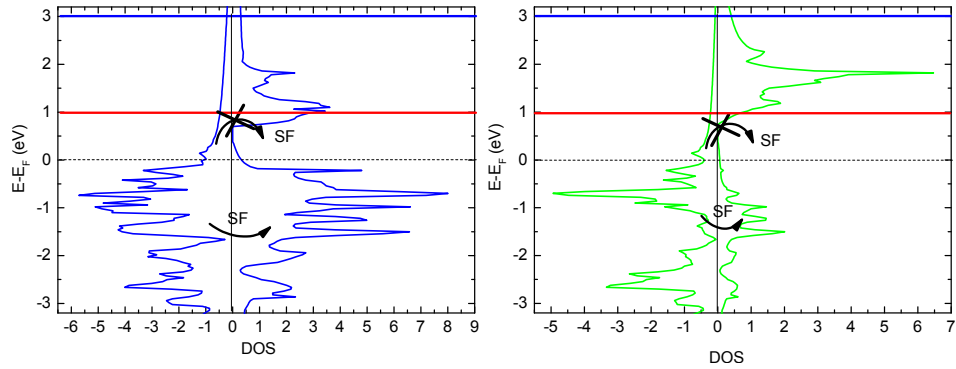
Figure 5.11: *DOS for Co (blue curve left) and Mn (green curve right). Possible spin-flip events. Solid red line describes upper level of electrons excitation available for 1 eV photon energy. Solid blue line for 3 eV.*

laser we excite electrons. In one electron picture using dipole approximation an electron makes transition absorbing a photon to the next energy level. This energy change is equal to the energy of the absorbed photon. In figure 5.11 the available upper energy level for 1 eV and 3 eV photon energy are depicted. Pumping the sample with higher photon energies we open an access to higher energy states in minority bends. Hence, we increase the possibility for electron transitions. In the energy range between 1 eV and 3 eV in the DOS picture (see fig. 5.11) one could expect even spin-flips. There are available states in this energy domain. Decreasing the photon energy we reduce phase-space for spin flips. In the range between 0 eV and 1 eV available states in the minority bans are appreciably reduced. It affects the demagnetization time. Something we clearly observed.

Spin-flip events are possible even below the Fermi level according to the reports published so far [130, 131]. Taking this argument for the possible spin-flip channel into account, we can explain demagnetization times comparable to the transition metals. One question, however, remains open. Why the demagnetization of Co and Mn sublattices is of the same time order, despite the different between the magnetic moments of these elements? According to the publication of Radu et al. [52] we should expect the demagnetization time proportional to the magnetic moment of the element.

It becomes quite obvious, that the DOS of the structure cannot deliver complete information about the entire proceeding of the dynamic processes in the matter. Looking at the figure 5.11 we realize that the minority band-gap for Mn is larger than for Co. Nevertheless, Manganese having magnetic moment greater than Cobalt demagnetizes just as fast. We should consider the Elliot-Yafet theory of spin-flips closer, in order to figure out which parameters affect the spin-flip probability.

5.3.5 Elliot-Yafet spin-flip processes in ultrafast demagnetization

In this section we would consider microscopic mechanism of the spin-flip process. In Elliot-Yafet model an electron flip their spin die to the scattering on the phonon. Hence, there is a certain probability to find an electron in one of the spin state after the scattering event. In periodic potential wave function of one electron can be written in the form $\Psi_{n\mathbf{k}} = u_{n\mathbf{k}} exp(-i\mathbf{kr})$. This expression does not include spin orientation of the electron. Due to the spin-orbit coupling an electronic state can be considered as a mixture of 'up' and 'down' spin states. Therefore, the form of the wave function is [54, 129]

$$\Psi_{\mathbf{k}}^{\uparrow} = [a_{\mathbf{k}}(\mathbf{r})| \uparrow\rangle + b_{\mathbf{k}}(\mathbf{r})| \downarrow\rangle]e^{i\mathbf{kr}}. \tag{5.4}$$

Electron transitions in dipole approximation occur under conservation of the spin orientation. The spin mixture due to the spin-orbit interaction provides an additional spin channel. Hence, in the second order perturbation theory it is possible to consider scattering accompanied by the flip of the spin [14]. This result is comparable to the effect of the conservation of the band vector $\mathbf{k}$ in the first order dipole transition of the electron in the solid. In the second order transition can occur from $|\mathbf{k}\rangle \rightarrow |\mathbf{k}'\rangle$ [107].

One of the important parameters in the Elliot-Yafet theory is the spin-mixing parameter

$$b^2 = min[p_{\uparrow}, p_{\downarrow}] \tag{5.5}$$

with $p_{\uparrow}$ and $p_{\downarrow}$ probabilities to find electrons in spin-up and spin-down states. This is a functional and can have values between 0 (pure spin states) and 0.5 (completely mixed states) [54]. The final form of the Elliot-Yafet equation for the spin-relaxation is [14, 54]

$$\frac{1}{T_1} = p\frac{b^2}{\tau} \tag{5.6}$$

with T_1 recovery time of the magnetic state to their equilibrium, τ Drude relaxation time, p material specific parameter. Let us discuss this equation. First we see that the relaxation time of the magnetic system is proportional τ. We have already discussed this parameter in the section 5.3.1. Electron relaxations occur faster relative to the rise in excitation energy. Hence, the proportionality of the magnetic relaxation time to the electronic relaxation time, could be a consequence of this fact. Unfortunately, we cannot resolve electron dynamics in our experiments since we are restricted in the pulse duration of our probe signal.

Secondly, we can see that the relaxation time of the magnetic system depends reciprocally on the square of the spin-mixing parameter b^2. This parameter is different for wave functions with different dispersion bands and energy indices $(n, \mathbf{k})$. Only in some regions of the Brillouin-zone this

parameter can reach high values. These are so called "hot-spots". Demagnetization is faster dependent on how high is the b functional. This is a question on theory to calculate b values over various k branches and figure out the channel with the highest spin-mixing states.

We return to the question of the demagnetization rate of Manganese vs. Cobalt. Using the Elliot-Yafet spin-flip mechanism as microscopic mechanism for the ultrafast demagnetization, we should suppose that the spin-orbit coupling for Manganese is stronger than for the Cobalt. This leads to the higher spin-mixing parameter b for Manganese and consequently to the higher spin-flip probability. Which could explain why Manganese demagnetize as fast as Cobalt sublattice, while the magnetic moment of the Manganese relates to the Cobalt magnetic moment as $1:3$.

5.4 Summary

We performed pump-probe experiments on the slicing beam line using two pump regimes and X-rays as probe signal. We found out that the electronic response is extremely fast, so that the decay time lies outside of our resolution ability. We additionally confirmed this finding with a table-top experiment. In this case our probe signal in visible range was around $60\,\mathrm{fs}$ duration. Demagnetization is evidently independent of the element and is of mostly the same order for Manganese and Cobalt. A clear wavelength dependence for the demagnetization is evident. For higher photon energies the demagnetization is faster. The experimental setup and the properts of the sample allow one to exclude a superdiffusive spin transport and the direct photon interaction as microscoptic mechanisms explaining the ultrafast demagnetization in Co_2MnGa. A possible mechanism remaining for the understanding of the ultrafast demagnetization processes are spin-flips, due to the scattering events. Nevertheless, some parameters, such as element-specific spin-mixing parametrs for Mn and Co, are unknown. The knowledge of this constant would cover the lack of the coefficients in the equation 5.6 and additionally provide a basis for understanding of similar demagnetization times for Co and Mn.

Chapter 6

Conclusion and outlook

In this work we investigated ultrafast demagnetization in ferromagnetic full Heusler-alloys with the chemical formula Co_2MnGa. For this aim we proposed to use a new probe technique for magnetization, namely resonant X-ray reflectivity, based on the magnetic dichroic effect on L_3 absorption edges in transition metals. With preliminary static experiments we figured out which incident angle would match experimental requirements, in order to deliver adequate information about the magnetization. Additionally, we found out that the difference between two signals recorded for both magnetization directions describes a magnetic response of the system, while the sum signal describes approximately pure electrons dynamics.

In the second step we performed pump-probe experiments investigating the effect of the wave length on the demagnetization time in the half-metallic system. Decreasing the energy of the photons and approaching the energy value of the gap in minority bands, we slow down the demagnetization dynamics. Trends in sum and difference signals can be seen in the figure 6.1.

6.1 XMCD in reflection as a probe method for demagnetization dynamics

A series of static reflectivity measurement revealed exact parameters used for probe of the demagnetization in Co_2MnGa. Free choice of these parameters is restricted. It can be energy and the angle at fixed X-ray polarization. We showed that it is possible to disentangle the charge and magnetic dynamics. For this purpose the reflected signal has to be treated on the certain way. We proposed and verified that sum-signal $\sum I = I^+ + I^-$ normalized at one at its maximum indicates charge contribution to the reflection and the difference signal $\Delta I = I^+ - I^-$ normalized to the one indicates magnetic contribution with good approximation. These relations are valid at certain values of the angle and the energy. Energy has to be adjusted to the L_3 resonance in case
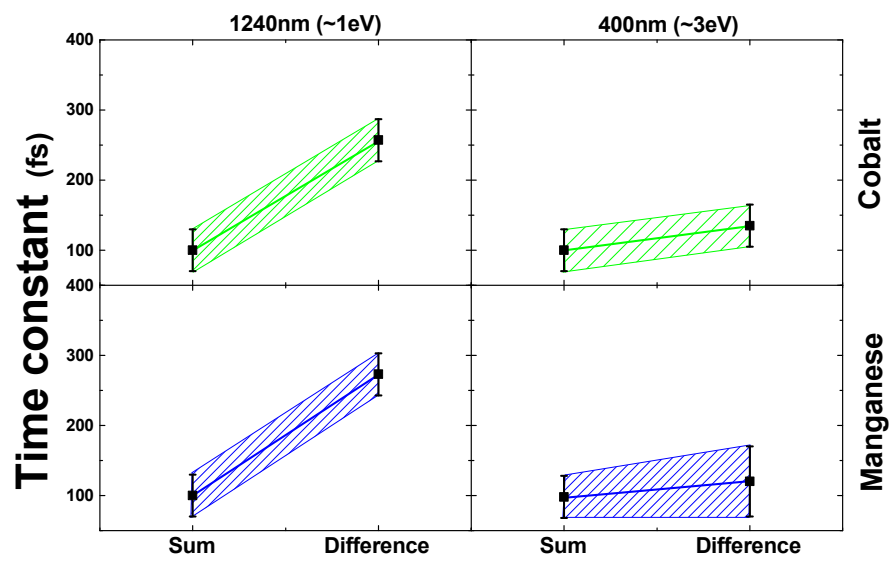
Figure 6.1: *Time constant for the sum and difference signals dependent on the element and the pump wave length.*

of transition metals. In our system these are Cobalt and Manganese. For this energy value the magnetic dichroic effect is at its maximum. Subsequently, the incidence angle has to match appropriate conditions. It should be away from the critical angle and, simultaneously, away from strong interference effects. These last occur for larger angles. In particular, this effect is stronger for Manganese.

Using theory we verified, those sum- and difference signals play the role of indicators for charge and magnetic contribution to the reflectivity. In a magneto-optical approach we succeeded in showing that the sum-signal depends only on Fresnel's coefficient and the magneto-optical constant is negligible. We compared calculations with measurements 4.10, these are in good agreement. In the case of the difference-signal, we considered the theory of the resonant scattering and reflectivity and found a link between non-diagonal elements in the permittivity ε_{xy} and the spectroscopic parameters $F^{(2)}$. The last is responsible for the magnetic dichroic effect according to the theory of the resonant magnetic scattering. This permittivity, in turn, is proportional to the difference-signal. It allows us to associate the difference-signal with magnetic response.

We have to mention that our system isa quite simple layer system. It has a capping layer of Aluminum with $3\,\mathrm{nm}$ thickness, Co_2MnGa of $100\,\mathrm{nm}$ and the substrate. Hence, it is out of our scope to make profound conclusions with respect to multilayer structures. Interference effects of high complicity might occur and affect the signal in an unsuspected way. Therefore, we want to stress that our method works with simple single- or bi-layer systems.

6.2 Effect of the pump wavelength on the demagnetization in Co_2MnGa

Our experiments reveal that we are able to slowdown the demagnetization in half-metallic Heusler structures tuning the energy of photons to the values comparable to the minority band-gap. When trying to explain this finding, we excluded superdiffusive spin transport as a possible candidate for the ultrafast demagnetization. The analysis of the X-ray penetration (see chapter 4 fig. 4.12) into the material and the laser excitation profile (see chapter 3 fig. 3.4) substantiate this assumption. One possible microscopic model explaining demagnetization would be spin-flip processes by electron-photon scattering events. In this model we can understand how the gap can affect the demagnetization time. Additionally, we have to suppose that spin-mixing states for the Manganese should have higher magnitude than for Cobalt. On this basis of this assumption we can explain why the demagnetization rate of Manganese is higher than for Cobalt.

6.3 Outlook

X-ray static characterization

In chapter 4 we mentioned how the index of refraction and spectroscopic parameters $F^{(i)}$ are linked to each other by means of the permittivity. In this approach the simplest spherical symmetry was used. As we know Co_2MnGa has cubic symmetry (O_h) which makes the relation between dielectric permittivity and $F^{(i)}$ more complex [57]. Nevertheless, it would be possible to disentangle all five spectroscopic contributions in case of cubic symmetry. In the absence of the analyzer for the reflected X-ray photons one needs to perform four independent reflectivity measurements with respect to the polarization of the incident light. This would be normal to the incidence plane polarization $\hat{\sigma}$, parallel to the incidence plane polarization $\hat{\pi}$ and their extensions linear polarization $\hat{\sigma} + \hat{\pi}$ and circular polarization $\hat{\sigma} + i\hat{\pi}$. Modern synchrotron facilities make it possible to define polarization of the X-ray. Fixed polarization reduces the unknown amount of parameters in the differential cross-section and therefore allows an estimating contribution of the scattering amplitudes into the measured intensity. Without the polarization of the outgoing light it might be complicated to evaluate the scattering tensor. Nevertheless, for four fixed polarization states this challenge is simplified. From this point the magnetic and charge components can be disentangled more precisely, as in the case of the measurement with single circular polarization.

These kinds of measurements would be of great importance. We estimated the pump conditions only on hand of experiments with circular polarized light, thus quantitative experiments. More detailed experiments would open an access to the qualitative analysis. As such it would be possible to answer the question of which hybrid states are really involved in the charge and magnetic related scattering and thereby enable a more detailed analysis of the pump-probe experiments.

Additionally it would be of interest to compare spectra for Heusler-alloy from the same family of Co_2MnZ materials. As we already described in chapter 3 with Z-elements the magnetization of the sample can be varied. This variation occurs through the yield of the valence electrons of Z-elements. It would change the magnetization of the sample and contribute differently to the reflectivity amplitude. The symmetry has to be conserved due to the same $2L_1$ structure.

Further development of the pump-probe experiment

To completely suppress electronic transitions in minority bands we have to apply photon energy less than $0.5\,eV$. This value corresponds to the band gap in minority bands. We can see in that for $0.5\,eV$ the minority transition's

density approaches zero. Technically it was not feasible to do so, therefore we applied only photons with the energy of $1\,\mathrm{eV}$. In the next step it would be of interest to apply a laser pulse with energy low as $0.5\,\mathrm{eV}$ and even less. Primary electronic excitation plays crucial role in the whole dynamic processes, pure electronic and magnetic. As can be seen in the case of the two pump wavelength. Reducing the photon energy leads to the slowdown of the demagnetization. Whole suppression of the minority electron transitions has to affect demagnetization time dramatically. This would deliver an answer to the question if the microscopic spin-flip processes based on the Elliot-Yafet model only govern the demagnetization dynamics.

Acknowledgements

I would like to thank many people for being supportive of my work during my time as PhD student at BESSY II. I am very grateful for discussions and helpful advices. In particular I would like mention persons...

...Prof. Alexander Föhlisch for providing me a PhD position and agreeing to be my supervisor.

... Torsten Kachel, Ilie Radu, Loic LeGuyader, Nico Pontius, Karsten Holdack for sharing their expert knowledge about measurements at femtoslicing, helpful discussions and advice regarding time-resolved experiments, electron storage ring facilities, ultrafast magnetism and others.

... Rolf Mitzner for teaching me operate laser and OPA and supporting my table-top experiments

... Prof. Dr. Hans-Joachim Elmers Alexander Kronenberg for collaboration in this Project and sample's preparation.

...Prof. Iosif Galanakis for providing us numerical calculations of sample's DOS.

...Dr. Karsten Hinrichs from Leibniz-Institut für Analytische Wissenschaften – ISAS – e.V. for providing me with the possibility to work with an ellipsometer and Timur Shaykhutdinov for supporting me in these measurements.

Bibliography

[1] R. Abrudan et al. "ALICE—An advanced reflectometer for static and dynamic experiments in magnetism at synchrotron radiation facilities". In: *Review of Scientific Instruments* 86.6, 063902 (2015).

[2] M. Aeschlimann et al. "Ultrafast thermomagnetic writing processes in rare-earth transition metal thin films". In: *Journal of Applied Physics* 67.9 (1990).

[3] M. Aeschlimann et al. "High-speed magnetization reversal near the compensation temperature of amorphous GdTbFe". In: *Applied Physics Letters* 59.17 (1991).

[4] M. Aeschlimann et al. "Ultrafast Spin-Dependent Electron Dynamics in fcc Co". In: *Phys. Rev. Lett.* 79 (25 1997).

[5] T. Ambrose, J. J. Krebs, and G. A. Prinz. "Magnetic properties of single crystal Co2MnGe Heusler alloy films". In: *Journal of Applied Physics* 87.9 (2000).

[6] U. Atxitia et al. "Micromagnetic modeling of laser-induced magnetization dynamics using the Landau-Lifshitz-Bloch equation". In: *Applied Physics Letters* 91.23, 232507 (2007).

[7] U. Atxitia et al. "Evidence for thermal mechanisms in laser-induced femtosecond spin dynamics". In: *Phys. Rev. B* 81 (17 2010).

[8] A Ayuela et al. "Structural properties of magnetic Heusler alloys". In: *Journal of Physics: Condensed Matter* 11.8 (1999).

[9] Koopmans B. et al. "Explaining the paradoxical diversity of ultrafast laser-induced demagnetization". In: *Nat. Mater* 9 (3 2010).

[10] Yu.A. Basov, D.V. Roshchupkin, and A.E. Yakshin. "Grazing incidence phase Fresnel zone plate for X-ray focusing". In: *Optics Communications* 109.3–4 (1994). ISSN: 0030-4018.

[11] M. Battiato, K. Carva, and P. M. Oppeneer. "Superdiffusive Spin Transport as a Mechanism of Ultrafast Demagnetization". In: *Phys. Rev. Lett.* 105 (2 2010).

[12] M. Battiato, K. Carva, and P. M. Oppeneer. "Theory of laser-induced ultrafast superdiffusive spin transport in layered heterostructures". In: *Phys. Rev. B* 86 (2 2012).

[13] E. Beaurepaire et al. "Ultrafast Spin Dynamics in Ferromagnetic Nickel". In: *Phys. Rev. Lett.* 76 (22 1996).

[14] F. Beuneu and P. Monod. "The Elliott relation in pure metals". In: *Phys. Rev. B* 18 (6 1978).

[15] M. Blume. "Magnetic scattering of x rays (invited)". In: *Journal of Applied Physics* 57.8 (1985).

[16] William Fuller Brown. "Thermal Fluctuations of a Single-Domain Particle". In: *Phys. Rev.* 130 (5 1963).

[17] Sebastian Brück. "Magnetic Resonant Reflectometry on Exchange Bias Systems". PhD thesis. Stuttgart, Germany: Max-Planck-Insitut für Metallforschung, Stuttgart, 2009.

[18] Paolo Carra et al. "X-ray circular dichroism and local magnetic fields". In: *Phys. Rev. Lett.* 70 (5 1993).

[19] Emanuele Centurioni. "Generalized matrix method for calculation of internal light energy flux in mixed coherent and incoherent multilayers". In: *Appl. Opt.* 44.35 (2005).

[20] C. T. Chen et al. "Experimental Confirmation of the X-Ray Magnetic Circular Dichroism Sum Rules for Iron and Cobalt". In: *Phys. Rev. Lett.* 75 (1 1995).

[21] J. Chovan, E. G. Kavousanaki, and I. E. Perakis. "Ultrafast Light-Induced Magnetization Dynamics of Ferromagnetic Semiconductors". In: *Phys. Rev. Lett.* 96 (5 2006).

[22] O. Chubykalo-Fesenko et al. "Dynamic approach for micromagnetics close to the Curie temperature". In: *Phys. Rev. B* 74 (9 2006).

[23] M. Cinchetti et al. "Spin-Flip Processes and Ultrafast Magnetization Dynamics in Co: Unifying the Microscopic and Macroscopic View of Femtosecond Magnetism". In: *Phys. Rev. Lett.* 97 (17 2006).

[24] Rudolf D. et al. "Ultrafast magnetization enhacement in metallic multilayers driven by superdiffusive spin current". In: *Nat. Comm.* 3 (1037 2012).

[25] F. Dalla Longa et al. "Influence of photon angular momentum on ultrafast demagnetization in nickel". In: *Phys. Rev. B* 75 (22 2007).

[26] N W Dalton. "Approximate calculation of electronic band structures. IV. Density of states for transition metals". In: *Journal of Physics C: Solid State Physics* 3.9 (1970).

[27] W. Demtröder. *Experementalphysik 2*. Berlin, 2004. ISBN: 3-540-20210-2.

[28] Olivier Deparis. "Poynting vector in transfer-matrix formalism for the calculation of light absorption profile in stratified isotropic optical media". In: *Opt. Lett.* 36.20 (2011).

[29] B. Drittler et al. "First-principles calculation of impurity-solution energies in Cu and Ni". In: *Phys. Rev. B* 39 (2 1989).

[30] Spence D. E., Kean P. N., and Sibbet W. In: *Opt. Lett.* 16 (1 1991).

[31] G. L. Eesley. "Observation of Nonequilibrium Electron Heating in Copper". In: *Phys. Rev. Lett.* 51 (23 1983).

[32] *Electrodynamic of continuous media*. Heidelberg: Pergamon Press, 1977. ISBN: 978-0-08-030275-1.

[33] R. J. Elliott. "Theory of the Effect of Spin-Orbit Coupling on Magnetic Resonance in Some Semiconductors". In: *Phys. Rev.* 96 (2 1954).

[34] C. D. Ellis and W. A. Wooster. "The Photographic Action of β-Rays". In: *Proceedings of the Royal Society of London A: Mathematical, Physical and Engineering Sciences* 114.767 (1927). ISSN: 0950-1207.

[35] H. E. Elsayed-Ali et al. "Time-resolved observation of electron-phonon relaxation in copper". In: *Phys. Rev. Lett.* 58 (12 1987).

[36] M. Elzo et al. "X-ray resonant magnetic reflectivity of stratified magnetic structures: Eigenwave formalism and application to a W/Fe/W trilayer". In: *Journal of Magnetism and Magnetic Materials* 324.2 (2012). ISSN: 0304-8853.

[37] A. Eschenlohr et al. "Ultrafast spin transport as key to femtosecond demagnetization". In: *Nat. Mater.* 12 (4 2013).

[38] Moulton P. F. "Spectroscopic and laser characteristics of Ti:Al$_2$O$_3$". In: *J. Opt. Soc.Am. B* 3 (1 1986).

[39] W. S. Fann et al. "Electron thermalization in gold". In: *Phys. Rev. B* 46 (20 1992).

[40] Gerhard H. Fecher et al. "Slater-Pauling rule and Curie temperature of Co2-based Heusler compounds". In: *Journal of Applied Physics* 99.8, 08 (2006).

[41] J. G. Fujimoto et al. "Femtosecond Laser Interaction with Metallic Tungsten and Nonequilibrium Electron and Lattice Temperatures". In: *Phys. Rev. Lett.* 53 (19 1984).

[42] I. Galanakis, P. H. Dederichs, and N. Papanikolaou. "Slater-Pauling behavior and origin of the half-metallicity of the full-Heusler alloys". In: *Phys. Rev. B* 66 (17 2002).

[43] I Galanakis, Ph Mavropoulos, and P H Dederichs. "Electronic struc-
ture and Slater–Pauling behaviour in half-metallic Heusler alloys
calculated from first principles". In: *Journal of Physics D: Applied
Physics* 39.5 (2006).

[44] D. A. Garanin. "Fokker-Planck and Landau-Lifshitz-Bloch equations
for classical ferromagnets". In: *Phys. Rev. B* 55 (5 1997).

[45] D. A. Garanin and O. Chubykalo-Fesenko. "Thermal fluctuations
and longitudinal relaxation of single-domain magnetic particles at
elevated temperatures". In: *Phys. Rev. B* 70 (21 2004).

[46] U. Geiersbach, A. Bergmann, and K. Westerholt. "Structural, mag-
netic and magnetotransport properties of thin films of the Heusler
alloys Cu2MnAl, Co2MnSi, Co2MnGe and Co2MnSn". In: *Journal
of Magnetism and Magnetic Materials* 240.1–3 (2002). 4th Interna-
tional Symposium on Metallic Multilayers. ISSN: 0304-8853.

[47] Michael Ghebrebrhan et al. "Global optimization of silicon photo-
voltaic cell front coatings". In: *Opt. Express* 17.9 (2009).

[48] Ayana Ghosh et al. "Optical constants and band structure of trigonal
NiO". In: *Journal of Vacuum Science & Technology A* 33.6, 061203
(2015).

[49] Maurice Goldman. "Formal Theory of Spin–Lattice Relaxation". In:
Journal of Magnetic Resonance 149.2 (2001). ISSN: 1090-7807.

[50] M. Gotoh et al. "Spin reorientation in the new Heusler alloys Ru2MnSb
and Ru2MnGe". In: *Physica B: Condensed Matter* 213–214 (1995).
ISSN: 0921-4526.

[51] Tanja Graf, Claudia Felser, and Stuart S.P. Parkin. "Simple rules for
the understanding of Heusler compounds". In: *Progress in Solid State
Chemistry* 39.1 (2011). ISSN: 0079-6786.

[52] C. E. Graves et al. "Nanoscale spin reversal by non-local angular mo-
mentum transfer following ultrafast laser excitation in ferrimagnetic
GdFeCo". In: *Nature Mat.* 12 (2013).

[53] J. Güdde et al. "Magnetization dynamics of Ni and Co films on
Cu(001) and of bulk nickel surfaces". In: *Phys. Rev. B* 59 (10 1999).

[54] Michael Haag, Christian Illg, and Manfred Fähnle. "Influence of mag-
netic fields on spin-mixing in transition metals". In: *Phys. Rev. B* 90
(13 2014).

[55] J. P. Hannon et al. "X-Ray Resonance Exchange Scattering". In:
Phys. Rev. Lett. 61 (10 1988).

[56] Fredrik Hansteen et al. "Nonthermal ultrafast optical control of the
magnetization in garnet films". In: *Phys. Rev. B* 73 (1 2006).

[57] M. W. Haverkort et al. "Symmetry analysis of magneto-optical effects: The case of x-ray diffraction and x-ray absorption at the transition metal $L_{2,3}$ edge". In: *Phys. Rev. B* 82 (9 2010).

[58] B.L. Henke, E.M. Gullikson, and J.C. Davis. "X-Ray Interactions: Photoabsorption, Scattering, Transmission, and Reflection at E = 50-30,000 eV, Z = 1-92". In: *Atomic Data and Nuclear Data Tables* 54.2 (1993). ISSN: 0092-640X.

[59] J. P. Hill and D. F. McMorrow. "Resonant Exchange Scattering: Polarization Dependence and Correlation Function". In: *Acta Crystallographica Section A* 52.2 (1996).

[60] J. Hohlfeld et al. "Nonequilibrium Magnetization Dynamics of Nickel". In: *Phys. Rev. Lett.* 78 (25 1997).

[61] J. Hohlfeld et al. "Fast magnetization reversal of GdFeCo induced by femtosecond laser pulses". In: *Phys. Rev. B* 65 (1 2001).

[62] K. Holldack et al. "Femtosecond Terahertz Radiation from Femtoslicing at BESSY". In: *Phys. Rev. Lett.* 96 (5 2006).

[63] Karsten Holldack et al. "FemtoSpeX: a versatile optical pump–soft X-ray probe facility with 100fs X-ray pulses of variable polarization". In: *Journal of Synchrotron Radiation* 21.5 (2014).

[64] W. Hübner and K. H. Bennemann. "Simple theory for spin-lattice relaxation in metallic rare-earth ferromagnets". In: *Phys. Rev. B* 53 (6 1996).

[65] Muhammad N. Huda et al. "Electronic structure of ZnO:GaN compounds: Asymmetric bandgap engineering". In: *Phys. Rev. B* 78 (19 2008).

[66] Anisimov S. I., Kapeliovich B. L., and Perel'man T. L. "Electron emission from metal surfaces exposed to ultrashort laser pulses". In: *Sov. Phys. JETP.* 39 (2 1974).

[67] Schellekens A. J. et al. "Investigating the contribution of supperdiffusive transport to ultrafast demagnetization of ferromagnetic thin films". In: *Appl. Phys. Lett.* 102 (25 2013).

[68] Bigot J.-Y., Vomir M., and Beaurepaire E. "Coherent ultrafast magnetism induced by femtosecond laser pulses". In: *Nat. Phys* 5 (7 2009).

[69] A. Jezierski. "Density of States in Transition Metal–Metalloid Amorphous Alloys". In: *physica status solidi (b)* 153.1 (1989). ISSN: 1521-3951.

[70] Y. Ji et al. "Determination of the Spin Polarization of Half-Metallic CrO_2 by Point Contact Andreev Reflection". In: *Phys. Rev. Lett.* 86 (24 2001).

[71] Torsten Kachel. "The PM3 beamline at BESSY II". In: *Journal of large-scale research fascilities* ().

[72] Torsten Kachel, Frank Eggenstein, and Rolf Follath. "A soft X-ray plane-grating monochromator optimized for elliptical dipole radiation from modern sources". In: *Journal of Synchrotron Radiation* 22.5 (2015).

[73] M. van Kampen et al. "All-Optical Probe of Coherent Spin Waves". In: *Phys. Rev. Lett.* 88 (22 2002).

[74] T. Kasuya. "Exchange mechanisms in Heusler alloys: Virtual double exchange". In: *Solid State Communications* 15.6 (1974). ISSN: 0038-1098.

[75] M. I. Katsnelson et al. "Half-metallic ferromagnets: From band structure to many-body effects". In: *Rev. Mod. Phys.* 80 (2 2008).

[76] N. Kazantseva et al. "Atomistic models of ultrafast reversal". In: *physica status solidi (b)* 244.12 (2007). ISSN: 1521-3951.

[77] N. Kazantseva et al. "Towards multiscale modeling of magnetic materials: Simulations of FePt". In: *Phys. Rev. B* 77 (18 2008).

[78] J. Kübler. "Proceedings of the 4th General Conference of the Condensed Matter Division of the EPS First principle theory of metallic magnetism". In: *Physica B+C* 127.1 (1984). ISSN: 0378-4363.

[79] S. Khan et al. "Femtosecond Undulator Radiation from Sliced Electron Bunches". In: *Phys. Rev. Lett.* 97 (7 2006).

[80] R. J. Kim et al. "Structural Dependence of the Physical Properties for Co_2MnGa Heusler Alloy Films". In: *Journal of the Korean Physical Society* 49.3 ().

[81] T. Kise et al. "Ultrafast Spin Dynamics and Critical Behavior in Half-Metallic Ferromagnet: Sr_2FeMoO_6". In: *Phys. Rev. Lett.* 85 (9 2000).

[82] R. Knorren et al. "Dynamics of excited electrons in copper and ferromagnetic transition metals: Theory and experiment". In: *Phys. Rev. B* 61 (14 2000).

[83] W. Kohn and L. J. Sham. "Self-Consistent Equations Including Exchange and Correlation Effects". In: *Phys. Rev.* 140 (4A 1965).

[84] E. Kojima et al. "Observation of the spin-charge thermal isolation of ferromagnetic $Ga_{0.94}Mn_{0.06}As$ by time-resolved magneto-optical measurements". In: *Phys. Rev. B* 68 (19 2003).

[85] M. Kolbe et al. "Test of band structure calculations for Heusler compounds by spin-resolved photoemission spectroscopy". In: *Phys. Rev. B* 86 (2 2012).

[86] B. Koopmans et al. "Ultrafast Magneto-Optics in Nickel: Magnetism or Optics?" In: *Phys. Rev. Lett.* 85 (4 2000).

[87] B. Koopmans et al. "Unifying Ultrafast Magnetization Dynamics". In: *Phys. Rev. Lett.* 95 (26 2005).

[88] J. Kötzler et al. "Evidence for critical fluctuations in Bloch walls near their disordering temperature". In: *Phys. Rev. Lett.* 71 (1 1993).

[89] Michael Krauß et al. "Ultrafast demagnetization of ferromagnetic transition metals: The role of the Coulomb interaction". In: *Phys. Rev. B* 80 (18 2009).

[90] J. Kübler, A. R. William, and C. B. Sommers. "Formation and coupling of magnetic moments in Heusler alloys". In: *Phys. Rev. B* 28 (4 1983).

[91] Gerrit van der Laan et al. "Experimental proof of magnetic x-ray dichroism". In: *Phys. Rev. B* 34 (9 1986).

[92] Willis E. Lamb. "Theory of an Optical Maser". In: *Phys. Rev.* 134 (6A 1964).

[93] Anni Lehmuskero, Markku Kuittinen, and Pasi Vahimaa. "Refractive index and extinction coefficient dependence of thin Al and Ir films on deposition technique and thickness". In: *Opt. Express* 15.17 (2007).

[94] Steven P. Lewis, Philip B. Allen, and Taizo Sasaki. "Band structure and transport properties of CrO_2". In: *Phys. Rev. B* 55 (16 1997).

[95] R. Ludeke and A. Bauer. "Hot electron scattering processes in metal films and at metal-semiconductor interfaces". In: *Phys. Rev. Lett.* 71 (11 1993).

[96] Martin Magnuson et al. "Electronic structure of GaN and Ga investigated by soft x-ray spectroscopy and first-principles methods". In: *Phys. Rev. B* 81 (8 2010).

[97] G Malmstrom, D J W Geldart, and C Blomberg. "Interaction between local magnetic moments in metals. I". In: *Journal of Physics F: Metal Physics* 6.2 (1976).

[98] Andreas Mann et al. "Insights into Ultrafast Demagnetization in Pseudogap Half-Metals". In: *Phys. Rev. X* 2 (4 2012).

[99] Alexey Melnikov et al. "Ultrafast Transport of Laser-Excited Spin-Polarized Carriers in Au/Fe/MgO(001)". In: *Phys. Rev. Lett.* 107 (7 2011).

[100] H.-Ch. Mertins et al. "Resonant magnetic reflection coefficients at the Fe $2p$ edge obtained with linearly and circularly polarized soft x rays". In: *Phys. Rev. B* 66 (18 2002).

[101]   Yoshio Miura, Kazutaka Nagao, and Masafumi Shirai. "Atomic disorder effects on half-metallicity of the full-Heusler alloys $Co_2(Cr_{1-x}Fe_x)Al$: A first-principles study". In: *Phys. Rev. B* 69 (14 2004).

[102]   S Mizukami et al. "Ultrafast demagnetization for Ni 80 Fe 20 and half-metallic Co 2 MnSi heusler alloy films". In: *Journal of Physics: Conference Series* 200.4 (2010).

[103]   G. M. Mïler et al. "Spin polarization in half-metals probed by femtosecondspin excitation". In: *Nature Mat.* 8 (1 2009).

[104]   B Y Mueller et al. "Driving force of ultrafast magnetization dynamics". In: *New Journal of Physics* 13.12 (2011).

[105]   Reiko Nakajima, J. Stöhr, and Y. U. Idzerda. "Electron-yield saturation effects in L -edge x-ray magnetic circular dichroism spectra of Fe, Co, and Ni". In: *Phys. Rev. B* 59 (9 1999).

[106]   P. Q. J. Nederpel and J. W. D. Martens. "Magneto-optical ellipsometer". In: *Review of Scientific Instruments* 56.5 (1985).

[107]   Madelung. O. *Introduction to Solid-State Theory.* Berlin Heidelberg New York: Springer-Verlag, 1978. ISBN: 3-540-08516-5.

[108]   H. Ohno. "Making Nonmagnetic Semiconductors Ferromagnetic". In: *Science* 281.5379 (1998).

[109]   Koji Ohta and Hatsuo Ishida. "Matrix formalism for calculation of electric field intensity of light in stratified multilayered films". In: *Appl. Opt.* 29.13 (1990).

[110]   N Papanikolaou, R Zeller, and P H Dederichs. "Conceptual improvements of the KKR method". In: *Journal of Physics: Condensed Matter* 14.11 (2002).

[111]   D B Pengra et al. "Resonance-enhanced magnetic X-ray diffraction from a rare-earth alloy". In: *Journal of Physics: Condensed Matter* 6.12 (1994).

[112]   S. Picozzi, A. Continenza, and A. J. Freeman. "Co_2MnX (X = Si, Ge, Sn) Heusler compounds: An *ab initio* study of their structural, electronic, and magnetic properties at zero and elevated pressure". In: *Phys. Rev. B* 66 (9 2002).

[113]   S. Picozzi, A. Continenza, and A. J. Freeman. "Role of structural defects on the half-metallic character of Co_2MnGe and Co_2MnSi Heusler alloys". In: *Phys. Rev. B* 69 (9 2004).

[114]   Z. Q. Qiu and S. D. Bader. "Surface magneto-optic Kerr effect". In: *Review of Scientific Instruments* 71.3 (2000).

[115]   John J. Quinn. "Range of Excited Electrons in Metals". In: *Phys. Rev.* 126 (4 1962).

[116] John J. Quinn and Richard A. Ferrell. "Electron Self-Energy Approach to Correlation in a Degenerate Electron Gas". In: *Phys. Rev.* 112 (3 1958).

[117] M. P. Raphael et al. "Magnetic, structural, and transport properties of thin film and single crystal Co2MnSi". In: *Applied Physics Letters* 79.26 (2001).

[118] H. Regensburger, R. Vollmer, and J. Kirschner. "Time-resolved magnetization -induced second-harmonic generation from the Ni(110) surface". In: *Phys. Rev. B* 61 (21 2000).

[119] B. Rethfeld et al. "Ultrafast dynamics of nonequilibrium electrons in metals under femtosecond laser irradiation". In: *Phys. Rev. B* 65 (21 2002).

[120] Daniel Schick et al. "Analysis of the halo background in femtosecond slicing experiments". In: *Journal of Synchrotron Radiation* 23.3 (2016).

[121] R. W. Schoenlein et al. "Femtosecond studies of nonequilibrium electronic processes in metals". In: *Phys. Rev. Lett.* 58 (16 1987).

[122] R. W. Schoenlein et al. "Femtosecond X-ray Pulses at 0.4 $\mathring{A}$ Generated by 90° Thomson Scattering: A Tool for Probing the Structural Dynamics of Materials". In: *Science* 274.5285 (1996).

[123] R. W. Schoenlein et al. "Generation of Femtosecond Pulses of Synchrotron Radiation". In: *Science* 287.5461 (2000).

[124] A. Scholl et al. "Ultrafast Spin Dynamics of Ferromagnetic Thin Films Observed by fs Spin-Resolved Two-Photon Photoemission". In: *Phys. Rev. Lett.* 79 (25 1997).

[125] G. Schütz et al. "Absorption of circularly polarized x rays in iron". In: *Phys. Rev. Lett.* 58 (7 1987).

[126] C. D. Stanciu et al. "Subpicosecond Magnetization Reversal across Ferrimagnetic Compensation Points". In: *Phys. Rev. Lett.* 99 (21 2007).

[127] *Statical Physics*. Heidelberg: Pergamon Press, 1980. ISBN: 0-7506-3372-7.

[128] D. Steiauf and M. Fähnle. "Elliott-Yafet mechanism and the discussion of femtosecond magnetization dynamics". In: *Phys. Rev. B* 79 (14 2009).

[129] D. Steiauf, C. Illg, and M. Fähnle. "Extension of Yafet's theory of spin relaxation to ferromagnets". In: *Journal of Magnetism and Magnetic Materials* 322.6 (2010). ISSN: 0304-8853.

[130] D Steil et al. "Ultrafast magnetization dynamics in Co-based Heusler compounds with tuned chemical ordering". In: *New Journal of Physics* 16.6 (2014).

[131] Daniel Steil et al. "Band-Structure-Dependent Demagnetization in the Heusler Alloy $Co_2Mn_{1-x}Fe_xSi$". In: *Phys. Rev. Lett.* 105 (21 2010).

[132] C. Suárez, W. E. Bron, and T. Juhasz. "Dynamics and Transport of Electronic Carriers in Thin Gold Films". In: *Phys. Rev. Lett.* 75 (24 1995).

[133] Shigeru Suehara, Tomoya Konishi, and Satoru Inoue. "*Ab initio* calculation of the refractive index and third-order nonlinear optical susceptibility of typical glass formers using the bond additivity model". In: *Phys. Rev. B* 73 (9 2006).

[134] James C. Suits. "New magnetic compounds with Heusler and Heusler-related structures". In: *Phys. Rev. B* 14 (9 1976).

[135] Muhammad Sultan, Alexey Melnikov, and Uwe Bovensiepen. "Ultrafast magnetization dynamics of Gd(0001): Bulk versus surface". In: *physica status solidi (b)* 248.10 (2011). ISSN: 1521-3951.

[136] Muhammad Sultan, Alexey Melnikov, and Uwe Bovensiepen. "Ultrafast magnetization dynamics of Gd(0001): Bulk versus surface". In: *Phys. Stat. Sol. (b)* 248.10 (2011). ISSN: 1521-3951.

[137] C.-K. Sun et al. "Femtosecond-tunable measurement of electron thermalization in gold". In: *Phys. Rev. B* 50 (20 1994).

[138] B. T. Thole et al. "X-ray circular dichroism as a probe of orbital magnetization". In: *Phys. Rev. Lett.* 68 (12 1992).

[139] Emrah Turgut et al. "Controlling the Competition between Optically Induced Ultrafast Spin-Flip Scattering and Spin Transport in Magnetic Multilayers". In: *Phys. Rev. Lett.* 110 (19 2013).

[140] A. Vaterlaus, T. Beutler, and F. Meier. "Spin-lattice relaxation time of ferromagnetic gadolinium determined with time -resolved spin-polarized photoemission". In: *Phys. Rev. Lett.* 67 (23 1991).

[141] J. Wang et al. "Ultrafast Quenching of Ferromagnetism in InMnAs Induced by Intense Laser Irradiation". In: *Phys. Rev. Lett.* 95 (16 2005).

[142] J. Wang et al. "Femtosecond demagnetization and hot-hole relaxation in ferromagnetic $Ga_{1-x}Mn_xAs$". In: *Phys. Rev. B* 77 (23 2008).

[143] Peter J. Webster. "Heusler alloys". In: *Contemporary Physics* 10.6 (1969).

[144] Marko Wietstruk et al. "Hot-Electron-Driven Enhancement of Spin-Lattice Coupling in Gd and Tb $4f$ Ferromagnets Observed by Femtosecond X-Ray Magnetic Circular Dichroism". In: *Phys. Rev. Lett.* 106 (12 2011).

[145] T. Wilhein et al. "Off-axis reflection zone plate for quantitative soft x-ray source characterization". In: *Applied Physics Letters* 71.2 (1997).

[146] A. R. Williams, J. Kübler, and C. D. Gelatt. "Cohesive properties of metallic compounds: Augmented-spherical-wave calculations". In: *Phys. Rev. B* 19 (12 1979).

[147] A.R. Williams et al. "Theory of Invar and Heusler alloys". In: *Journal of Magnetism and Magnetic Materials* 31–34, Part 1 (1983). ISSN: 0304-8853.

[148] Jan-Peter Wüstenberg et al. "Ultrafast magnetization dynamics in the half-metallic Heusler alloy Co2Cr0.6Fe0.4Al". In: *physica status solidi (b)* 248.10 (2011). ISSN: 1521-3951.

[149] Ruqian Wu, Dingsheng Wang, and A.J. Freeman. "First principles investigations of MCD spectra and sum rules for 3d transition metal surfaces". In: *Journal of Magnetism and Magnetic Materials* 132.1 (1994). ISSN: 0304-8853.

[150] J P Xanthakis, R L Jacobs, and E Babic. "A calculation of the densities of states of some amorphous Zr transition-metal alloys". In: *Journal of Physics F: Metal Physics* 16.3 (1986).

[151] Y. Yafet. "g Factors and Spin-Lattice Relaxation of Conduction Electrons*". In: Solid State Physics 14 (1963). Edited by Frederick Seitz and David Turnbull. ISSN: 0081-1947.

[152] J. Zak et al. "Fundamental magneto-optics". In: *Journal of Applied Physics* 68.8 (1990).

[153] J. Zak et al. "Universal approach to magneto-optics". In: *Journal of Magnetism and Magnetic Materials* 89.1–2 (1990). ISSN: 0304-8853.

[154] G. P. Zhang and W. Hübner. "Laser-Induced Ultrafast Demagnetization in Ferromagnetic Metals". In: *Phys. Rev. Lett.* 85 (14 2000).

[155] Qiang Zhang et al. "Ultrafast spin-dynamics in half-metallic CrO_2 thin films". In: *Phys. Rev. B* 74 (6 2006).

[156] Dai Zhao, Hartmut Höchst, and David L. Huber. "Dielectric tensor formulation of magnetic dichroism sum rules". In: *Journal of Applied Physics* 84.5 (1998).

[157] V. P. Zhukov, E. V. Chulkov, and P. M. Echenique. "Lifetimes and inelastic mean free path of low-energy excited electrons in Fe, Ni, Pt, and Au: *Ab initio* GW + T calculations". In: *Phys. Rev. B* 73 (12 2006).